UNIVERSITÀ DEGLI STUDI DI TRIESTE

UNIVERSITÀ DEGLI STUDI DI TRIESTE

XXXVIII CICLO DEL DOTTORATO DI RICERCA IN

Scienze Della Terra, Fluidodinamica E Matematica. Interazioni E Metodiche

Estimation of ocean tidal loading through hourly GNSS processing and analysis of ocean tides in the Adriatic Sea

Settore scientifico-disciplinare: **GEOS-04/A**

DOTTORANDA
Anna Fantoni

COORDINATORE
Prof. Stefano Maset

SUPERVISORE DI TESI
Prof. Carla Braitenberg

CO-SUPERVISORE DI TESI
Dott. Roberto Devoti

ANNO ACCADEMICO 2024/2025

Abstract

Ocean tidal loading (OTL) represents the elastic response of the solid Earth to the varying weight of ocean tides. Although these deformations are typically at the millimeter to centimeter scale, they carry important information on the coupling between ocean dynamics, crustal elasticity, and geodetic observation. Detecting and modeling such small signals remains particularly challenging in regions where tidal amplitudes are weak and ocean models have limited spatial resolution. The Adriatic Sea, with its shallow bathymetry, semi-enclosed geometry, and strong resonance at diurnal and semidiurnal periods, provides a natural laboratory for addressing this problem.

The study investigates how reliably OTL can be detected and quantified from GNSS coordinate time series and how the combination of geodetic and oceanographic observations can improve the characterization of tidal forcing and crustal response. The problem was tackled comprehensively, analyzing tidal constituents in GNSS observations, and testing the ocean tidal models against sea surface observations from tide gauge (TG) and GNSS reflectometry (GNSS-R). The first focuses on methodology, assessing the sensitivity and feasibility to detect OTL constituents of different GNSS processing strategies, namely absolute and differential. The second applies these methods regionally to the northern Adriatic, integrating GNSS with TG and GNSS-R data to analyze both the ocean tides and the associated surface deformation.

Hourly GNSS processing, applied to continuous observations, allows the recovery of tidal displacements at millimetric level. Introducing modern OTL corrections consistently reduces coordinate scatter by up to 22% in the vertical and 10-15% in the horizontal components, confirming that current models capture most of the tidal load. However, residual spectra reveal coherent tidal energy, dominated by the diurnal K_1 and semidiurnal M_2 constituents, pointing to remaining model–data mismatches and orbital aliasing. PPP solutions retrieve a greater number of tidal constituents, whereas DD tends to suppress weaker harmonics due to differencing. The detectability of tidal lines depends critically on record length and noise. Multi-year series enhance spectral resolution and amplitude stability, while higher noise levels can obscure weak tides even in long

datasets.

In the regional application of the Adriatic sea, TG analyses confirm a northward amplification of semidiurnal energy (M_2 and S_2) and a coherent phase progression consistent with resonance. The global model FES2014b reproduces the main pattern, though with localized discrepancies attributable to bathymetric and coastal complexity. GNSS-R observations provide an effective complement to TGs, recovering sea level variations with 2–3 cm agreement and correlations exceeding 90%, demonstrating the potential of low-cost, autonomous coastal monitoring. GNSS-derived OTL displacements reveal a coherent semidiurnal elastic response consistent with model predictions, while diurnal discrepancies primarily reflect GNSS orbital effects rather than true ocean model errors.

The work documents the first hourly GNSS detection of OTL in the Adriatic Sea. By integrating GNSS, GNSS-R, and TG observations, it establishes a cross-validated framework capable of resolving sub-centimeter crustal deformation in a small and resonant basin. The findings advance methodological understanding of GNSS-based tidal analysis and highlight the benefits of combining geodetic and oceanographic techniques for studying ocean-solid Earth interactions. Beyond scientific implications, the integrated monitoring approach offers practical relevance for coastal geodesy, hydrodynamic model calibration, and risk assessment in regions affected by subsidence and sea level rise.

Contents

List of Figures

List of Tables

Chapter 1

Introduction

1.1 State of the art and motivation

Ocean tidal loading (OTL) represents the deformation of the solid Earth caused by the varying weight of ocean tides due to the periodic sea surface height (SSH). Therefore, these deformations are periodic and predominantly vertical, typically reaching amplitudes of a few millimeters to centimeters depending on the location, the tidal regime, and the proximity to coasts or semi-enclosed basins (Farrell, 1972). OTL is an important geophysical phenomenon because it connects ocean dynamics, solid Earth elasticity, and precise geodetic observations. The main challenge lies in accurately observing and modeling these small but complex deformations, especially in regions where the amplitude of ocean tides is small, such as the Adriatic Sea.

Over the last two decades, the use of Global Navigation Satellite System (GNSS) observations has revolutionized our ability to detect and quantify OTL signals (Penna et al., 2015; Bos et al., 2015; Martens et al., 2016). High-precision GNSS positioning, when applied to long and continuous time series, enables the estimation of sub-daily periodic signals corresponding to the main tidal constituents. Studies such as Zajdel et al. (2022) , Perosanz et al. (2023) and Ait-Lakbir et al. (2023) have shown that with multi-GNSS processing, the estimation of solar constituents improves significantly in both accuracy and stability compared to GPS-only solutions. Similar analyses, demonstrated that ambiguity resolution and the inclusion of multiple satellite systems can improve the detection of tidal displacements by up to a few tenths of a millimeter for certain harmonics. These improvements are particularly relevant for small basins where the OTL signal approaches the noise level.

Nevertheless, detecting OTL in small basins from GNSS data remains a demanding task. The amplitude of the deformation is often very small and easily

masked by noise due to multipath effects, local monument instability, antenna calibration errors, or atmospheric delay mismodelling. The quality and continuity of the GNSS record are crucial because short or interrupted time series degrade the spectral resolution, causing leakage between close tidal frequencies. Beyond observational noise, a key limitation arises from the models used to correct OTL in standard GNSS processing. Global OTL corrections, based on large-scale tide models like Finite Element Solution (FES, F. H. Lyard et al., 2021) or TPXO (Egbert et al., 2002), are typically computed on coarse grids that fail to capture the local response in complex coastal and semi-enclosed regions. These models may not correctly represent coastal amplification or resonance effects, leading to biases in the predicted amplitude and phase of tidal loading displacements (Farina et al., 2013; Bos et al., 2015; Petrov et al., 2021). Applying global OTL corrections blindly can therefore introduce systematic residuals that remain visible in GNSS position time series, often as periodic signals at the millimeter level. Differences in model resolution, coastline representation, and interpolation procedures may account for part of these residuals.

The Adriatic Sea provides a particularly interesting and challenging case for ocean tides studies. Its geometry and shallow bathymetry cause natural resonance at diurnal and semi-diurnal periods, amplifying certain tidal constituents such as M_2 and K_1. Medvedev et al. (2020) provided observational evidence of tidal resonance in the basin, identifying eigenmodes around 21.5 h and 10.9 h, which are close to diurnal and semi-diurnal oscillations. Although the overall tidal range in the Adriatic is small compared to ocean coasts, these resonances locally enhance tidal amplitudes and may produce measurable loading effects on the solid Earth. Studies of tidal currents by Poulain (2013) confirmed the dominance of the same tidal constituents, particularly in the northern Adriatic, where coastal amplification is strongest.

Early investigations of OTL effects in the Adriatic Sea date back to the pioneering work of Chiaruttini (1976), who computed the M_2 ocean tide loading response in terms of gravity, tilt, and strain at several sites across the Italian peninsula using Green's function techniques. Several of these sites, including Grotta Gigante and Trieste, are located in northeastern Italy and along the Adriatic coast, highlighting the early recognition of the region's sensitivity to tidal loading effects.

Accurately characterizing the forcing side of the problem is essential to relate GNSS-measured deformation to oceanic mass variation. Traditional tide gauges

(TG) provide high-quality, long-term sea level data, but they are limited spatially and can be influenced by vertical land motion. Recently, GNSS Reflectometry (GNSS-R) has emerged as a promising technique to complement TGs by observing sea level changes through reflected GNSS signals (Larson et al., 2017). In GNSS-R, the signal-to-noise ratio or complex field of reflected signals encodes variations in the reflector height, allowing the retrieval of sea surface variations with centimetric accuracy. Studies such as Tabibi et al. (2020) demonstrated the capability of GNSS-R to recover tidal harmonics in polar regions with good agreement to TGs, while more recent works (e.g. Liu et al., 2022) have shown that dual-frequency GNSS-R can retrieve sea level changes at high temporal resolution, with root-mean-square (rms) differences below 6 cm relative to reference gauges. However, challenges remain, environmental conditions, antenna geometry, and reflection surface characteristics can bias the retrieved amplitudes.

Combining GNSS positioning, TG, and GNSS-R observations offers a powerful framework for studying ocean tides and its surface deformation. GNSS captures the elastic response of the crust to ocean loading, while TGs and GNSS-R provide complementary information on the forcing, allowing cross-validation of models and improving local corrections. For the Adriatic, this integrated approach is particularly promising because it enables investigation of whether the small but non-negligible OTL signal can be resolved above the noise level, and under what processing strategies this becomes possible.

The literature suggests that detectability depends strongly on data quality, processing techniques, and the sophistication of the models employed. High-quality multi-year GNSS records with low noise are required to resolve the small tidal lines in the spectrum. Regional OTL models that include the accurate geometry and resonance characteristics could help to improve the prediction of loading displacements. Furthermore, careful noise modeling and the use of multi-GNSS observations enhance the signal-to-noise ratio, making the detection of millimeter-level tidal deformation feasible.

In summary, the current state of knowledge indicates that while OTL signals are measurable in many parts of the world using GNSS, their detection in small basins such as the Adriatic remains challenging due to their small amplitude and the presence of competing signals from non-tidal processes. Nevertheless, recent advances in GNSS processing, reflectometry, and the integration of auxiliary sea level data provide an unprecedented opportunity to study these subtle signals. A comprehensive analysis combining regional modeling, improved GNSS

techniques, and complementary observations could finally determine whether the Adriatic's resonant tidal loading can be detected and characterized with sufficient confidence. Such work would not only contribute to understanding local geodynamics but also refine the methodology for observing OTL in other small or semi-enclosed basins around the world.

1.2 Outline and summary of the thesis

The thesis is structured into six chapters:

- Chapter 1 contains the introduction and state of the art.
- Chapter 2 covers GNSS fundamentals, including positioning principles, observables, error sources, and advanced processing techniques; tropospheric delays and their modeling; GNSS reflectometry for measuring surface properties; Earth and ocean tides theory and effects; and OTL and its influence on geodetic measurements.
- Chapter 3 describes the datasets, processing strategies and methods used to analyze ocean tidal effects. The details on the deployment of a new multi-GNSS station are described. Global OTL models are presented and the prediction of ocean tidal displacement is described.
- Chapter 4 presents the methodology and results of estimating OTL effects using GNSS data processed with both Precise point positioning (PPP) and Double difference (DD) strategies. The theory and modeling of OTL are then introduced, with emphasis on the use of global models and computation. Subsequently, the chapter compares GNSS-derived displacements with modeled tidal constituents, analyzing RMS improvements and residuals after applying OTL corrections. A detailed tidal analysis is performed for key constituents, highlighting differences between vertical and horizontal components and between DD and PPP solutions. The chapter also addresses challenges such as orbital aliasing, constellation-specific artifacts, and their impact on spectral analysis. Finally, the discussion synthesizes the results, emphasizing the relative strengths and limitations of PPP versus DD, the agreement with global ocean models, and implications for high-precision geodetic applications.

- Chapter 5 provides an overview of tidal dynamics in the northern Adriatic, a region distinguished by shallow waters, semi-enclosed geometry, and strong tidal resonance. It introduces the use of TG measurements to analyze tidal amplitudes and phases, with particular attention to the northward increase of semidiurnal constituents. The chapter also presents GNSS reflectometry (GNSS-R) as a complementary method for sea level monitoring and outlines the processing strategies for elevation angles, azimuth ranges, and reflector heights. Methods for assessing OTL using GNSS-derived 3-D displacements and modeling are described. The separation of tropospheric zenith delay (ZTD) from vertical coordinates estimation is discussed to ensure accurate tidal estimation. Harmonic and spectral analyses of diurnal and semidiurnal tidal constituents are introduced. The chapter highlights the comparison of observed signals with a global tidal model.
- Chapter 6 collects the general conclusions of the study highlighting the findings and the advances in GNSS-based OTL estimation and in ocean tide analysis in the northern Adriatic sea.

Chapter 2

Theory

2.1 Global Navigation Satellite System

The Global Navigation Satellite System (GNSS) is a geodetic technique which provides positioning, navigation, and timing information worldwide. The concept of satellite navigation emerged in the mid-20th century, driven initially by military needs for global positioning (Parkinson et al., 1996). The first operational system became functional in the 1960s. It was succeeded by the Global Positioning System (GPS), developed by the United States Department of Defense and opened for civilian use in the 1980s (Kaplan et al., 2006). Nowadays, GNSS encompasses multiple independent and interoperable systems: GPS (United States), GLONASS (Russia), Galileo (European Union), BeiDou (China), and regional augmentation systems such as QZSS (Japan) and NavIC (India). Together, these systems form a dense network of satellites that significantly improve coverage, accuracy, and redundancy. The information for each constellation about the number of orbiting and working satellites and frequencies used are summarized in Table 2.1 (Montenbruck et al., 2014).

Table 2.1: Summary of the main GNSS constellations, indicating the number of operational satellites and nominal carrier frequencies for each system. The values correspond to the nominal full constellation status, with frequency designations following standard international conventions.

Constellation	**N° of satellites**	**Frequencies**
GPS	31	L1, L2, L5
GLONASS	24	L1, L2, L3
GALILEO	27	E1, Ea5, Eb5, E6
BEIDOU	44	B1, B2, B3

GNSS positioning techniques are founded on the principle of trilateration (Ka-

plan et al., 2006). Each satellite continuously transmits a coded signal containing its orbital parameters (ephemeris) and precise transmission time. A receiver, by comparing the received signal time to its internal clock, can estimate the signal's travel time and thus the distance to the satellite. With simultaneous pseudorange measurements from at least four satellites, the receiver solves for its three-dimensional position and clock offset. GNSS satellite's motion obeys Newton's law of universal gravitation, orbiting on elliptical orbits, following Kepler's laws of planetary motion. The latter link orbital velocity and period to the orbital altitude and the Earth's Mass (Parkinson et al., 1996). The predictable nature of these orbits enables precise modelling of satellite positions (ephemerides), which is critical for accurate positioning. The trilateration principle can be expressed mathematically as follows: if the position of the i-th satellite is $\mathbf{S}_i = (X_i, Y_i, Z_i)$ and the unknown receiver position is $\mathbf{R} = (X, Y, Z)$, the geometric range is given by

$$\rho_i = \sqrt{(X - X_i)^2 + (Y - Y_i)^2 + (Z - Z_i)^2}. \tag{2.1}$$

The measured pseudorange P_i includes the receiver clock offset δt_r relative to GNSS system time:

$$P_i = \rho_i + c\,\delta t_r + \varepsilon_i, \tag{2.2}$$

where c is the speed of light and ε_i accounts for measurement noise and other residual errors. At least four independent measurements are required to solve for the three receiver coordinates and the clock offset. This nonlinear system is typically linearized and solved iteratively using least-squares estimation.

All GPS satellite signals originate from a fundamental oscillator frequency f_0 (10.23 MHz). The two right-hand circularly polarized carrier frequencies, f_1 and f_2 (1.57 GHz and 1.22 GHz), use biphase modulation to transmit clock data, orbital parameters, and navigation messages (Figure 2.1). GPS satellites transmit three coded signals modulated onto two carrier frequencies (L_1 and L_2): the precision code *P(t)*, the coarse acquisition (C/A) code *C(t)*, and the navigation message *D(t)*. The first two codes are modulated on the carrier frequencies as so-called pseudo random noise (PRN) sequences. The L_1 signal contains both P-code and C/A-code, the L_2 signal contains just the P-code. The third signal is the broadcast or navigation message which contains information about the satellite orbit, clock, health status, and other data.

GNSS positioning accuracy is limited by a range of error sources (Hofmann-Wellenhof et al., 2008):

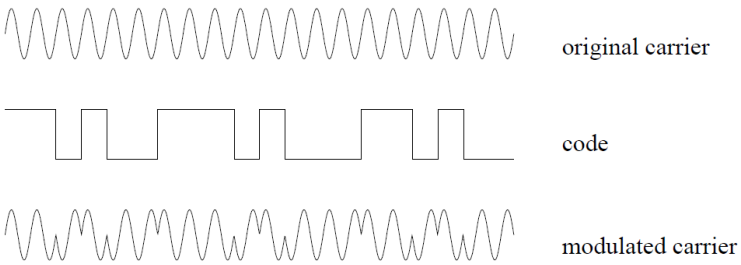

Figure 2.1: Schematic representation of the GPS signal structure. Each satellite transmits right-hand circularly polarized carrier waves (L1, L2) modulated by pseudo-random noise (PRN) codes and a navigation message containing ephemerides, clock corrections, and system status information. Adapted from the Bernese GNSS Software Manual (Dach et al., 2015).

- Satellite clock errors: deviations of onboard atomic clocks from system time;
- Ephemeris errors: inaccuracies in the broadcast satellite positions;
- Ionospheric delay: dispersive delay caused by the ionosphere, varying with solar activity and signal frequency;
- Tropospheric delay: non-dispersive delay due to atmospheric temperature, pressure, and humidity variations;
- Multipath: interference from reflected signals arriving in addition to the direct path;
- Receiver noise: thermal and quantization noise in the electronics.

Several mitigation strategies are used to address these effects. Dual-frequency measurements allow elimination of first-order ionospheric delay using the ionosphere free linear combination. Tropospheric delays can be modelled with mapping functions such as Saastamoinen function or Vienna Mapping Function (VMF) (Saastamoinen, 2013; Boehm et al., 2006). Multipath effects are reduced through antenna design, choke rings, and careful site placement. Satellite clock and orbit errors are minimized using precise products from the International GNSS Service (IGS) (Kouba et al., 2001). For high-accuracy applications, methods such as Differential GNSS (DGNSS), Real-Time Kinematic (RTK), or Precise Point Positioning (PPP) can achieve millimeter-level precision (Zumberge et al., 1997).

2.1.1 GNSS observable modeling and position estimation

GNSS positioning techniques are broadly categorized into absolute (standalone) and relative (differential) methods. Absolute GNSS positioning determines a receiver's coordinates directly from satellite signals using broadcast ephemeris data, providing positions in a global reference frame (Misra et al., 2002; Hofmann-Wellenhof et al., 2008). In contrast, relative GNSS positioning, which involves two or more receivers, computes the position of one receiver relative to another with known coordinates. This approach effectively mitigates common errors such as satellite clock biases, orbital errors, and atmospheric delays (Leick et al., 2015; Kaplan et al., 2017).

Within this classification, Precise Point Positioning (PPP) represents an advanced form of absolute positioning, while double-difference (DD) techniques constitute a key relative positioning method based on differential processing between multiple receivers.

2.1.1.1 Double-Difference processing

In DD processing, coordinate estimation is performed by solving for a baseline relative to a fixed reference station with precisely known coordinates using the carrier phase observables. The observation equations are constructed by forming differences between receivers observing the same satellite and furthermore forming a second difference between satellites observing the same receiver. This method offers the advantage of largely eliminating clock errors associated with both the satellite and the receiver (G. Blewitt, 2015).

The DD method is a widely adopted and highly effective approach for processing GNSS data. The advantages of this approach is its ability to eliminate the receiver clock bias directly, rather than treating it as an estimated parameter and its effectiveness in mitigating common errors such as tropospheric and ionospheric delays as well as tidal and non-tidal loading effects.

The pseudorange observation equations for the receivers A and B observing the same satellite j are (G. Blewitt, 2015):

$$\begin{aligned} L_A^j &= \rho_A^j + c(\tau_A - \tau^j) + Z_A^j - I_A^j + B_A^j \\ L_B^j &= \rho_B^j + c(\tau_B - \tau^j) + Z_B^j - I_B^j + B_B^j \end{aligned} \tag{2.3}$$

where ρ_i^j is the geometry distance between the receiver and the satellite, τ^j and τ_i are the satellite and receiver clock bias, c is the velocity of light, Z_i^j is the tropospheric delay, I_i^j is the ionospheric delay and B_i^j represents measurement noise and multipath effects.

The single difference eliminates the satellite clock bias by taking the difference between two receivers A and B observing the same satellite j.

$$\begin{aligned} \Delta L_{AB}^j = L_A^j - L_B^j = \\ = \Delta\rho_{AB}^j + c\Delta\tau_{AB} + \Delta Z_{AB}^j - \Delta I_{AB}^j + B_{AB}^j \end{aligned} \tag{2.4}$$

The double difference further removes the receiver clock bias by taking the difference between two single differences from two satellites j and k.

$$\begin{aligned} \Delta\Delta L_{AB}^{jk} = \Delta L_{AB}^j - \Delta L_{AB}^k = \\ = (\Delta\rho_{AB}^j - \Delta\rho_{AB}^k) + (\Delta Z_{AB}^j - \Delta Z_{AB}^k) \\ - (\Delta I_{AB}^j - \Delta I_{AB}^k) + (\Delta B_{AB}^j - \Delta B_{AB}^k) \end{aligned} \tag{2.5}$$

The same occurs for the carrier phase observation equation, leading to the removal of both satellite and receiver clock biases, leaving only atmospheric effects, measurement noise, and integer ambiguities.

$$\begin{aligned} \Delta\Delta\Phi_{AB}^{jk} = \Delta\Phi_{AB}^j - \Delta\Phi_{AB}^k = \\ = (\Delta\rho_{AB}^j - \Delta\rho_{AB}^k) + (\Delta Z_{AB}^j - \Delta Z_{AB}^k) \\ - (\Delta I_{AB}^j - \Delta I_{AB}^k) + \lambda(\Delta N_{AB}^j - \Delta N_{AB}^k) \end{aligned} \tag{2.6}$$

where λ is the wavelength for carrier-phase respective frequency and N is the ambiguity parameter for the phase observation.

2.1.1.2 Precise Point Positioning processing

PPP is a processing technique that estimates receiver coordinates using undifferenced code and carrier-phase observations from a single station. By relying on precise satellite orbit and clock products derived from a global network, PPP can achieve centimeter-level positioning accuracy without the need for local reference stations (Zumberge et al., 1997; Rizos et al., 2012). During each epoch, receiver coordinates are estimated together with nuisance parameters such as receiver clock errors, atmospheric delays, and carrier-phase ambiguities, which also

absorb unmodeled satellite and receiver hardware delays and initial phase windup effects.

PPP requires the application of accurate and consistent models for several error sources, including antenna phase-center offsets and variations, solid Earth tides, Earth rotation, relativistic effects, and atmospheric delays. The first-order ionospheric delay is commonly mitigated through ionosphere-free linear combinations of dual-frequency observations or explicitly estimated, while the tropospheric delay is generally treated as an unknown parameter and estimated during processing. Accurate modeling of atmospheric delays has been shown to significantly reduce PPP convergence time (Ma et al., 2025), which otherwise remains one of the main limitations of the technique.

PPP convergence can be further improved by increasing the number of available satellite constellations, as multi-GNSS observations enhance satellite geometry and redundancy (Banville et al., 2020). Moreover, unmodeled satellite and receiver biases prevent carrier-phase ambiguities from being directly resolved as integers, motivating the development of advanced PPP ambiguity resolution techniques (PPP-AR) (Gabor, 1999). Compared to DD processing, PPP offers notable computational efficiency, as its processing time scales linearly with the number of stations, whereas DD processing scales more rapidly due to the increasing number of baselines (Elgered et al., 1998).

The observation equations, respectively for pseudoranges (L_{P_i}) and carrier phase (L_{Φ_i}), can be written as follows (Ogaja, 2022):

$$\begin{aligned} L_{P_i} &= \rho_i^j + c(\tau_i - \tau^j) + Z_i^j - I_i^j + \Delta + \epsilon_{P_i} \\ L_{\Phi_i} &= \rho_i^j + c(\tau_i - \tau^j) + \lambda(N + B + b) + Z_i^j - I_i^j + \Delta + \epsilon_{\Phi_i} \end{aligned} \tag{2.7}$$

where ρ_i^j is the geometry distance between the receiver i and the satellite j, τ^j and τ_i are the satellite and receiver clock bias, c is the velocity of light, Z_i^j is the tropospheric delay, I_i^j is the ionospheric delay, λ is the wavelength for carrier-phase respective frequency, B and b are the uncalibrated phase delays for receiver and satellite, respectively, N is the ambiguity parameter for the phase observation, Δ is the correction component containing satellite and receiver phase centers and ϵ_{Φ_i} and ϵ_{P_i} are the measurement noise for pseudo-range and carrier-phase.

The ionospheric-free combination of double-frequency f_1 and f_2 GNSS pseudorange P_{IF} and carrier phase Φ_{IF} observation equations corrected for satellite clock bias and antenna phase center variations can be written as (Kouba et al.,

2001):

$$P_{IF} = \frac{f_1^2 P_1 - f_2^2 P_2}{f_1^2 - f_2^2}$$
$$\Phi_{IF} = \frac{f_1^2 \Phi_1 - f_2^2 \Phi_2}{f_1^2 - f_2^2} \tag{2.8}$$

2.1.2 GNSS tropospheric and ionospheric delay

The zenith tropospheric delay (ZTD) is an essential parameter that represents the delay experienced by GNSS signals as they travel through the Earth's troposphere. This delay arises due to the refraction caused by atmospheric pressure, temperature, and water vapor, which influence the propagation speed of electromagnetic waves. For a station at the sea level and standard atmospheric conditions, the delay due to tropospheric refraction is of the order of 2.3 m (Dach et al., 2015).

The ZTD can be decomposed into two principal components (Bevis et al., 1994: the Zenith Hydrostatic Delay (ZHD), predominantly caused by dry atmospheric gases, it is relatively stable and can be accurately modeled using surface pressure measurements and empirical models, and the Zenith Wet Delay (ZWD), attributable to atmospheric water vapor, which is highly variable both spatially and temporally, posing challenges for precise estimation.

The physical basis of tropospheric delay can be described through the concept of atmospheric refractivity. The refractive index of the neutral atmosphere n differs slightly from unity, and the refractivity N is expressed as (Thayer, 1974):

$$N = (n-1) \times 10^6 = k_1 \frac{P}{T} + k_2 \frac{e}{T^2}, \tag{2.9}$$

where P is the total atmospheric pressure, e is the water vapor partial pressure, T is the absolute temperature (local air temperature at the point where refractivity is evaluated), and k_1, k_2 are empirically derived constants. The first term, which depends on total pressure, gives rise to the hydrostatic component of the delay (Saastamoinen, 1972), while the second term, which depends on water vapor content, defines the wet component. The total ZTD can be expressed as the sum of its components:

$$\text{ZTD} = \text{ZHD} + \text{ZWD} \tag{2.10}$$

Since GNSS observations are not generally made at zenith, the ZTD must be mapped into slant tropospheric delays (STDs) along each satellite–receiver line

of sight. This transformation is performed using mapping functions $m(e)$, such as the Vienna Mapping Function (VMF, Landskron et al., 2018):

$$\mathrm{STD} = m_{\mathrm{hyd}}(e) \cdot \mathrm{ZHD} + m_{\mathrm{wet}}(e) \cdot \mathrm{ZWD} \tag{2.11}$$

where e is the satellite elevation angle and $m_{\mathrm{hyd}}(e)$, $m_{\mathrm{wet}}(e)$ are the hydrostatic and wet mapping functions, respectively. The accuracy of these mapping functions is crucial, as deficiencies propagate into GNSS positioning results and atmospheric parameter retrieval.

The variability of the ZWD component is particularly noteworthy. In tropical regions, the ZWD can contribute more than 40% of the total ZTD, whereas in high-latitude or arid regions, it remains a relatively small fraction. Temporal fluctuations occur on multiple scales: from minutes to hours in response to convective systems and diurnal heating, to seasonal cycles linked to monsoon circulation, storm tracks, and large-scale climatic regimes. This variability makes ZWD estimation both a challenge and an opportunity. On one hand, it complicates the modeling of GNSS signal delays; on the other hand, it provides a valuable proxy for atmospheric water vapor, an essential variable for weather forecasting and climate monitoring (Guerova et al., 2016; Riccardi et al., 2021).

As a result, ZTD estimates derived from GNSS networks have become an important data source for atmospheric sciences. They are now routinely assimilated into Numerical Weather Prediction models to improve short-term forecasts, especially in regions with sparse radiosonde or satellite coverage. Moreover, long-term ZTD and ZWD records have proven useful for detecting trends in atmospheric water vapor, offering insights into climate variability and potential links to global warming. In addition, high-resolution GNSS-derived tropospheric delays contribute to early warning systems for severe weather events, such as thunderstorms and typhoons, where rapid changes in water vapor play a critical role in storm development.

Beyond their atmospheric relevance, ZTD estimates are also sensitive to geophysical loading effects. Earth deformation phenomena such as OTL, atmospheric pressure loading (APL), and solid Earth tides cause station displacements that affect the effective signal path length. Neglecting these displacements introduces systematic biases into ZTD estimation. Studies have demonstrated strong correlations between deformation effects and differences in ZTD estimates when such corrections are applied. For example, a correlation of 0.99 has been observed

between vertical OTL-induced deformation and ZTD discrepancies, underscoring the interplay between the Earth's deformation and atmospheric delay modeling (Dach et al., 2000). These findings highlight that accurate ZTD estimation requires a holistic treatment of both atmospheric conditions and geophysical loading processes.

The ionospheric delay is another major source of error affecting GNSS signal propagation. It originates from the dispersive nature of the ionosphere, a partially ionized region of the upper atmosphere extending from approximately 60 km to more than 1000 km above the Earth's surface. The magnitude of the ionospheric delay depends primarily on the total electron content (TEC) along the signal path and is inversely proportional to the square of the signal frequency (Klobuchar, 1987; Schaer et al., 1999).

For single-frequency GNSS observations, the ionospheric delay can reach several tens of meters during periods of high solar activity, making it the dominant error source if not adequately modeled. However, in dual-frequency GNSS processing, the first-order ionospheric delay can be effectively removed by forming the ionosphere-free (IF) linear combination of carrier-phase and code observations (Hofmann-Wellenhof et al., 2008). This combination exploits the dispersive nature of the ionosphere and reduces the first-order ionospheric effect by more than 99% .

Despite the use of the ionosphere-free combination, higher-order ionospheric effects remain, including second- and third-order terms, which are related to the geomagnetic field and electron density gradients. Although these residual effects are typically at the millimeter level for positioning applications, they can become relevant for high-precision geodetic analyses and during periods of enhanced ionospheric activity.

In the Precise Point Positioning (PPP) approach adopted in this study, the ionosphere-free linear combination is used in conjunction with precise satellite orbit and clock products. Consequently, no explicit estimation of ionospheric parameters is performed. Instead, the residual ionospheric effects are absorbed into the observation noise and parameter estimation, while external ionospheric products implicitly contribute to the generation of precise satellite clocks used in PPP processing (Hernández-Pajares et al., 2007).

2.1.3 GNSS reflectometry (GNSS-R)

GNSS was originally developed for navigation purposes, but its applications have expanded significantly over recent decades. With the advancement of GNSS as a satellite-based microwave (L-band) technology, its applications have expanded significantly, revealing new capabilities and potential uses. More recently, the GNSS reflectometry (GNSS-R) technique has been investigated, in relation with the exploitation of the radio wave reflection (Zavorotny et al., 2014). GNSS-R has been demonstrated to be a reliable method to analyze different geophysical properties of the surface, for example sea level variation, soil moisture, and snow depth (Larson et al., 2017).

In GNSS-R, several techniques have been developed depending on the type of GNSS observable exploited. The most commonly used approach in ground-based applications is based on the signal-to-noise ratio (SNR), which captures the interference pattern between direct and reflected signals (Larson et al., 2017). However, GNSS-R is not limited to SNR-based methods. Alternative approaches have been proposed using pseudorange (code) observations (Katzberg et al., 2013), carrier-phase measurements, and signal strength indicators (SSI). Code-based GNSS-R techniques are mainly employed in airborne and spaceborne configurations, where reflected signals are analyzed in terms of delay and Doppler characteristics, while phase-based approaches exploit carrier-phase residuals to infer reflector geometry with high precision, albeit with increased sensitivity to phase ambiguities and noise.

An additional observable of interest for GNSS reflectometry is the SSI, which represents a raw measure of received signal power recorded in GNSS observation files (Nievinski et al., 2014). Unlike SNR observables, which may not always be available, particularly in early GNSS datasets or for specific receiver types, SSI data are systematically present in GNSS observation files. As such, SSI-based reflectometry offers a valuable alternative for exploiting legacy GNSS data and long-term time series when SNR measurements are missing or unreliable. This broad range of GNSS-R techniques extends the applicability of reflectometry beyond modern receivers and enables the use of both historical and multi-constellation datasets.

Sea surface height (SSH) variations have been studied through the last decades with two main techniques: observations with TG and satellite radar altimetry. TG measures relative sea level with respect to a local reference on the land, with-

out taking into account ground motion. On the other hand, satellite radar altimetry measures SSH at high spatial resolution along its track, but the temporal data accessibility is in the order of hours to days, therefore the data have lower temporal resolution than the tide gauges. GNSS-R is able to overcome these problems, offering an estimation with a deviation in the order of few millimeters respect to TG. The local reference point coincides with the GNSS antenna mount, which can be directly monitored within a global reference frame. As a result, GNSS-derived sea level is inherently an absolute measurement, making it sensitive to long-term absolute sea level trends (Devoti et al., 2023). In conclusion, the GNSS reflected signal can measure the SSH with high spatial and temporal resolution (Jin et al., 2010).

Permanent GNSS receivers are instruments that receive signals from satellites and use them to position the receiver in space and time. They are affected by multipath errors, which occur when the direct signal from the satellite interferes with signals reflected by surfaces in the vicinity of the receiver. To mitigate these effects in conventional GNSS positioning, specialized antenna designs and installation strategies are routinely adopted, such as choke-ring antennas, ground planes, radomes, and other multipath-suppressing devices developed by GNSS manufacturers (Bilich et al., 2008). These instrumental solutions aim to attenuate or reject reflected signals in order to improve positioning accuracy. In contrast, the GNSS-Reflectometry (GNSS-R) technique intentionally exploits reflected signals to estimate the height of the reflective surface and to study its temporal variations (Larson et al., 2013).

In this study case, we use the technique to estimate the SSH of the sea surface below the GNSS station, in order to obtain information on the dynamic of the ocean tides.

Signals reflected off the water will be delayed in reaching the receiver, and as a result will not necessarily be in phase with the direct signal. As the satellite passes overhead, the angle of reflection changes, and thus the delay will change. At a certain moment, the reflected signal will be in phase with the main signal, enhancing it, at other times it will be out of phase, dampening its strength. These variations in the signal strength are measured by the receiver's SNR. Considering a GNSS antenna located at a height h above the sea surface, it detects two signals: direct signal, which travels straight from the satellite receiver, and reflected signal, which bounces off the surface before reaching the receiver. As illustrated in Figure 2.2, the path of the reflected signal is longer than the direct one, and

their difference is indicated by Δs as:.

$$\Delta s = 2hsin(e) \tag{2.12}$$

where e is the elevation angle. The additional path length introduces a phase difference $\Delta\Phi$ between the direct and reflected signals, and can be written as:

$$\Delta\Phi = \frac{2\pi\Delta s}{\lambda} = \frac{4\pi h}{\lambda} sin(e) \tag{2.13}$$

where λ is the wavelength of the GNSS signal (Altuntas et al., 2021).

The superposition of both signals, direct and reflected, results in interference,

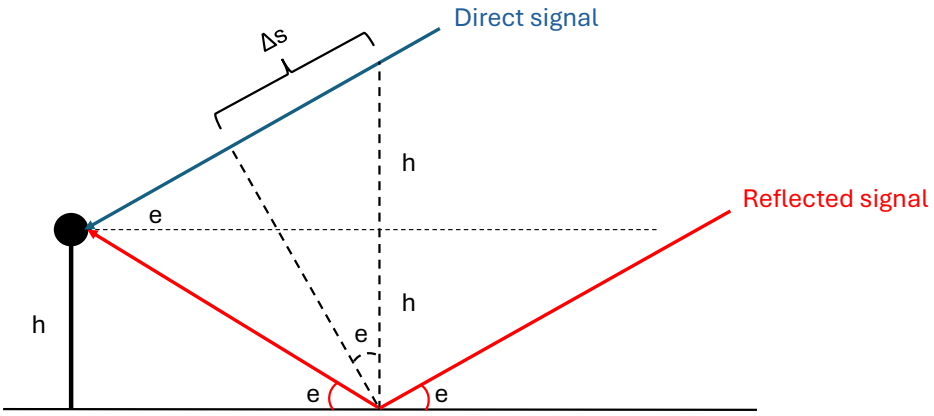

Figure 2.2: Geometrical configuration of the GNSS-R principle. The direct and reflected signals received by a GNSS antenna are shown, with Δs representing the excess path length of the reflected signal relative to the direct one. The interference between the two signals encodes information on the antenna height above the reflecting surface.

which produces oscillations in the observed signal power. Eliminating the direct signal from the SNR function, the remaining data are the contribution of the reflected signal (Figure 2.3). The direct signal is eliminated by removing the smooth, slowly varying trend (e.g., using a polynomial or low-pass filter) from the SNR data, leaving only the oscillations caused by the reflected signal.

The detrended SNR can be expressed:

$$SNR = A\, cos\left(\frac{4\pi h}{\lambda} sin(e) + \phi\right) \tag{2.14}$$

where A and ϕ are the amplitude and phase of the SNR (Altuntas et al., 2023). Using $sin(e)$ as the independent variable, the oscillation frequency of SNR signal

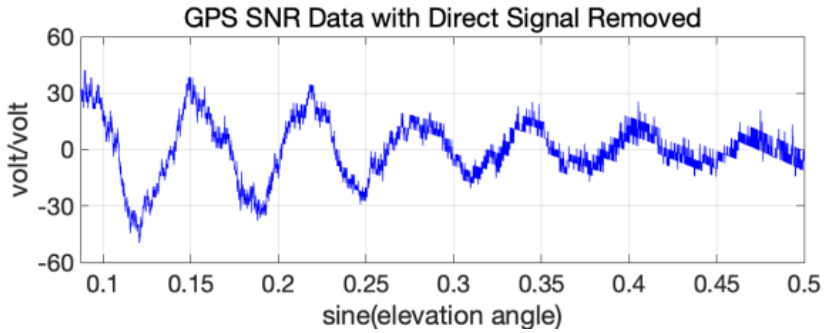

Figure 2.3: Example of a detrended signal-to-noise ratio (SNR) record after removing the direct signal component. The residual oscillations correspond to interference fringes resulting from the interaction between the direct and reflected GNSS signals, which can be analyzed to estimate the height of the reflecting surface (source: `https://gnssrefl.readthedocs.io/_/downloads/en/latest/pdf/`).

becomes a constant function of h, therefore a Lomb-Scargle periodogram can be implemented to extract the vertical distance between the antenna and the reflective surface (Lomb, 1976; Scargle, 1982).

$$f = \frac{4\pi h}{\lambda} \Rightarrow h = \frac{4\pi f}{\lambda} \tag{2.15}$$

The main guidelines for a multi purpose GNSS station, including GNSS-R, can be summarized as follow (Geremia-Nievinski et al., 2019):

- unobstructed view from the antenna to the satellite in the sky and from the antenna down to the surface. The station equipment (receiver, battery, etc.) should be placed outside the reflection surface view;
- for water level monitoring, surface visibility has to be maximized. For roof-top installations, the preference of the antenna location should be to sidewalls or corners;
- The ideally azimuthal sector should be around 180°, at the very least 90° wide;
- The choice of the sampling interval should be inversely proportional to the height of the antenna above the surface;
- record more than just GPS system;
- RINEX3 format is strongly recommended, as it stores the SNR separately for each GNSS signal.

2.2 Earth and ocean tides

Tides are periodic deformations of both the solid and fluid (ocean and atmosphere) Earth, produced primarily by the differential gravitational forces exerted by the Moon and the Sun (Melchior, 1983; Pugh et al., 2014). Even though the Sun is vastly more massive than the Moon, its tidal influence is weaker because tidal forces decrease with the cube of the distance, making the Moon's proximity the dominant factor (Doodson et al., 1997). The fundamental mechanism can be described in terms of the tidal potential V_t, which represents the second-order term in the spherical harmonics expansion of the gravitational potential of an external body of mass M at distance R from the Earth's center. For a point at distance r from the Earth's center, with ψ being the angle between the point and the direction to the external body, the tidal potential is given by:

$$V_t(r, \psi) \approx \frac{GMr^2}{2R^3} P_2(\cos\psi) \tag{2.16}$$

where G is the gravitational constant and P_2 is the Legendre polynomial of degree 2, written as:

$$P_2(\cos\psi) = \frac{1}{2}\left(3\cos^2\psi - 1\right) \tag{2.17}$$

This potential induces periodic forces that generate characteristic diurnal and semi-diurnal oscillations in both the solid Earth and the oceans. The solid Earth's response, often termed Earth tides or body tides (EBT), involves vertical displacements of up to $\sim$ 0.4 m and is described in terms of the dimensionless Love numbers h, l, and k, which respectively parameterize radial displacement, horizontal displacement, and the change in gravitational potential (Wahr, 1981; Lambeck, 1988). The vertical displacement u_r at the Earth's surface due to the tidal potential can be expressed as:

$$u_r = h\frac{V_t}{g} \tag{2.18}$$

where g is the mean gravitational acceleration at the surface. Similarly, the perturbation $\delta\Phi$ in the gravitational potential due to Earth deformation is

$$\delta\Phi = kV_t \tag{2.19}$$

Inelastic behavior in the mantle, characterized by the quality factor Q, introduces a phase lag δ between the tidal potential and the response, leading to irreversible energy dissipation (Wahr, 1981).

Ocean tides, in contrast, represent the hydrodynamic adjustment of the ocean's free surface to the same tidal potential. Their large scale behavior is governed by the depth-integrated, linearized shallow water equations on a rotating sphere (Pugh et al., 2014):

$$\begin{aligned} \frac{\partial \mathbf{u}}{\partial t} + f\,\hat{\mathbf{k}} \times \mathbf{u} &= -g\nabla\eta + \mathbf{F}_t - r\mathbf{u} \\ \frac{\partial \eta}{\partial t} + \nabla \cdot (H\mathbf{u}) &= 0 \end{aligned} \tag{2.20}$$

where $\mathbf{u}$ is the horizontal velocity, f is the Coriolis parameter, η is the sea surface height, H is the mean depth, $\mathbf{F}_t$ is the body force per unit mass associated with the tidal potential, and r is a linear friction coefficient. The observed tidal signal at a location can be represented as the superposition of N harmonic constituents (Doodson et al., 1997):

$$\eta(t) = \sum_{n=1}^{N} A_n \cos(\omega_n t + \phi_n) \tag{2.21}$$

where A_n is the amplitude, ω_n is the angular frequency, and ϕ_n is the phase lag of the n-th constituent (e.g., M_2, S_2, K_1, O_1). Resonance within ocean basins can amplify specific constituents when the natural oscillation period T_0 of the basin approaches the forcing period T_f, with the amplification factor approximated by

$$\mathcal{A} \propto \frac{1}{\sqrt{(1-(T_f/T_0)^2)^2 + (2\zeta T_f/T_0)^2}} \tag{2.22}$$

where ζ is a damping coefficient.

The redistribution of ocean mass during the tidal cycle produces additional deformation of the lithosphere, known as ocean tide loading (OTL), with vertical displacements of several centimeters in some coastal regions. Conversely, Earth tides modulate the local gravitational potential and relative sea level, subtly influencing the propagation of tidal waves.

The harmonic description of the tidal gravity potential and its derived quantities, as tidal displacements and earth tidal gravity perturbation is made with analogous harmonic expansion to equation 2.21.

The study of tides has broad scientific importance. In geodesy, precise tidal

models are required for correcting GPS and very long baseline interferometry (VLBI) measurements, as well as for interpreting data from satellite gravimetry missions such as GRACE and GRACE-FO. Tides thus represent a fundamental coupling between celestial mechanics, geophysics, and ocean dynamics, and ongoing advances in theoretical modeling, high resolution bathymetric mapping, and satellite observation will continue to refine our understanding and prediction of their variability, energetics, and role in the long-term evolution of the Earth–Moon system.

2.3 Ocean loading effect

OTL represents a critical process within Earth's dynamic system, where the gravitational forces exerted by the gravitational bodies induce periodic oceanic motions that subsequently load and deform the Earth's surface. This periodic redistribution of water mass affects coastal and continental regions, generating complex spatial and temporal deformations. Unlike solid Earth tides, which are governed solely by gravitational forces, OTL is highly influenced by factors such as bathymetry, coastal boundaries, and basin geometry, which interrupt and modulate the tidal flow (Pugh et al., 2014). The theoretical foundation for understanding this process was established by Farrell, 1972, who developed a model to describe the elastic response of the Earth's crust to tidal loading. These deformations have important implications for precise geodetic measurements, seismic activity, and the study of Earth's rheology, therefore accurately modeling OTL is essential for applications across geophysics, oceanography, and environmental monitoring.

The theoretical formulation of OTL begins with the surface load exerted by the ocean tide, which can be expressed as a pressure function $L(\theta, \lambda, t)$ defined on the Earth's surface, where θ and λ denote latitude and longitude, respectively, and t represents time. The load is proportional to the ocean tide height $H_t(\theta, \lambda, t)$, scaled by the seawater density ρ_w and gravitational acceleration g.

$$L(\theta, \lambda, t) = \rho_w g \, H_t(\theta, \lambda, t). \tag{2.23}$$

The Earth's elastic response to this load can be modeled through the convolution of $L(\theta, \lambda, t)$ with a Green's function $G(\psi)$, which represents the displacement at a site due to a unit point load applied at angular distance ψ. Taking into

consideration the vertical displacement u_r, the motion equation is

$$u_r(\theta_0, \lambda_0, t) = \iint_{\Omega} L(\theta, \lambda, t)\, G_r(\psi)\, d\Omega, \tag{2.24}$$

where (θ_0, λ_0) are the coordinates of the observing site, ψ is the great-circle distance between (θ, λ) and (θ_0, λ_0), and $d\Omega$ is the surface area element.

The Green's functions are derived from the load *Love numbers* (h'_n, l'_n, k'_n) computed for a given Earth model, which quantify the Earth's elastic response to surface mass loading at spherical harmonic degree n (Macdonald, 1975). Specifically, the radial Green's function is given by the spherical harmonic expansion (Farrell, 1972; Farrell, 1972):

$$G_r(\psi) = \frac{1}{4\pi\bar{\rho}gR} \sum_{n=0}^{\infty} \frac{2n+1}{1+k'_n}\, h'_n\, P_n(\cos\psi), \tag{2.25}$$

where R is the Earth's radius, $\bar{\rho}$ is the mean Earth density, and P_n denotes the Legendre polynomial of degree n. Analogous expressions exist for the horizontal Green's functions $G_\theta(\psi)$ and $G_\lambda(\psi)$, which depend on the horizontal load Love number l'_n.

Continuous GNSS data have been used to study the OTL displacement of the Earth since the beginning of the 2000s (Allinson, 2004, R. Dach, 2001). These data allow for high precision monitoring of Earth's surface displacement, providing invaluable insights into the effects of OTL on the Earth's crust. GNSS measurements, particularly in coastal and near-shore regions, are instrumental in detecting both vertical and horizontal deformations caused by the redistribution of ocean mass during tidal cycles.

Cotidal charts derived from global tide models such as FES2014b (F. H. Lyard et al., 2021) provide a combined representation of the amplitude and phase of tidal constituents. Figure 2.4 illustrates the global distribution of the M_2 tide, where contour lines indicate cotidal phases referenced to Greenwich and color shading denotes amplitudes. The amplitude reflects the strength of the ocean tide at a given location, while the phase describes the relative timing of high water with respect to a reference meridian. Together, these parameters govern the spatiotemporal pattern of ocean mass redistribution and hence directly control the magnitude and timing of the associated Earth deformation.

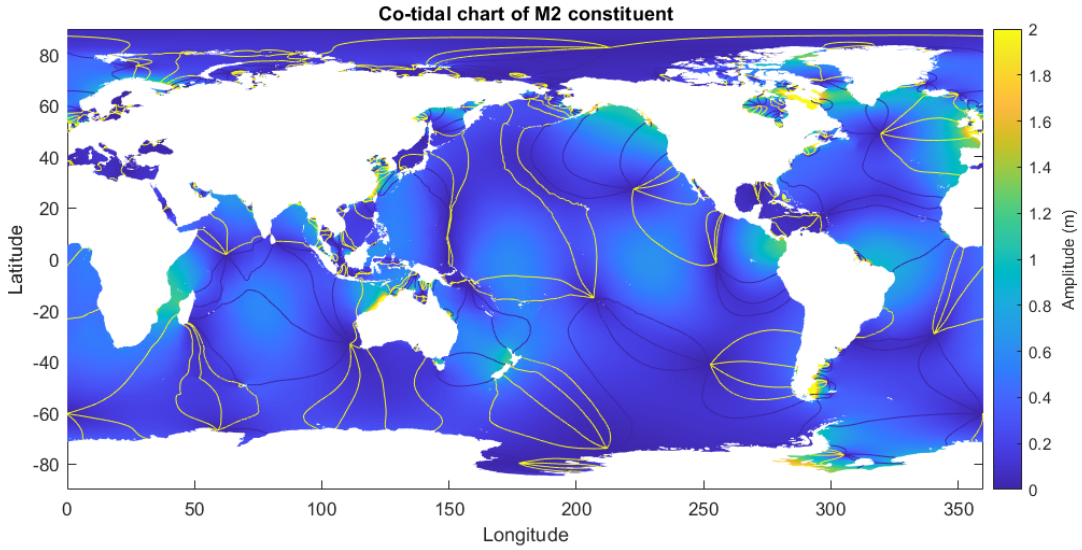

Figure 2.4: Global cotidal chart of the principal lunar semidiurnal constituent M_2 from the FES2014b ocean tide model. Color shading represents tidal amplitude, while yellow and blue lines indicate cotidal phase referred to Greenwich. The chart illustrates the spatial variability of the tidal response that governs ocean tide loading effects on the solid Earth.

Chapter 3

Data and methods

This section introduces the datasets used and the processing methods applied in this study. We first describe the databases of GNSS positioning, TG, and GNSS-R. We then outline the data processing workflows for the two GNSS observation types, with a particular emphasis on GNSS positioning techniques, as these are the primary means to extract direct OTL effects. Finally, we present the global and local tidal models employed in the analysis, along with details on model predictions and deformation computations.

3.1 GNSS network

For the GNSS positioning analysis, the database was organized into two distinct parts: one network dedicated to evaluating the processing strategies (Double Difference and Precise Point Positioning), and another focused on the Northern Adriatic Sea investigation.

3.1.1 Processing strategies database

The first part of the study focuses on two GNSS stations, CASC (Portugal) and VEN1 (Italy), positioned along the coasts of the Atlantic and Adriatic seas, respectively, and subject to distinct oceanic loading conditions (Figure 3.1). Both DD and PPP processing strategies have been applied to evaluate the hourly time series of these stations. In the DD processing scheme, two additional reference stations, VILL (Spain) and BRMF (France), are included and held fixed at known positions, while the baselines between station pairs are estimated on an hourly basis. At these locations, the expected OTL effects as from global models (e.g. Egbert et al., 2002; R. D. Ray, 2013; F. H. Lyard et al., 2021; Hart-Davis et al.,

2021) are predominantly influenced by the Atlantic Ocean, with OTL component amplitudes reaching approximately 35 mm and by the Adriatic Sea where the OTL amplitudes are significantly smaller, ranging from 5 mm to 8 mm. The baseline length between CASC and VILL is approximately 510 km whereas the distance between VEN1 and BRMF is about 570 km. The DD method involves determining the position of a GNSS station relative to a precisely surveyed position, referred to as the fiducial station (Dey et al., 2014). By fixing the reference station, the position of the secondary station is estimated, enabling the determination of relative motion with high precision while mitigating common-mode effects.

Using the PPP approach, two fiducial station networks (see Appendix Table A.1 and Table A.2) were selected, one associated with CASC and the other with VEN1. Although PPP is formally an absolute positioning technique, regional common-mode systematic errors have been documented in GNSS coordinate time series, manifesting coherently across networks and affecting multiple frequency bands, particularly at annual and sub-annual periods (J. Ray et al., 2008; Pintori et al., 2022). To mitigate these spatially correlated biases, a hybrid processing strategy was adopted. First, PPP solutions were computed for a regional network of stations. Subsequently, the resulting network solution was jointly estimated and rigidly transformed into the ITRF2020 reference frame using a set of high-stability fiducial reference stations. This strategy reduces common-mode errors and improves the stability of the reference frame by mitigating spatially correlated effects, including tropospheric delays, orbit mismodelling, and residual clock biases. The distribution of the stations is shown in Figure 3.1.

The raw GNSS RINEX files were obtained from the European Reference Frame (EUREF) database Bruyninx et al., 2019, the Réseau de Géodésie Permanente (RGP `https://rgp.ign.fr/`) and International GNSS Service (IGS) database (Teunissen et al., 2017).
s from the GPS, GALILEO and GLONASS constellations were consistently integrated into all processing strategies.

All datasets were acquired at a standard 30-second sampling interval, and observation from the GPS, GALILEO and GLONASS constellations were consistently integrated into all processing strategies. The temporal interval of investigation covers a period of 220 days.

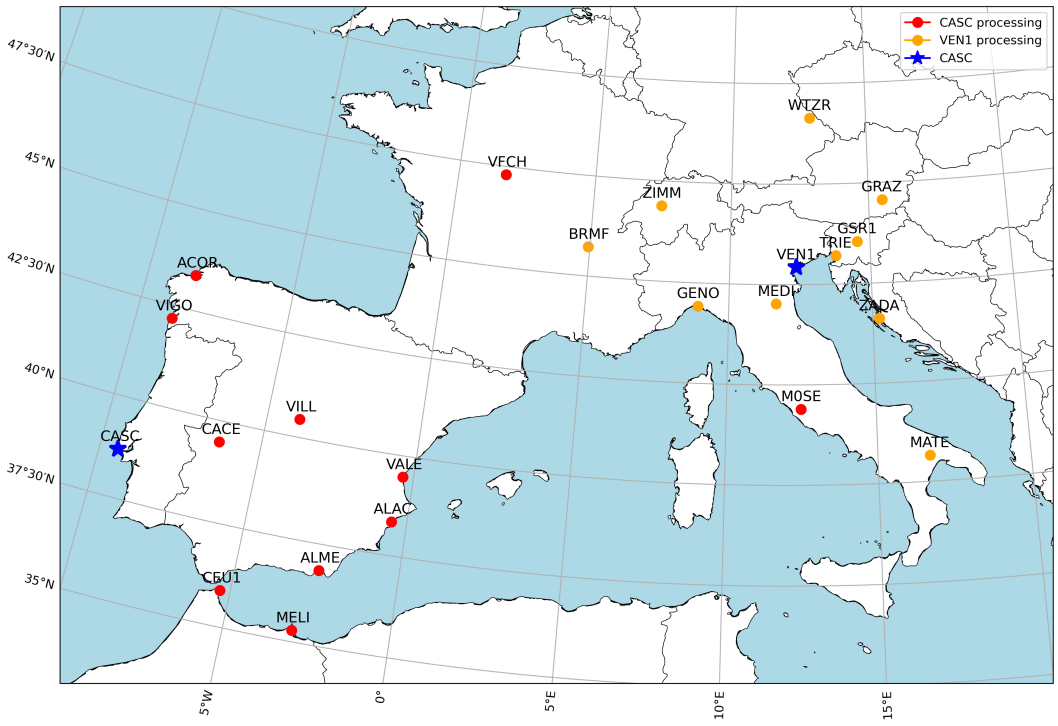

Figure 3.1: Distribution of the selected GNSS stations is shown, with red dots representing the network of IGS fiducial stations chosen for estimating the CASC position using the PPP processing strategy, and orange dots representing the network of fiducial stations selected for estimating the VEN1 position using the same strategy. CASC and VEN1 positions are indicated with blue stars.

3.1.2 Adriatic GNSS network

The second part of the study is interested in the determination and evaluation of the OTL effect in the Northern Adriatic region. As mentioned in the previous section, in the area the ocean tides reach amplitudes in range of 20 to 27 cm of height, with a consequent loading effect between 5 to 10 mm.

The analysis is conducted over seven GNSS stations located along the Italian and Croatia coastline (Table A.3), considering a fiducial network for a total of sixteen stations. In Figure 3.2, the distribution of the stations is shown, in red the sites where the OTL displacement is estimated, in green the fiducial stations for the reference frame. The regional fiducial network, as done before, was jointly estimated and consequently rigidly transformed into the ITRF2020 reference frame, to eliminate common errors and mitigate the noise in the time

series. The investigated stations are located at a distance from the coastline of around 300 meters, except for TRIE and MEDI, which are respectively 2.5 kilometers and 50 kilometers far.

The stations were processed with the PPP strategy in order to obtain the absolute effect of the ocean loading at the specific site. The RINEX files are collected from the EUREF database for stations GARI, MEDI, PORE, VEN1, and ZADA, TRIE data are acquired from the Rete GNSS Friuli Venezia Giulia (`https://rem.regione.fvg.it/`), and lastly ANCG data were provided by the Istituto Nazionale di Geofisica e Vulcanologia (INGV) database, acquired from the ITALPOS network. All datasets were acquired at a standard 30-second sampling interval, and observations from the GPS, GALILEO and GLONASS constellations were consistently integrated into all processing strategies. The time coverage of the study is 1 year, from 1^{st} of July 2021 to 1^{st} of July 2022.

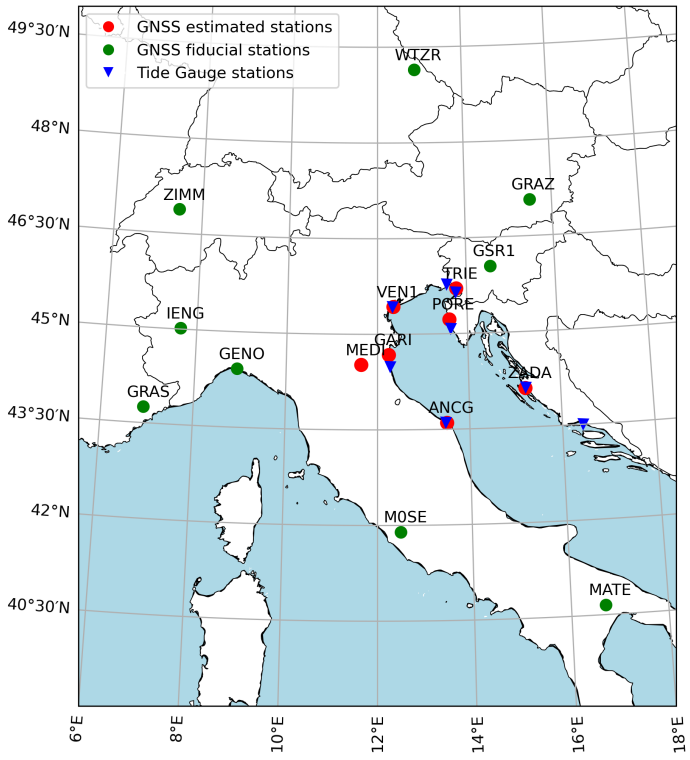

Figure 3.2: Distribution of the selected GNSS and tide gauge stations. The red dots represent the GNSS investigated stations, the green dots represent the network of fiducial stations, and the blue triangles represent the tide gauge stations.

3.2 Tide gauge network

For the TG analysis, eight stations were selected (blue triangles in Figure 3.2): Trieste, Venezia, Ravenna, Ancona, Monfalcone, Rovinj, Split, and Zadar. Observations from Trieste, Venezia, Ravenna, and Ancona are managed by the Istituto Superiore per la Protezione e la Ricerca Ambientale (ISPRA), which provides data with a 10-minute sampling interval through its online database (`www.mareografico.it`). Data from the Monfalcone station were retrieved from the Protezione Civile della Regione Friuli Venezia Giulia website (`https://monitor.protezionecivile.fvg.it/`), with a sampling interval of 15 minutes. The Croatian stations (Rovinj, Split, and Zadar) were obtained from the Center for Open Science (OSF, `https://osf.io/s9hjv`), with an hourly sampling rate. The locations and temporal coverage of all stations are detailed in Table A.4 and shown in Figure 3.2.

3.3 GNSS-R network

The selection of the GNSS-R stations is based on the criteria listed in section 2.1.3, which define the characteristics of suitable reflection sites. Along the Northern Adriatic coast, the stations identified as suitable for the analysis are PORE, VEN1, and GARI. Table 3.1 presents the station identification name, coordinates and satellites available for the selected stations. The RINEX data are collected from the EUREF Permanent Network database for one year period covering the year 2023.

Additionally, a new GNSS station was installed under the supervision of our

Table 3.1: Coordinates and available satellite constellations for the GNSS-R stations selected along the northern Adriatic coast (G = GPS, R = GLONASS, E = Galileo, C = BeiDou).

Station ID	**Latitude (°)**	**Longitude (°)**	**Satellite**
GARI	44.6769	12.2494	GREC
PORE	45.226	13.595	GRE
VEN1	45.430	12.354	GREC
SIST	45.768	13.630	G

research group by the Department of Mathematics, Informatics and Geoscience

(MiGe) at the University of Trieste. The station is called SIST. The selected site is at the terrace of the Diporto Nautico of Sistiana (DNS), which generously granted access for the installation. This station was established to monitor sea level variations in a location previously lacking both tide gauge and GNSS infrastructure. The geographic coordinates of the site are 45° 46' 4.32" N and 13° 37' 51.25" E, as shown in Figure 3.3 and the details are in Table 3.1.

Figure 3.3: Geographic location of the newly installed GNSS station at the Diporto Nautico of Sistiana (DNS), north of Trieste.

Sistiana is a town north of the city of Trieste, which has been affected by many sea storms in the past. The most recent one occurred at the beginning of November 2023, causing significant damage to the port infrastructure and nearby roads. Monitoring the area was also a factor in the choice of this location.

The station is equipped with a Trimble NetRS receiver connected to a simple ANT3B-CAL antenna (Figure 3.4 A). The Trimble NetRS is a dual-frequency GPS receiver widely used in geodetic, geophysical, and environmental monitoring applications, designed for continuous, high-precision data collection. The Simple ANT3B-CAL (Figure 3.4 B) is a compact, high-precision GNSS antenna designed for scientific and geodetic applications; it is calibrated to perform across multiple GNSS constellations (GPS, GLONASS, Galileo and BeiDou) and frequencies, offering a reliable signal reception for both static and kinematic setups. To enable remote access for data retrieval, a 4G LTE router was connected to the receiver, and a Raspberry Pi was configured to transmit the data to a remote archive

accessible from any location. The equipment is installed on the external terrace of the building, oriented toward the sea to facilitate the reception of signals reflected from the marine surface. The antenna is attached to a pole, while the instrumentation is placed inside a waterproof box.

The receiver acquisition is set in order to collect hourly and daily data files,

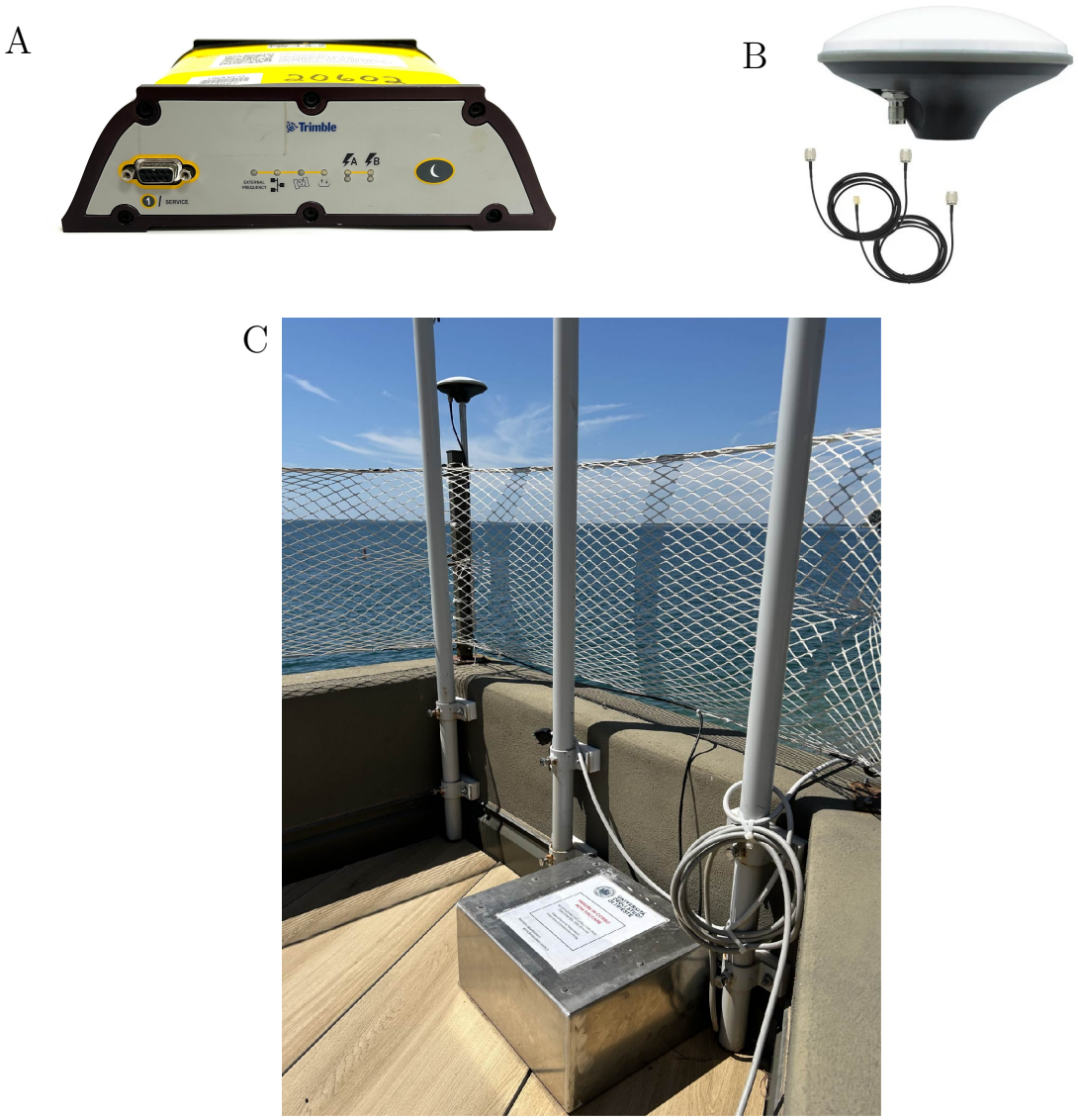

Figure 3.4: Equipment setup of the DNS GNSS-R station at Sistiana. Trimble NetRS dual-frequency receiver (A), Simple ANT3B-CAL antenna (B), and final installation on the terrace facing the sea (C).

with a sampling frequency of 5 minutes. The installation was performed on the 24^{th} of July 2025 and the data analyzed in this study cover a period of 24 days.

3.4 GNSS positioning data processing

The data were processed using the Bernese 5.4 GNSS software (Dach et al., 2015), which is a high quality standard scientific package for geodetic applications based on GNSS. It is provided and updated by the Astronomical Institute of the University of Bern (AIUB). The software supports multi-GNSS constellations, including GPS, GLONASS, Galileo, and BeiDou, and provides full control over observation modeling, parameter estimation, and error mitigation. It implements both relative (DD) and absolute (PPP) positioning strategies, offering flexibility depending on the application's requirements. The processing strategies were tailored to support the investigation of OTL effects and to assess the performance of different GNSS positioning techniques.

The Bernese processing strategy can be divided into three main phases: data preparation, data pre-processing, and data processing (Figure 3.5). The data preparation phase is the same for both techniques, consisting in the creation of the new campaign and its preparation. The term *campaign* is used for a set of data which should be processed together. This directory involves important files essential for the process and it is organized in different subdirectories, listed in Table 3.2.

Table 3.2: Directory structure of a Bernese 5.4 campaign, showing the main folders and their contents (adapted from Dach et al., 2015).

Directory	**Content**
ATM	files related to atmosphere (troposphere and ionosphere)
BPE	BPE–related output files
GRD	grid files for various purposes
OBS	Bernese–formatted observation files
ORB	orbit– and ERP–related files
ORX	original RINEX files
OUT	program output and numerous miscellaneous files
RAW	RINEX files to be imported for processing
SOL	solution–related files (NEQ and SINEX)
STA	station–related files

Subsequently, the observation data are downloaded, along with the orbit data and Earth Orientation Parameters (EOP). The RINEX data must be converted into the Bernese format using the functions *RNXGRA*, *RNXSMT*, and *RXOBV3*,

which respectively generate a pseudo-graphic representation of the RINEX observation files, clean and smooth the code observations, perform numerous checks on the header information, and finally convert the RINEX code and phase data into the Bernese format. The preparation of pole, orbit, and clock information is carried out using the functions *POLUPD*, *ORBGEN*, and *RNXCLK*, which respectively reformat and update pole files, generate or update standard orbits, and extract satellite clock information from the clock RINEX file.

The data pre-processing phase prepares the data for the main estimation program. Firstly, program *RNXSMT* is applied to detect cycle slips and outliers on RINEX level, and *CODSPP* compute the corrections for synchronizing the receiver clocks with respect to GPS time. Following this first common steps, then the processing strategy is different based on the technique used. For DD solution the program *SNGDIF* forms baselines from zero-difference observation files and again cycle slips and outliers are detected and resolved using *MAUPRP* program.

The parameter estimation is based on least squares adjustment, using the two main programs *GPSEST* and *ADDNEQ2*. The first processes the observations starting from the observation files, set up the observation equations and solves the normal equation (NEQ); the second manipulates and combines solutions at the NEQ level. In the estimation program, the residuals are then checked with the program *RESRMS*, and the misbehaving stations and satellites are detected in *RESHCK* program. *ADDNEQ2* program is subsequently followed by *GPSXTR* program, which extracts summaries from *GPSEST*/*ADDNEQ2* program output. For the PPP processing, the Helmert transformation between two coordinates files is applied in *HELMR1* program. The last steps of the PPP processing is the computation of the velocities (*NUVELO*), propagation of coordinates with the velocity field (*COOVEL*), and merge of the coordinates (*CRDMERGE*).

The data were processed hourly in order to better distinguish the sub-diurnal ocean tidal component, considering GPS, GLONASS and GALILEO satellites. Using data from all these GNSS is crucial in hourly data analysis as it significantly increases observation redundancy, improving the precision and reducing the noise in the coordinate time series (figure 3.6).

MGEX products from the Center for Orbit Determination in Europe (CODE) were chosen. In modeling the troposphere, the Dry VMF3 model (Landskron et al., 2018) serves as the a priori model. For the mapping function, the Wet VMF3 function is applied to refine the estimation of tropospheric parameters (Landskron et al., 2018). The zenith delay, which accounts for variations in

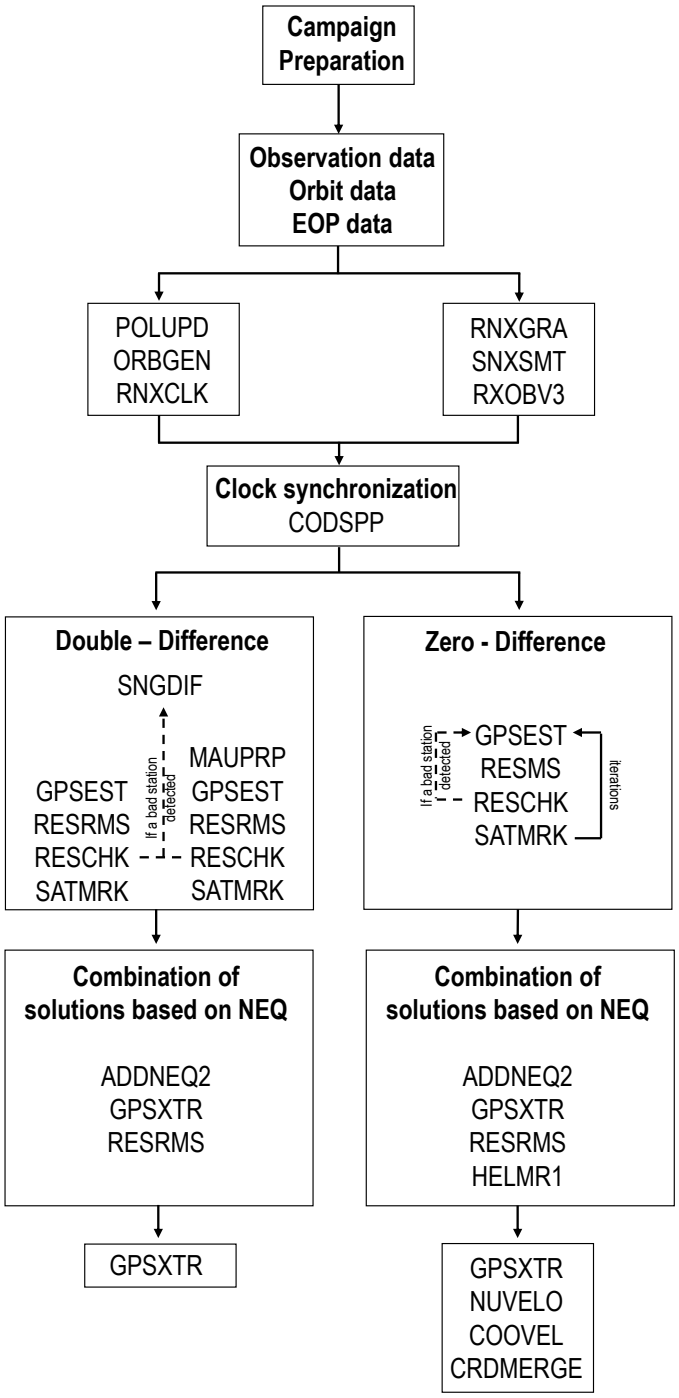

Figure 3.5: Workflow of the Bernese 5.4 processing chain for Double-difference and zero difference solutions, illustrating the main phases: data preparation, pre-processing, and parameter estimation.

atmospheric water vapor, is estimated every hour. For the PPP solutions, the gradient was also estimated every 6 hours, modelled with Chen-Herring model (Chen et al., 1997); while for DD solutions it is not recommended for single

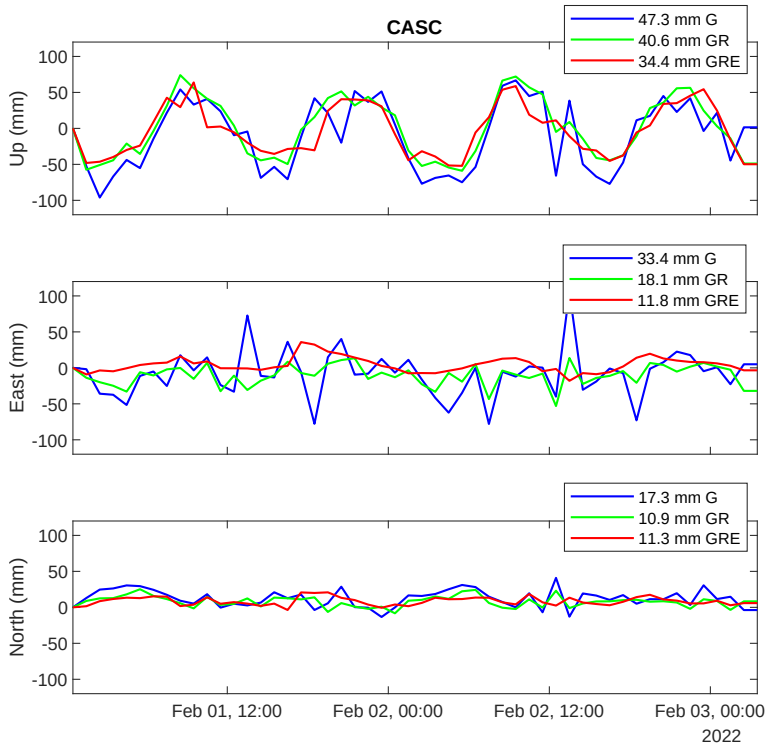

Figure 3.6: Noise comparisons of CASC PPP components processed from only GPS (G), GPS+GLONASS (GR) and GPS+GLONASS+GALILEO (GRE), showing the decrease of the noise by adding constellations.

baseline (Dach et al., 2015). The ionosphere is addressed using the ionosphere-free linear combination (L3) method, which helps to mitigate ionospheric delays in the GNSS signals. For the solid Earth tide corrections, the strategy adheres to the IERS 2010 Conventions (Petit et al., 2010). No additional atmospheric model corrections are incorporated beyond the troposphere modeling. Corrections for the pole tide are implemented in accordance with the IERS 2010 Conventions. However, the permanent tide effect is not removed from the model. Non-tidal loading effects, such as oceanic, atmospheric and hydrologic, are not accounted for in the processing strategy. The Earth Orientation Parameters (EOP) for diurnal and semidiurnal variations are corrected following the IERS 2010 Conventions. Regarding satellite parameters, the satellite center of mass corrections are applied using phase center offsets from the IGS20.pcm model, and the satellite antenna phase variations are modeled using the PCV model phase center from IGS20.atx. Finally, an elevation angle cutoff of 3 degrees is utilized to reduce the impact of low-elevation signals, which are generally more susceptible to atmospheric and multipath errors (EUREF guidelines `https://www.epncb.oma.be/_documentation/guidelines/guidelines_analysis_centres.pdf`). Table 3.3 summarizes

the Bernese 5.4 processing strategy.

This processing strategy was applied to both DD and PPP techniques in two instances: initially, without the inclusion of any OTL model to study the behavior of ocean tides in GNSS observations, and subsequently, with the application of the FES2014b (F. H. Lyard et al., 2021) global OTL model to evaluate the influence of this effect on the solutions and to analyze the potential differences between the model predictions and the observations.

Table 3.3: Summary of the Bernese 5.4 GNSS processing strategy adopted in this study, detailing the modeling assumptions, corrections, and parameter estimation setup for both DD and PPP solutions.

Parameter	**Description**
Troposphere	A priori model: Dry VMF3 Mapping Function for parameters: Wet VMF3 Estimation: Zenith delay every 1 hour
Ionosphere	Ionosphere–Free Linear Combination L3
Solid Earth tide	IERS 2010 Conventions
Ocean tidal model	See text
Atmospheric model	Not applied
Pole tide	IERS 2010 Conventions
Permanent tide	Not removed from model
Non-tidal loading	Not applied for any
EOP model	IERS 2010 Conventions for diurnal, semidiurnal
Satellite center of mass	Phase centers offsets from IGS20.pcm applied
Satellite antenna phase	PCV model phase center from IGS20.atx applied
Elevation angle cutoff	3

3.5 GNSS-R data processing

The GNSS stations selected for the estimation of the sea level variation by the GNSS reflectometry technique were processed with the *Gnssrefl* open source software provided by Kristine M. Larson (Larson, 2024). It is a python-based software able to extract the SNR data from the RINEX files and to determine different types of estimates, such as water level variations, snow accumulation, ice surface changes, and surface soil moisture.

The processing procedure follows a straight workflow, as illustrated in Figure 3.7. The SNR data are collected from the RINEX file through the *rinex2snr*

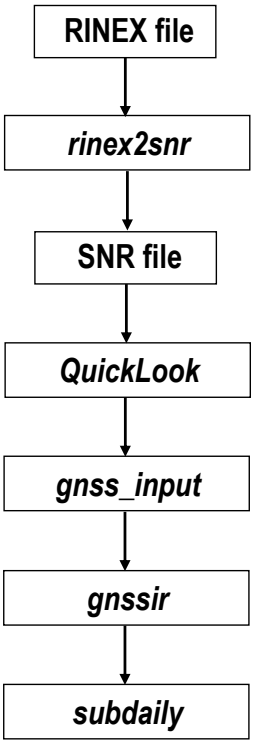

Figure 3.7: Workflow of the *Gnssrefl* processing.

function, supporting both RINEX 2 and 3 versions. To check if the receiver is collecting this information, the RINEX header file is inspected. As shown in Figure 3.8, the red rectangles highlight the observation types: the signal to noise information is identified by the ones starting with letter *S*.

The geometric concept underlying GNSS-R measurements is the reflection zone, which is the surface region where GNSS signals can reflect toward the antenna. For coherent reflections, this zone is typically modeled as a first Fresnel zone, an elliptical region centered around the specular reflection point. The size and shape of this zone depend on the GNSS signal wavelength, satellite elevation angle, and receiver height (Tabibi et al., 2020). The increase of the elevation angle leads to a smaller sensing zone which is closer to the antenna. Above a certain angle the Fresnel zone starts to include the shore and the SNR data are no more representing the sea surface height. Figure 3.9 shows an example of the reflection zone for station VEN1, obtained by using the web app developed along with the software (`https://gnss-reflections.org/`). Each one of the colored clusters represents the reflection zone for a single rising or setting GPS satellite

```
3.0                 COMPACT RINEX FORMAT                    CRINEX VERS   / TYPE
RNX2CRX ver.4.1.0                       19-Jul-24 07:14     CRINEX PROG / DATE
     3.05           OBSERVATION DATA    M (MIXED)           RINEX VERSION / TYPE
GR30 V4.20          ASI-egeos           20221118 235942 UTC PGM / RUN BY / DATE
gfzrnx-2.00-8219    FILE PROCESSING     20240719 071400 UTC COMMENT
INITIAL_RINEX_VERSION: 3.03                                 COMMENT
VEN100ITA                                                   MARKER NAME
19513M001                                                   MARKER NUMBER
Automatic           ASI-egeos                               OBSERVER / AGENCY
1705432             LEICA GR30          4.20/7.300          REC # / TYPE / VERS
19244003            LEIAR20         NONE                    ANT # / TYPE
        0.0000        0.0000        0.0000                  ANTENNA: DELTA H/E/N
  4379846.8268   959292.0000  4521100.1253                  APPROX POSITION XYZ
C    8 C2I C7I D2I D7I L2I L7I S2I S7I                      SYS / # / OBS TYPES
E   16 C1C C5Q C7Q C8Q D1C D5Q D7Q D8Q L1C L5Q L7Q L8Q S1C  SYS / # / OBS TYPES
       S5Q S7Q S8Q                                          SYS / # / OBS TYPES
G   16 C1C C2S C2W C5Q D1C D2S D2W D5Q L1C L2S L2W L5Q S1C  SYS / # / OBS TYPES
       S2S S2W S5Q                                          SYS / # / OBS TYPES
R   12 C1C C2C C2P D1C D2C D2P L1C L2C L2P S1C S2C S2P      SYS / # / OBS TYPES
S    4 C1C D1C L1C S1C                                      SYS / # / OBS TYPES
START OF RINEX header check by ROB      20221120 102049 UTC COMMENT
 with respect to                                            COMMENT
 https://gnss-metadata.eu/v1/sitelog/exportlog?id=VEN100ITA COMMENT
RINEX file downloaded from BEV                              COMMENT
END OF RINEX header check by ROB                            COMMENT
SNR is mapped to RINEX snr flag value [1-9]                 COMMENT
LX:      < 12dBHz -> 1; 12-17dBHz -> 2; 18-23dBHz -> 3      COMMENT
       24-29dBHz -> 4; 30-35dBHz -> 5; 36-41dBHz -> 6       COMMENT
       42-47dBHz -> 7; 48-53dBHz -> 8; >= 54dBHz -> 9       COMMENT
DBHZ                                                        SIGNAL STRENGTH UNIT
     0                                                      RCV CLOCK OFFS APPL
 24 R01  1 R02 -4 R03  5 R04  6 R05  1 R06 -4 R07  5 R08  6 GLONASS SLOT / FRQ #
    R09 -2 R10 -7 R11  0 R12 -1 R13 -2 R14 -7 R15  0 R16 -1 GLONASS SLOT / FRQ #
    R17  4 R18 -3 R19  3 R20  2 R21  4 R22 -3 R23  3 R24  2 GLONASS SLOT / FRQ #
    18    18  1929     7                                    LEAP SECONDS
```

Figure 3.8: Example of a compact RINEX 3 header showing the list of observation types. Fields beginning with "S" correspond to the signal-to-noise ratio (SNR) values used for GNSS-R analysis.

arc. The colors represent different elevation angles (5° yellow, 10° blue, 15° red). The missing satellite signals in the north are the result of the GPS satellite inclination angle and the station latitudes.

In order to select the more suitable values for elevation angle interval and

Figure 3.9: Reflection zones for VEN1 station. The colors represent different elevation angles (5° yellow, 10° blue, 15° red). The azimuthal angles from which the useful SNR values come from are between 150° and 280°.

azimuthal angle allowing to perform the best processing for each station, the

quickLook function has been adopted. It creates two plots (figure 3.10 and 3.11): one with periodograms for four different quadrants (northwest, northeast, southeast, southwest) and the other with the Reflector height (RH) results shown as a function of azimuth. Figure 3.11 summarizes the acceptance or rejection of RH retrievals in terms of the quality control parameters in the first panel; in the central panel the peak to noise ratios are shown; the bottom panel is the amplitude of the spectral peak. Using an elevation interval between 5 and 15 degrees, the analysis is suggesting the presence of a reflector located about 16-17 meters under the antenna position, between the azimuthal angles 150 and 270 degrees. This is further emphasized in Figure 3.10, which shows the periodograms of the SNR observations. The southeast and specially the southwest quadrants, relative to the the azimuth between 90 and 270 degrees, identify the presence of a reflector around 17 meters under the antenna. The northern part is a dead zone for water reflections, as expected from the absence of sea surface.

This initial investigation is therefore essential for the decision of the analysis

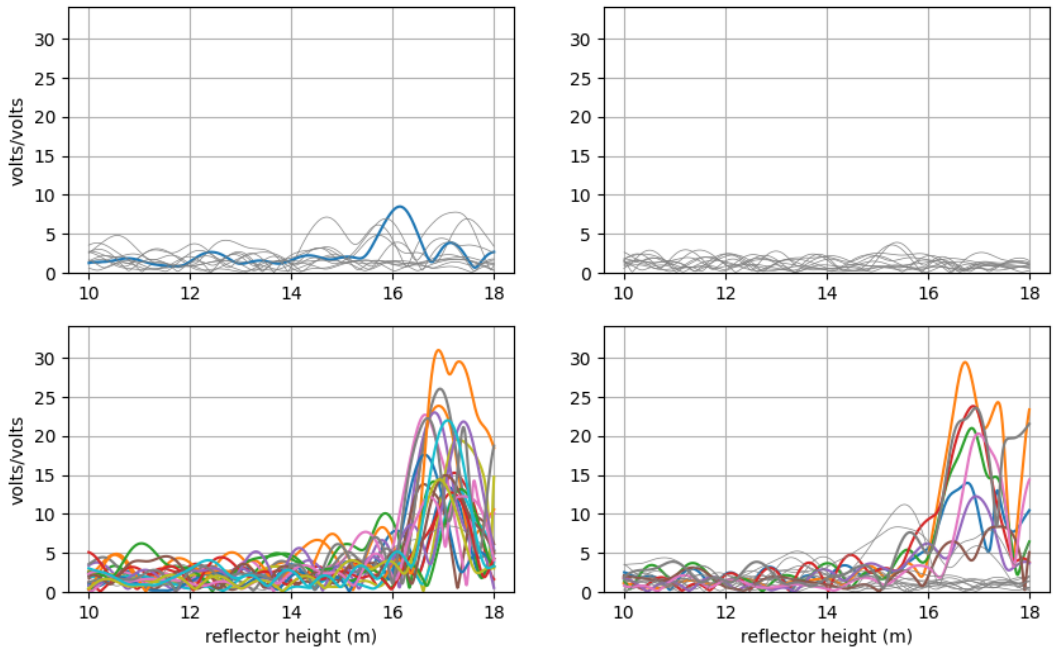

Figure 3.10: Periodograms of SNR observations for the VEN1 station, separated by quadrant. The spectral peaks indicate the presence of a sea-surface reflector approximately 17 m below the antenna, mainly in the southeast and southwest directions.

strategy. The function *gnssir_input* sets the Lomb-Scargle analysis strategy that will be used in the estimation of the reflective surface, collecting all the input information regarding station coordinates, elevation angle range, expected reflector height range, peak-to-noise value, frequencies list, and azimuth angle range.

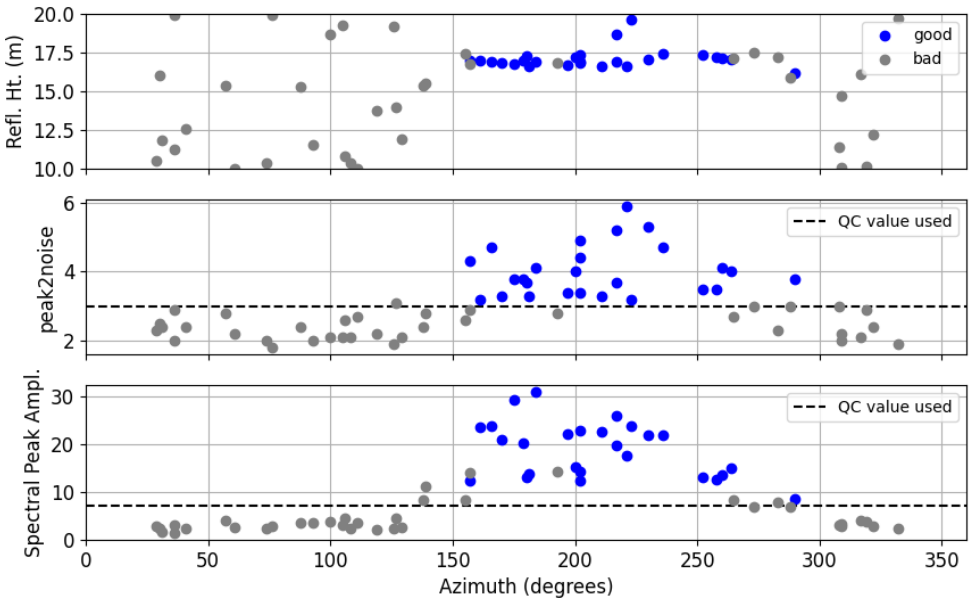

Figure 3.11: Summary of GNSS-R reflector height (RH) retrievals for VEN1 from the quickLook function. Panels show, from top to bottom: quality control flags, peak-to-noise ratios, and spectral peak amplitudes as a function of azimuth.

These parameters are then used as configuration for the calculation phase, accomplished using the function *gnssir*, the main driver for estimating reflector heights. The output for each single day are lastly combined in a unique solution with the *subdaily* function, which applies relevant corrections needed to measure water tides. This code is composed by two main sections: first it summarizes the retrievals for each constellation, identifies and removes outliers, performs a quality control on parameters; secondly, it removes more outliers based on a spline fit to the RH retrials, calculates and applies RHdot correction, and removes an inter-frequency bias.

3.6 Global ocean tidal models

The calculation of the OTL displacements is obtained from available ocean tidal models, which are models used to predict the behavior of ocean tides globally or regionally. We investigated five widely used models to analyze their regional accuracy. The selected models are FES2004 (F. Lyard et al., 2006), FES2014b (F. H. Lyard et al., 2021), TPXO9-Atlas (Egbert et al., 2002), GOT4.10c (R. D. Ray, 2013), and EOT20 (Hart-Davis et al., 2021) (see Table 3.4).

The global finite element solution FES2014b was developed, implemented and

validated through a collaborative effort involving private enterprises and public institutions, in partnership with the Centre National d'Études Spatiales (CNES) and the Institut du Développement et des Ressources en Informatique Scientifique (IDRIS). The tidal constants are derived from the tide gauge and satellite altimetry (TOPEX/POSEIDON and ERS) sea level analysis. The tide elevation data are available for 34 tidal constituents, distributed on 1/16° grids (amplitude and phase). This model is the advancement in data assimilation and model resolution of FES2004, which relies primarily on satellite missions such as TOPEX/Poseidon and Jason-1, offering a resolution of 1/8° x 1/8° and modeling 15 tidal constituents.

The TPXO9-Atlas model is a series of fully-global models of ocean barotropic tides, which best-fits, in a least-squares sense, the Laplace Tidal Equations and assimilated data. It was developed at Oregon State University and represents a more recent version of the global solution described by Egbert et al. (2002). This model was produced using data from TOPEX/POSEIDON and Jason 1 satellite altimetry, GRACE, and tide-gauge observations in areas with complex coastal relief and polar regions. It includes gridded harmonic constants of relative sea-surface elevations for eight primary, 3 non-linear tides, and 9 and 11 minor tides, at 1/30° of spatial resolution.

The ocean tide model EOT20 is the latest in a series of global ocean tide models developed at DGFI-TUM. It is derived from the collection over 18 years of data from a harmonic analysis of multi-mission altimetry data (TOPEX/POSEIDON, Jason-1, 2, ERS2, and ENVISAT). Both the ocean and load tide models are provided with a spatial resolution of 1/8° for 17 tidal constituents.

The ocean tide model GOT4.10c developed by the Goddard Space Flight Center is based on a harmonic analysis of satellite altimetry data (TOPEX/Poseidon, Jason-1, Jason-2, ERS-2, and ENVISAT), along with tide gauge measurements. The model assimilates over two decades of altimetry data and includes a range of tidal constituents, with a spatial resolution of 1/2° for 26 primary and minor tides.

Figure 3.12 shows the spatial resolution maps of FES2014, GOT4.10c, EOT20, and TPXO9 models, considering the Northern Adriatic region as an example. FES2004 model has the same resolution as EOT20, therefore it is not illustrated in the figure.

Table 3.4: Characteristics of the global ocean tidal models considered, including assimilated datasets and spatial resolution.

Model	**Data Assimilated**	**Resolution**
FES2004	T/P, ERS-2, Jason-1, Envisat, TG	1/8°
FES2014b	T/P, ERS-1/2, Jason-1/2, Envisat, TG	1/16°
TPXO9	T/P, ERS-1/2, Jason-1/2, Envisat, TG	1/30°
EOT20	T/P, ERS-2, Jason-1/2, Envisat	1/8°
GOT4.10c	ERS-1/2, GFO, Jason-1/2, ICESat	1/2°

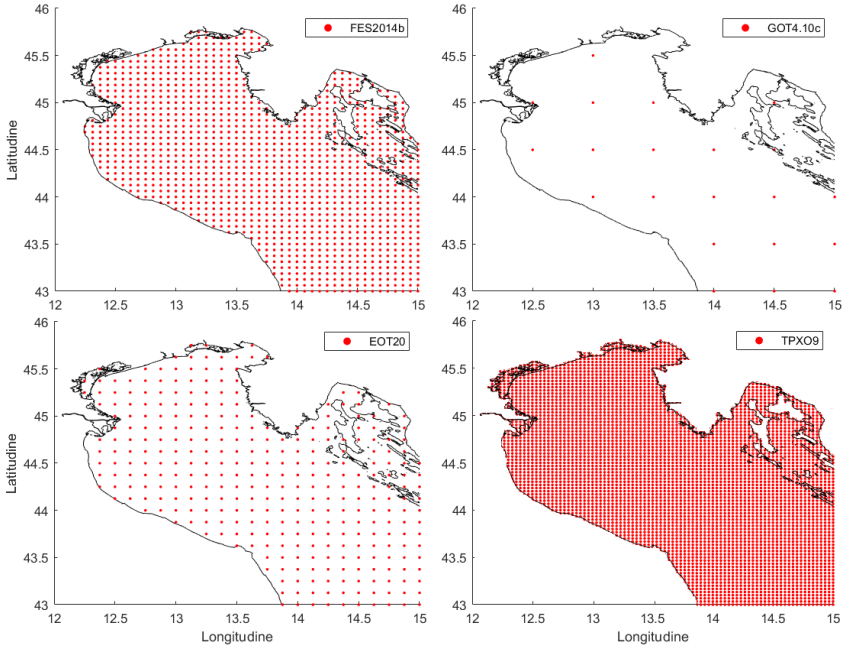

Figure 3.12: Spatial coverage and grid resolution of the FES2014b, GOT4.10c, EOT20, and TPXO9-Atlas ocean tide models in the northern Adriatic region. The FES2004 model is not shown, as it shares the same resolution as EOT20.

Chapter 4

GNSS processing techniques for OTL estimation

4.1 GNSS post processing adjustments

The presence of outliers in GNSS time series can be related to variations in GNSS positional accuracy, which depends on different types of factors (Ordóñez et al., 2011), such as: errors in the satellite and receiver clocks, accuracy in the determination of atmospheric delays, errors in satellite ephemerides, and satellite geometry.

To identify and remove outliers from the time series, we employed a robust iterative editing procedure based on a 3-sigma rejection criterion. First, gross outliers with absolute values exceeding a fixed threshold were eliminated. Subsequently, statistical outliers were iteratively removed by identifying data points whose absolute deviation from the median exceeded three times the standard deviation of the series. Unlike conventional sigma-clipping based on the mean, this approach uses the median as a central tendency measure to reduce sensitivity to existing outliers, providing a more reliable filter for non-Gaussian or contaminated datasets. The process was repeated until no additional outliers were detected, ensuring stable and clean input for subsequent analyses.

GNSS coordinate time series typically contain not only the geophysical signals of interest but also long-term trends and periodic components (Geoffrey Blewitt et al., 2002, Dong et al., 2006). In particular, GNSS station position estimates are well known to exhibit a linear secular trend, primarily associated with tectonic plate motion or site-specific processes such as subsidence, and seasonal signals, dominated by annual and semi-annual oscillations, which are commonly attributed to surface mass loading (e.g. hydrological, atmospheric), monument instability, and other local environmental effects. To isolate the residual time

series from these deterministic components, the following parametric model is fitted to each coordinate component $X(t)$

$$X(t) = \beta_0 + \beta_1 t + A_1 \cos(\omega_1 t) + B_1 \sin(\omega_1 t) + A_2 \cos(\omega_2 t) + B_2 \sin(\omega_2 t) \quad (4.1)$$

where β_0 represents the initial offset, β_1 is the linear rate, (A_1, B_1) describe the annual cycle, (A_2, B_2) describe the semi-annual cycle. The parameters are estimated using a least-squares adjustment, with the design matrix composed of a constant, a linear term in time, and pairs of sinusoidal functions corresponding to the annual and semi-annual harmonics. The fitted model is then subtracted from the original series, yielding the detrended time series.

4.2 Ocean tidal loading and model predictions

Tidal forces on Earth are primarily generated by the gravitational attraction between Earth and nearby astronomical bodies, with the most significant contributions from the Moon and the Sun. These forces can be described using the concept of gravitational potential, wherein the total potential is the cumulative sum of individual potentials exerted by each celestial body, according to the superposition principle. The tidal generating (see chapter 2.2) potential is frequently represented as a sum of harmonic components (Doodson et al., 1997; Petit et al., 2010).

OTL is the result of variations in ocean mass distribution caused by tidal forces, which induce surface displacements. These displacements are computed by convolving Lattice Green's functions, as described by Farrell (1972), with a specified model (Martens et al., 2016).

To predict modeled displacements, the Ocean Tide Loading provider, available at `http://holt.oso.chalmers.se/loading/`, supplies 11 pairs of amplitudes and phases for the principal ocean tidal constituents. These constituents are provided in the blocking-less queuing (BLQ) format and include coefficients for three long-period tides (Mf, Mm, Ssa), four diurnal tides (K_1, P_1, P_1, Q_1), and four semi-diurnal tides (M_2, S2, N_2, K_2).

The HARDISP Fortran code, accessible via the International Earth Rotation and Reference Systems Service (IERS) at `ftp://tai.bipm.org/iers/conv updt/chapter7/hardisp/HARDISP.F`, utilizes these tidal coefficients to com-

pute three-dimensional displacements at specific locations. The comprehensive set of 342 tidal constituents, as recommended by the IERS, is derived from the aforementioned 11 loading coefficients. Interpolation is performed in the complex domain, allowing the admittance to be determined for the primary tidal components. Spline interpolation is used to obtain the real and imaginary parts across all frequencies. Subsequently, these complex values are transformed back into the time domain to yield amplitudes and phases. The final displacement Δd for each component is calculated by summing the contributions from the complete set of tidal constituents as follows:

$$\Delta d = \sum_{j} A_{dj} cos(\chi_j(t) - \phi_{dj}) \tag{4.2}$$

where j is the index for tidal constituent, A_{dj} is the amplitude of the response for chosen location, $\chi_j(t)$ is the astronomical argument in radiant for the tide, and ϕ_{dj} is the phase of the response for chosen location.

4.3 DD and PPP ocean tidal loading estimations

As explained in the previous chapter 3.4, in GNSS data analysis, two main processing strategies are widely used: the Double-Difference (DD) and the Precise Point Positioning (PPP) approaches. The DD technique, based on differencing simultaneous observations between multiple satellites and receivers, effectively eliminates most common-mode errors such as satellite and receiver clock offsets, enabling robust estimation of relative displacements and fast ambiguity resolution (Khan et al., 2002; Allinson, 2004; King et al., 2005). This method has long been a standard in geodetic applications, particularly for regional deformation and OTL detection studies.

The PPP approach, on the other hand, estimates station coordinates directly in a global reference frame by using precise satellite orbit and clock products (Zumberge et al., 1997). Historically, PPP faced challenges due to the inability to resolve carrier-phase ambiguities as integers, which limited its accuracy and convergence time. However, significant advances in PPP Ambiguity Resolution (PPP-AR) techniques now allow for integer ambiguity fixing by accounting for satellite dependent biases through observable-specific bias products (Loyer et al.,

2012; Geng et al., 2022). These developments have considerably improved PPP precision, making it increasingly competitive with DD solutions for geophysical applications such as OTL estimation (Abbaszadeh et al., 2020; Wei et al., 2021; Ait-Lakbir et al., 2023; Matviichuk et al., 2023; Wang et al., 2023).

Recent studies have demonstrated that GNSS-derived OTL estimates can not only validate global ocean tide models but also reveal local discrepancies related to coastline geometry, bathymetry, and elastic Earth structure (Abbaszadeh et al., 2020; Wang et al., 2023; Ait-Lakbir et al., 2023). Nevertheless, the extent to which DD and PPP (including PPP-AR) yield consistent OTL results under varying tidal environments remains an open question.

The main objective of this study is to conduct a methodological and feasibility assessment of the DD and PPP approaches for detecting and quantifying OTL signals from GNSS coordinate time series. Specifically, we perform a comparative analysis in two contrasting tidal environments, an open-ocean site characterized by strong loading effects and a semi-enclosed basin with weaker tides, focusing on the dominant diurnal and semi-diurnal constituents (M_2, N_2, K_2, O_1, Q_1, P_1, K_1). The semi-diurnal constituent S_2 is not considered, since no atmospheric tidal loading model was applied during the processing, and this constituent could therefore be biased as a result. By systematically evaluating the performance, sensitivity, and limitations of both approaches, this study aims to establish the practical feasibility of using each method for reliable OTL estimation and to provide methodological insights for future GNSS-based geophysical investigations.

We first discuss the results based on the root-mean-square (RMS) variations of the time series without applying an ocean tidal correction and then with the OTL correction on displacement applied. Second, we conduct a tidal analysis to compare the observed tidal displacements with the available OTL models and study the differences between observations and models.

4.3.1 Impact of OTL correction on GNSS accuracy

Figure 4.1 presents a four-day snapshot of the solution for CASC using the DD and PPP techniques, compared to the OTL time series modeled using FES2014b and generated with the HARDISP software. The black line represents the hourly GNSS observations, while the blue curve represents the smoothed observations obtained by applying a low-pass finite impulse response (FIR) filter with a cut-off period of 8 hours (corresponding to a cut-off frequency of 0.125 h^{-1}). This

filtering mitigates scattering effects caused by short-period variability, reduces abrupt variations, and yields a curve that is more comparable to the OTL model (red line). The vertical component exhibits the largest variations, ranging from approximately -50 to 100 mm in PPP solutions and -50 to +50 in DD's, reflecting the strong influence of OTL on this component. In general, the Up component of the OTL displacement exhibits amplitudes approximately three times greater than the East component and up to five times greater than the North component, regardless of the processing technique applied. The PPP solution reflects the absolute effect of the OTL on the position of each station, whereas the DD solution is relative to the baseline between two stations; as a result, the signal appears with reduced amplitude in the second approach. In the DD solution, the OTL signal is derived from the difference in displacement effects between the two stations.

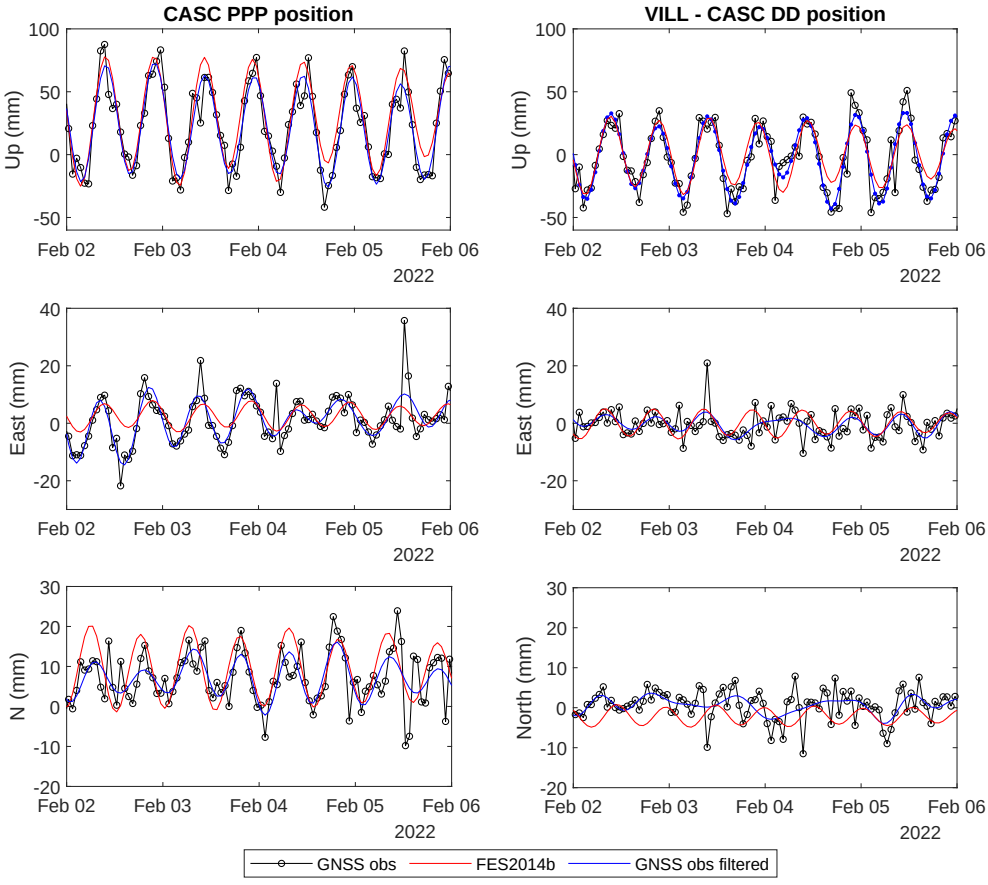

Figure 4.1: Four-day snapshot of the position solutions for CASC, using the DD (right panels) and PPP (left panels) techniques (black line), and compared against the modeled OTL displacements derived from the FES2014b model (red line). The blue curve represents the smoothed observations produced by applying a low-pass filter to mitigate scattering effects caused by periodic variations with periods shorter than eight hours.

The dataset was processed in two distinct phases. In the first phase, the data were processed using the previously described strategy for both positioning techniques with no correction applied for OTL effects. In the second phase, the data were reprocessed with the inclusion of OTL corrections implemented using the global ocean tidal model FES2014b. The bar chart (Figure 4.2) presents the RMS values (in millimeters) for both processing strategies across three coordinate components Up, East, and North for the two stations. In all components, the

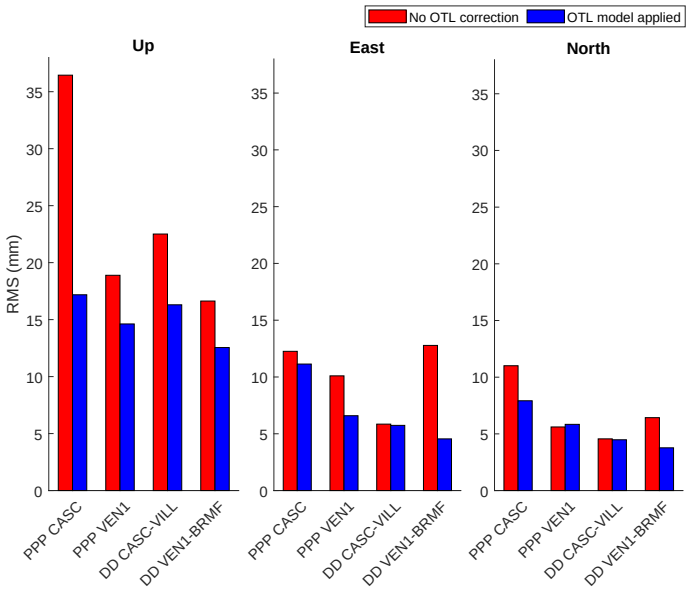

Figure 4.2: Bar chart of the RMS values of CASC and VEN1 time series processed with PPP and DD strategies, without applying any correction for the OTL effect (red) and applying FES2014b ocean tidal model (blue).

incorporation of the OTL model consistently leads to a reduction in RMS values, reflecting improved stability and precision in the GNSS solutions. The effect is most pronounced in the vertical component, where tidal loading typically has the largest impact on station displacements, leading to at least a 22% reduction in the RMS of station positions.

It is evident that the OTL has a strong impact on GNSS position estimation, leading to a significant displacement in the order of mm up to cm, depending on the station location. The residual RMS decreased across all components, most markedly in the vertical, confirming that the bulk of the loading signal is captured. Correcting for this loading and optimizing the models is essential to evaluate other types of perturbing sources and effects.

	Up (mm)		East (mm)		North (mm)	
	No	Applied	No	Applied	No	Applied
PPP CASC	36.4	17.1	12.2	11.1	11.0	7.9
PPP VEN1	18.8	14.6	10.1	6.5	5.6	5.8
DD CASC-VILL	22.5	16.3	5.8	5.7	4.5	4.4
DD VEN1-BRMF	16.6	12.5	12.7	4.5	6.4	3.7

Table 4.1: RMS values of CASC and VEN1 time series processed with PPP and DD strategies, without applying any correction for the OTL effect (Column "No") and applying FES2014b ocean tidal model (Columns "Applied").

4.3.2 Tidal analysis and ocean model comparison

The selection of the major constituents included in the tidal analysis was guided by the Rayleigh criterion, which provides a resolution criterion based on the frequency difference and the length of the observation period. According to the Rayleigh criterion (Godin, 1972), two frequencies can be resolved if their absolute difference is greater than or equal to the inverse of the observation period length. This criterion is crucial in harmonic analysis, as it helps assess whether the frequencies of interest can be accurately distinguished. For example, to estimate independently M_2 and S_2 a observation period of at least 14.77 days is necessary; to separate S_2 from K_2 182.6 days are required (Pugh et al., 2014). The Rayleigh criterion, combined with the Nyquist frequency, ensures that both the resolution and the sampling rates are sufficient for distinguishing between closely spaced tidal constituents and avoiding potential errors in frequency identification. The Nyquist frequency regards the sampling rates and establishes the maximum frequency that can be accurately reconstructed without aliasing, meaning without spurious spectral overlaps. It is defined as half of the sampling rate and represents the upper limit beyond which higher-frequency components cannot be correctly resolved, leading to distortions and misinterpretations in spectral analysis (Shannon, 1949).

The tidal analysis was performed using the versatile tidal analysis software developed by M. G. G. Foreman et al. (2009), considering the 7 frequency components to resolve in this study (K_2, M_2, N_2, K_1, P_1, O_1, and Q_1).

To assess the accuracy and effectiveness of the tidal analysis, we applied the methodology to a synthetic time series generated using the HARDISP code. This

synthetic dataset was used to compute the displacement at the CASC station over a six-months interval, based on the FES2014b tidal model. To make the synthetic curve more realistic, Gaussian noise was added to the data, resulting in a noise level comparable to that of GNSS measurements and for each noise level 30 independent realizations are performed to ensure statistical robustness of the estimated parameters. For CASC station the noise was 14.6 mm for PPP, and 13.6 mm for DD. In table 4.2 the differences between the model amplitudes and the calculated amplitudes are shown, as well as the standard errors on the estimates for PPP solutions. Table 4.3 summarize the results for DD solutions.

The results indicate that all main tidal constituents are accurately retrieved,

Table 4.2: PPP estimated amplitude residuals and retrieval error (mm) of the ocean tidal components obtained from the tidal analysis of the synthetic time series with added noise at CASC for the vertical component in mm.

	K_2	M_2	N_2	K_1	P_1	O_1	Q_1
Res A	0.03	0.04	0.17	0.00	0.09	0.03	0.29
Error	0.41	0.42	0.70	0.61	0.42	0.27	0.31

Table 4.3: DD estimated amplitude residuals and retrieval error (mm) of the ocean tidal components obtained from the tidal analysis of the synthetic time series with added noise at CASC for the vertical component in mm..

	K_2	M_2	N_2	K_1	P_1	O_1	Q_1
Res A	0.06	0.02	0.14	0.03	0.22	0.14	0.30
Error	0.28	0.29	0.42	0.39	0.31	0.35	0.28

with amplitude residuals generally below 0.2 mm. For both processing strategies, the Q_1 estimates fall below the detection threshold, indicating that this constituent cannot be reliably resolved at the present noise level and time span. The retrieval errors are consistent with the imposed noise levels, confirming the robustness of the harmonic analysis. As expected, DD solutions exhibit slightly smaller uncertainties than PPP, reflecting the partial mitigation of common-mode errors through differencing. The residual amplitude differences remain well within the millimeter level, demonstrating that the analysis setup is capable of resolving the target tidal constituents even under realistic noise conditions.

Following this analysis, an additional test was performed to assess the influence of baseline length on the DD solutions. Specifically, we evaluated the

ratio between the retrieved amplitude and its standard error under varying noise conditions and baseline separations. Although the DD method largely mitigates common satellite and receiver errors, such effects are not completely removed for long baselines. When the inter-station distance increases to 500–600 km, the residual orbit and clock errors are no longer fully correlated between sites and can reach the centimeter level, partially masking the millimeter-scale tidal signal. In the study, the choice of long baselines was deliberate; the effect at VEN1 is very small, and it was necessary to perform the differencing with a reference station where the loading signal was even smaller, otherwise, the resulting differential displacements would have been on the order of, or below, the GNSS noise level.

The relationship between the amplitude-to-standard-error ratio (A/se) and the imposed noise level is shown in Figure 4.3 and Figure 4.4 for the M_2 constituent. For VEN1, the chosen baseline with BRMF (approximately 500 km)

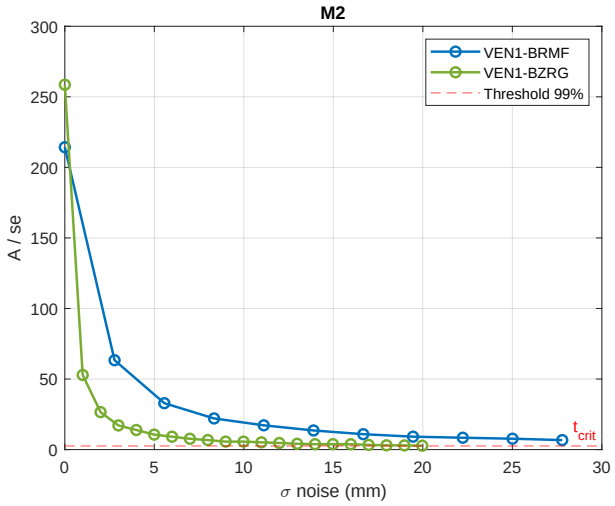

Figure 4.3: Dependence of the M_2 constituent detectability on baseline length for the VEN1 station. The plot shows the ratio between amplitude and standard error (A/se) as a function of imposed noise level for different baselines, highlighting improved detectability for the longer VEN1–BRMF baseline compared to the shorter VEN1–BZRG pair.

exhibits higher ratio values than the shorter VEN1–BZRG baseline (150 km), indicating a more robust retrieval of the tidal signal despite the longer separation. This behavior confirms that the detectability of the tidal constituent also depends on the relative amplitude difference between the two sites. When the local loading response is weak, a baseline toward a site with an even smaller tidal effect maximizes the measurable differential signal. The shorter baseline falls below the 99% detection threshold more rapidly as the noise level increases, revealing its lower resilience to observational noise.

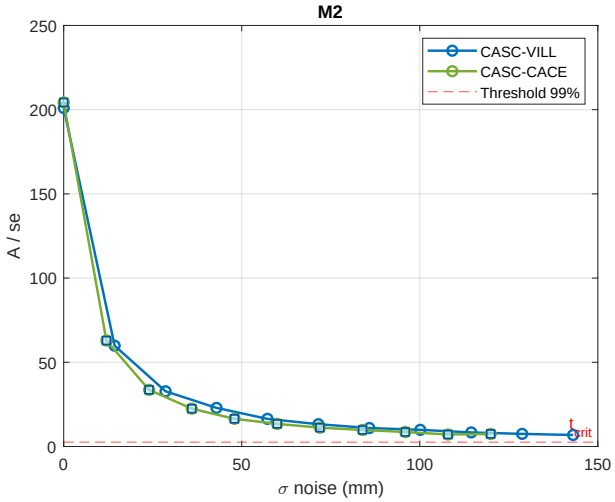

Figure 4.4: Dependence of the M_2 constituent detectability on baseline length for the CASC station. The figure compares amplitude-to-error ratios for the CASC–VILL (500 km) and CASC–CACE (280 km) baselines, illustrating more stable retrievals for longer separations.

A similar behavior is observed for the CASC station, where two baselines were analyzed, CASC–VILL (about 500 km) and CASC–CACE (280 km). Also in this case, the longer baseline maintains higher ratios across the tested noise range, confirming a more stable retrieval of the M_2 constituent.

Overall, these tests demonstrate that the detectability of the OTL signal in DD solutions is a combined function of baseline length, relative tidal amplitude between stations, and data noise, and that an optimal configuration may not necessarily correspond to the shortest baseline.

To further evaluate the influence of the observation window on tidal constituent retrieval, an additional test was performed using synthetic OTL time series and contaminated with Gaussian noise representative of the VEN1 GNSS data. The analysis was repeated for progressively longer subsets of the time series, and for each case the ratio between the estimated amplitude and its formal standard error was computed to quantify the detectability of each constituent. The results, shown in Figure 4.5, reveal a clear dependence of tidal resolution on record length. The ratio values increase systematically with the duration of the series, with the dominant constituents (M_2, K_1) reaching the significance threshold earlier than the weaker components (P_1, O_1, K_2). PPP solutions display a steeper increase in A/se compared to DD, indicating a faster improvement in constituent detectability as the observation period extends. For record lengths shorter than approximately six months, only the main semidiurnal and diurnal constituents exceed the confidence level, whereas longer records approach con-

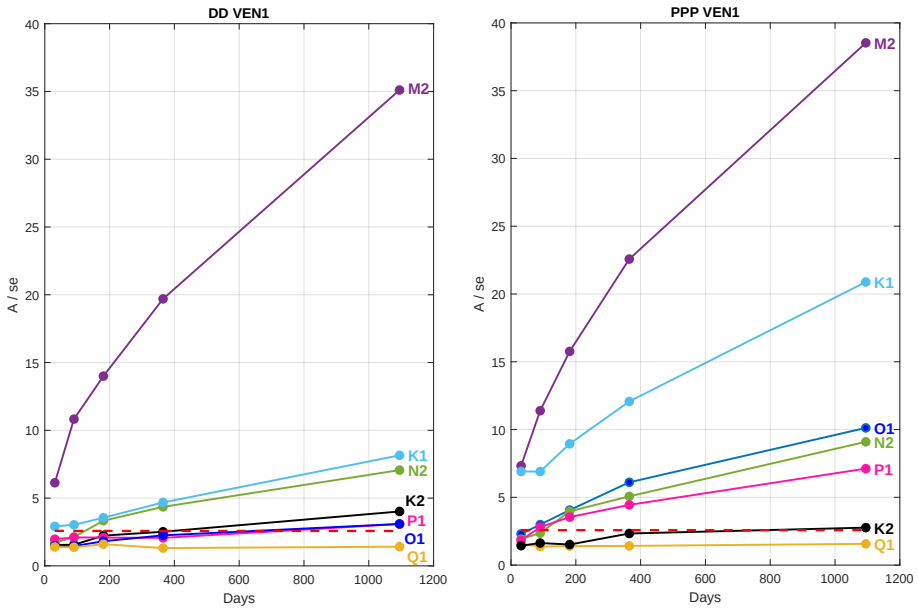

Figure 4.5: Dependence of tidal detectability on time series length for VEN1. Curves show the ratio between the amplitude and its standard error (A/se) for each constituent estimated over progressively longer time windows for DD (left) and PPP (right) solutions.

vergence for secondary components. This test confirms that extending the GNSS time span substantially improves the reliability and completeness of tidal constituent recovery, particularly in low amplitude tidal environments such as VEN1. For the selected time interval of 220 days, for the PPP solutions Up component at VEN1 the expected resolved OTL constituents should therefore be M_2, N_2, K_1, P_1 and O_1, while for DD only M_2, N_2 and K_1.

The results for CASC Up component are shown as well in Figure 4.6. For the selected time interval of 220 days, for the PPP solutions Up component at CASC the expected resolved OTL constituents should therefore be all the analyzed one except for Q_1, while for DD all except for Q_1 and P_1.

The harmonic analysis was performed on the GNSS-derived coordinate time series for CASC and VEN1 stations using both PPP and DD techniques. The estimated amplitudes of the main tidal constituents were compared with the corresponding predictions from five global ocean tide models: FES2004, FES2014b, TPXO9-Atlas, GOT4.10c, and EOT20. Figures 4.7 and 4.8 summarize the results for the vertical, east, and north components at each station. For clarity, only those constituents whose amplitudes exceed the adopted significance threshold are displayed. An exception was made for P_1 and K_1 in some cases and it is

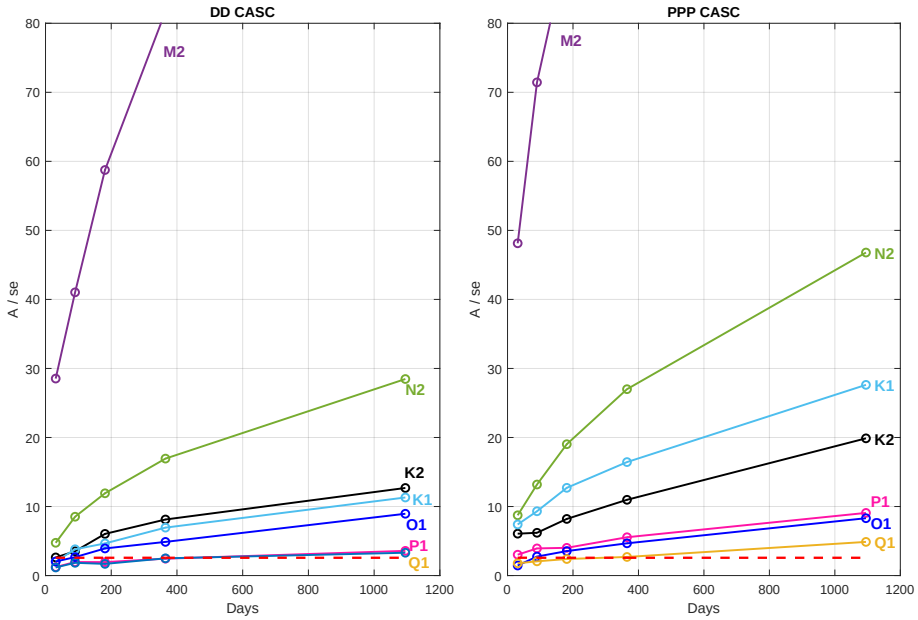

Figure 4.6: Dependence of tidal detectability on time series length for CASC. Curves show the ratio between the amplitude and its standard error (A/se) for each constituent estimated over progressively longer time windows for DD (left) and PPP (right) solutions. A zoom on the weakest components compared to M_2 was done, to make possible to understand their behavior.

explained through the results interpretation.

At CASC, located along the Atlantic coast and affected by strong tidal loading, the PPP and DD results exhibit clear differences in amplitude level and in the number of resolved constituents, especially in the horizontal components. In the Up component (Figure 4.7), the PPP solution captures large vertical oscillations dominated by the M_2 constituent, with amplitudes of about 28–30 mm, matching closely the model predictions. The secondary constituents N_2 and K_2 are also well resolved, with amplitudes of approximately 7 mm and 3.5 mm respectively, showing sub millimetric differences with the models. The diurnal constituent O_1 appear clearly in the PPP solution, with amplitudes of roughly 2 mm. P_1 and K_1 do not exceed the significance threshold, even though the synthetic test clearly shows a strong A/se ratio, especially for K_1 which is the second largest component in the synthetic test, whose observed values reaches only 2.48.

By contrast, the DD solution at CASC shows a reduction in signal amplitude, as expected for relative positioning with a long baseline to the reference station. In the Up component, the dominant M_2 amplitude is around 20 mm, while the N_2 and K_2 components reach approximately 4 mm and 2.5 mm, respectively. The K_1 constituent is again not significant in the DD vertical series and falls below

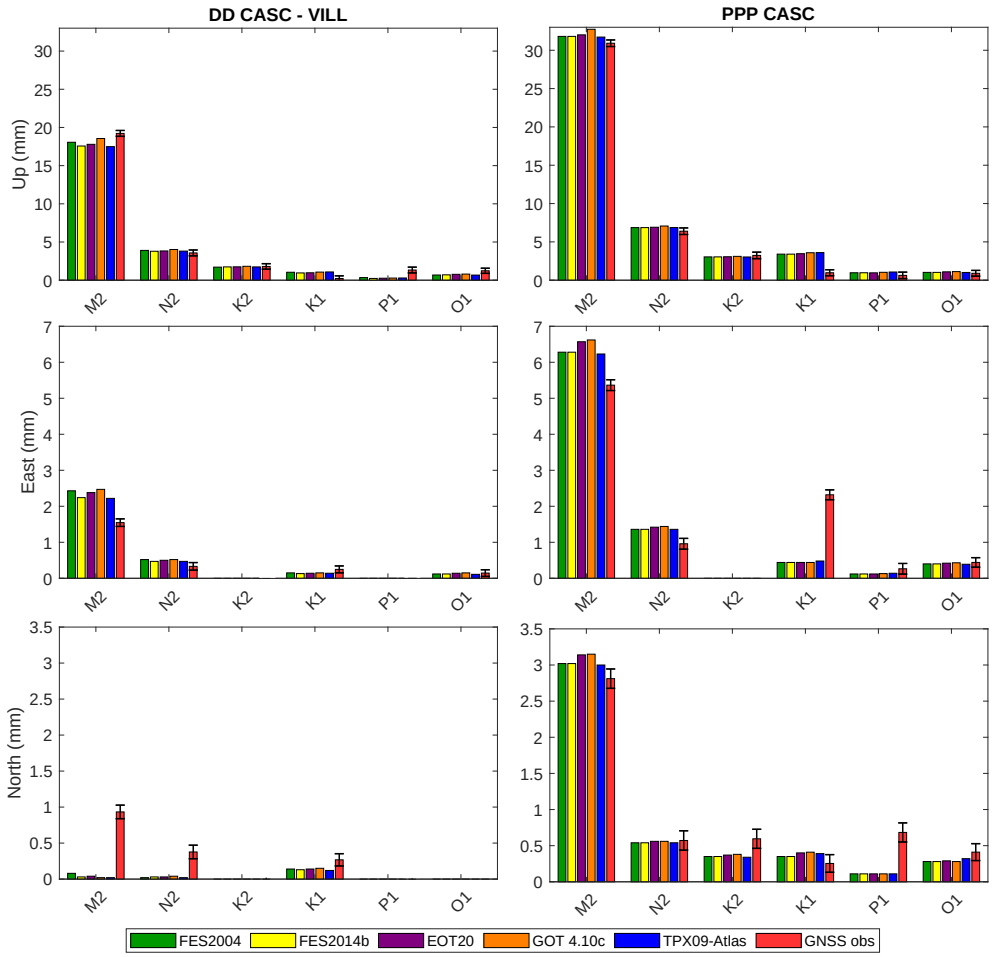

Figure 4.7: Tidal analysis results of CASC processed with DD respect to VILL (left) and PPP (right) strategies for Up, East and North components in red compared with previously listed global ocean models.

the detection threshold. For this technique, a clear mis-modelling behavior is evident for K_1 and P_1; the former, which should be one of the strongest components, falls below the threshold and its estimated amplitude is far below the model predictions, while the latter, which should not be significant, is estimated with an amplitude about seven times higher than predicted. The O_1 tide remains marginally detectable, with amplitudes of about 1 mm.

In the horizontal components, the PPP and DD differences are equally evident. For the East component, the PPP solution resolves M_2, N_2, K_1 and O_1 with semidiurnal amplitudes attenuated and diurnal amplified respect to the model predictions. The relative amplitudes estimated with DD show the exact same pattern as PPP, with smaller discrepancies for K_1. The North component shows lower energy overall; PPP resolves all constituents except K_1, while DD significantly resolving M_2, N_2 and K_1, but with clear discrepancies from the models

for the semi diurnal constituents. Overall, the significant constituents are better resolved in the PPP solutions, showing smaller deviations from the models.

At VEN1, located on the northern Adriatic coast where tidal loading is weak, the overall amplitudes are one order of magnitude smaller but the differences between the two techniques remains evident. In the Up component (Figure 4.8),

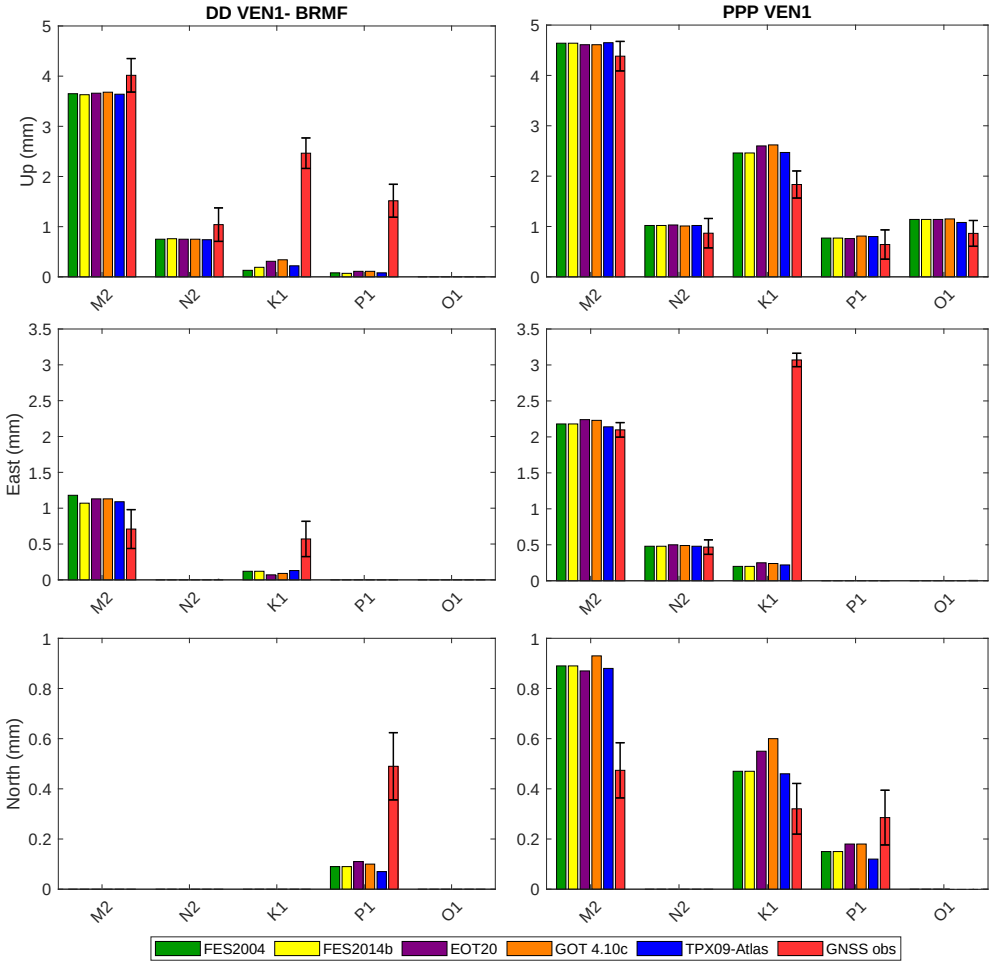

Figure 4.8: Tidal analysis results of VEN1 processed with DD (left) and PPP (right) strategies for Up, East and North components in red compared with previously listed global ocean models.

the M_2 constituent dominates with amplitudes of about 4–5 mm in the PPP solution, while the DD analysis yields values around 3–4 mm. The N_2 component is also resolved, in both PPP and DD solutions, showing good coherence with the model predictions. The diurnal constituents K_1 and P_1 are present in PPP with amplitudes below 2 mm, while in the DD results they are significant in terms of signal to noise ration, but they are not coherent with the models.

The East and North components at VEN1 display very small oscillations, reflecting the weak tidal loading in the northern Adriatic. In the East direction,

M_2 and K_1 are the only constituents exceeding the significance threshold in the DD solutions, with amplitudes differing from the model predictions by approximately 0.5 mm. All other constituents remain below the detection limit. In the PPP results, a larger number of constituents are detected: the two semidiurnal components (M_2 and N_2) closely follow the model predictions, while the diurnal K_1 exhibits an amplitude about six times higher than the models. The North component shows even smaller variability, with amplitudes consistently below 1 mm across all tidal frequencies. These results confirm that, under low-amplitude tidal conditions, the PPP technique maintains sufficient sensitivity to resolve the dominant semidiurnal and diurnal signals, whereas the DD approach captures only the strongest oscillations and suppresses the weaker components. Although statistically significant, the horizontal components display a certain degree of mismodelling with respect to the ocean tide model predictions.

We then reprocessed the data, incorporating OTL corrections using FES2014b model, and analyzed the residual ocean tidal components in the time series. The choice of the FES2014b model was motivated by its superior spatial resolution and regional coverage, especially in the vicinity of the VEN1 station, where its detailed coastal representation and improved bathymetric model provide more reliable OTL estimates. The results are shown in Figure 4.9, where the amplitudes of the tidal constituents for vertical, east and north components for both techniques are highlighted.

In both stations, the vertical component shows the largest residual amplitudes, reflecting the higher sensitivity of this component to imperfections in the applied OTL model. The CASC PPP solution exhibits the most prominent residual, associated with the diurnal K_1 constituent, reaching values above 4 mm. Significant, though smaller, residuals are also visible for the semidiurnal M_2 and diurnal P_1. In contrast, the DD residuals at CASC are markedly lower, generally below 1.5 mm for all constituents, with the strongest remaining signal in K_1.

At VEN1, the residuals are overall smaller, consistent with the weaker tidal forcing in the Adriatic Sea. However, distinct differences remain between techniques. The PPP results show a clear residual peak in the K_1 component, especially in the East direction, reaching nearly 3 mm, while M_2 and P_1 contribute at the level of about 1 mm. The DD solutions, in contrast, show residuals typically below 1 mm in all components, except for K_1 which still remains the main residual between the OT components.

Across both stations, the horizontal components display significantly smaller

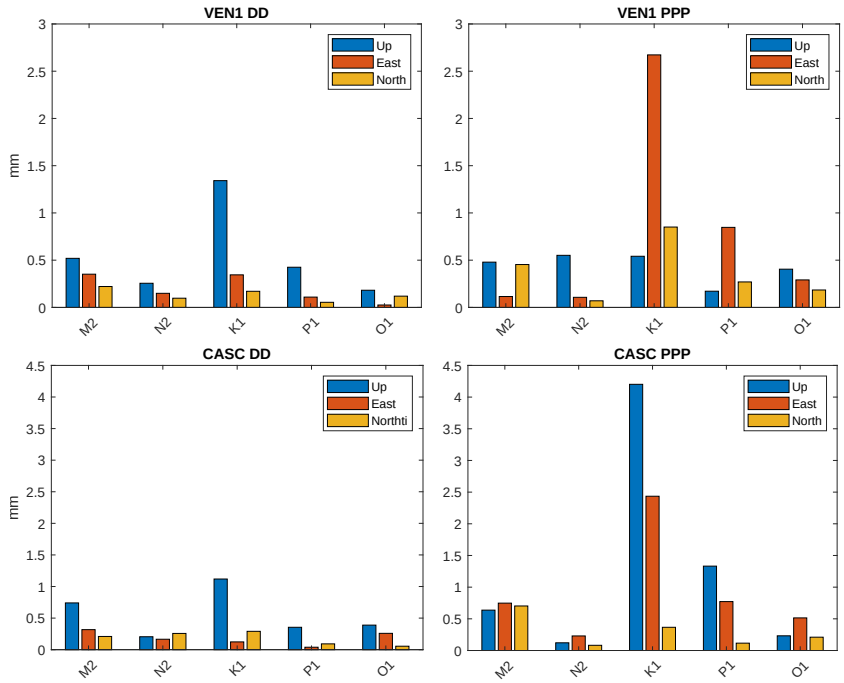

Figure 4.9: Amplitude residuals of the main tidal constituents analyzed after applying the OTL correction using the FES2014b model. The left panel shows residuals obtained with the DD processing strategy, while the right panel presents the PPP residuals.

residuals than the vertical ones, with most values within the millimeter range. The overall pattern confirms that, even after model correction, small but measurable tidal energy remains in the GNSS observations, particularly in PPP solutions. These residuals are dominated by the K_1 constituent and, to a lesser extent, by the semidiurnal M_2 and diurnal P_1 components, suggesting that small discrepancies persist between the modeled and observed OTL effects, likely due to local hydrodynamic conditions or minor model limitations in shallow and coastal regions.

To investigate whether the K_1 PPP residuals at the CASC station can be attributed to local effects (e.g., coastal morphology, bathymetry), another site was analyzed. The GAIA station, located north of CASC and approximately six kilometers inland from the coastline, was selected for this purpose. The data were processed using the PPP technique over a seven-month period, employing the same network as for CASC. The residuals, shown in Figure 4.10, reveal a pronounced unmodelled signal for the K_1 constituent, particularly in the vertical component.

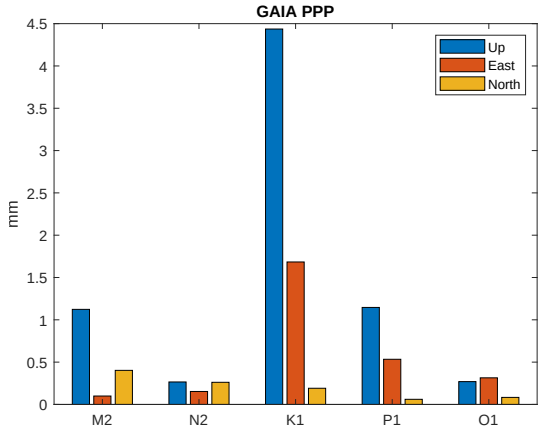

Figure 4.10: Amplitude residuals of the main tidal constituents analyzed after applying the OTL correction using the FES2014b model. Station GAIA with PPP processing.

4.3.3 Orbital aliasing in multi-GNSS time series

The advent of multi constellations such as GLONASS and Galileo has expanded the scope of multi-GNSS observations. These additional systems not only provide redundancy and improved geometry but also introduce constellation-specific errors, which manifest as orbital artifacts positioning products. Recent studies (e.g. Bogusz et al., 2016; Abraha et al., 2018) show that these artifacts can reach amplitudes of several millimeters to centimeters in station coordinate time series and tropospheric delay estimates, significantly affecting the interpretation of subtle geophysical signals. For example, Galileo introduces artifacts with dominant periods of approximately 14.08 hr, 17.09 hr, 34.20 hr, 2.49 days, and about 3.4 days, whereas GLONASS artifacts appear at 5.63 hr, 7.36 hr, 10.64 hr, 21.26 hr, 3.99 days, and about 8 days. GPS, in turn, exhibits orbital signals tied to harmonics of the K_1 tide, producing inconsistencies with geophysical tidal models of up to 12 mm in the vertical component. These signals are not uniform across the globe, in fact their magnitude depends strongly on station latitude and the geometry of satellite flybys, with equatorial sites particularly affected by GLONASS-specific artifacts (Zajdel et al., 2022).

Derived coordinates time series from GNSS can be affected by diverse types of technique errors, which influence the study and analysis of different geophysical phenomena. Several studies revealed the presence of artificial signals in GNSS position power spectra, originated from processing artifacts arising from repeat period of satellite orbits (J. Ray et al., 2008; Bogusz et al., 2016).

The aliased period of a sinusoidal signal can be calculated with the following

equation (Jacobs et al., 1992):

$$f_{alias} = |f_{true} \pm n f_{orb}| \tag{4.3}$$

f_{alias} is the observed alias frequency in the GNSS spectrum, f_{true} is the true frequency of the signal, n is an integer harmonic index, positive or negative, representing the number of orbital cycles being added or subtracted, and f_{orb} is the GNSS orbital repeat frequency (Penna et al., 2003). The GPS orbital period is 11.957 hours, which corresponds to 2.005 cycles per day; the GLONASS orbital period is 11.2941 hours, which corresponds to 2.125 cycles per day. By using the Equation 4.3 we can extract the aliasing signals relative to the high frequency peaks present in the spectrum, shown in Table 4.4.

Figure 4.11 presents the power spectra of the coordinate time series for both

Table 4.4: Real and aliased periods of principal tidal constituents in GNSS coordinate time series. T_{true} denotes the actual tidal period, while T_{alias} for GPS and GLONASS are the corresponding aliased periods calculated using Equation 4.3, based on the orbital repeat frequencies of each constellation.

Tide	f_{true} (cpd)	T_{true} (h)	T_{alias} GPS (h)	T_{alias}GLONASS (h)
M_2	1.9324	12.42	6.09	5.92
S_2	2.0000	12.00	5.99	5.82
N_2	1.8957	12.66	6.15	5.97
K_2	2.0050	11.97	5.98	5.81
K_1	1.0029	23.93	7.98	7.67
P_1	0.9295	25.82	8.18	7.86
O_1	0.9971	24.07	7.99	7.69
Q_1	0.8932	26.87	8.28	7.95

DD, in red, and PPP, in blue, solutions. The comparison highlights the distinct manifestation of orbital artifacts depending on the processing strategy, for the interval of signals with a period between 4 and 10 hours. In the PPP solutions, spectral peaks are more pronounced at periods corresponding to the alias frequencies of tidal constituents, particularly around 5.98 h and 7.98 h, which are consistent with the theoretical aliasing of the M_2, S_2, and K_1 tides (see Table 4.4). In contrast, the DD spectra show a reduction in the amplitude of these artifacts, even though there is not their complete suppression. Common-mode errors are partly absorbed through the differencing process, leading to weaker

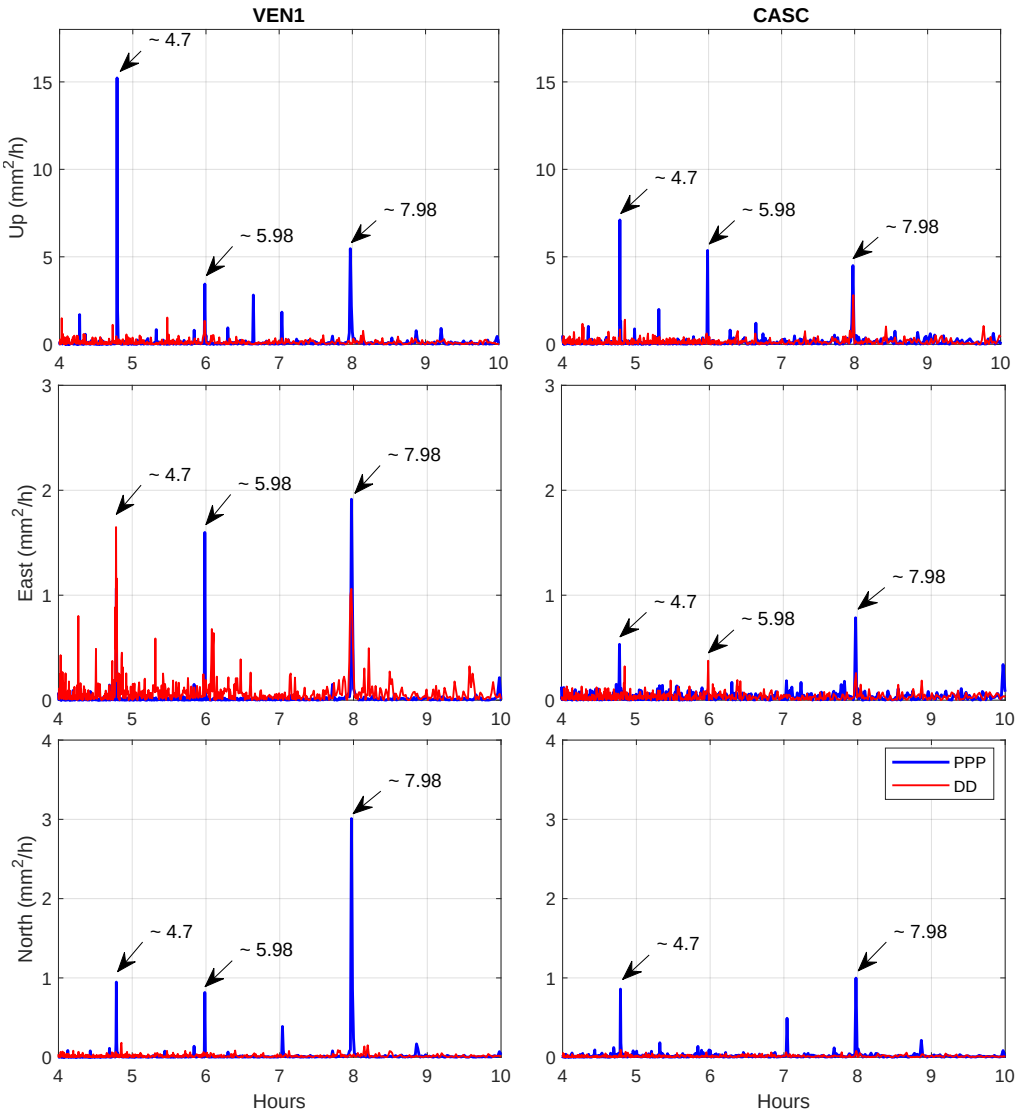

Figure 4.11: Comparison of power spectra from PPP and DD coordinate time series in the sub-daily band (4–10 h). The PPP spectra display distinct peaks near 5.98 h and 7.98 h, corresponding to alias periods of the principal tidal constituents (M_2, S2, K_1), while DD spectra exhibit reduced amplitudes of these orbital artifacts due to partial cancellation of common-mode errors.

artifact signatures. While PPP allows for global, station-independent processing, it also exposes stations more directly to constellation-specific orbital artifacts. The North component is the one which shows the greater differences between the two processing technique. DD appears to mitigate the majority of the effects due to aliasing frequencies, as visible for both stations. The vertical component is clearly the most affected by aliasing for the PPP solutions, which highlights the importance of a careful account for these periodicities to avoid misinterpretation when analyzing PPP-derived coordinates and tidal components.

Galileo constellation is also affected by orbital artifacts, and the most dominant sub-daily signals appear with periods of 9.97 h, 14.08 h, and 17.09 h. The spectral analysis highlighted only the artifact with 17.09 hours period, as shown in Figure 4.12. The 17.09 h peak is much smaller in terms of amplitude than the

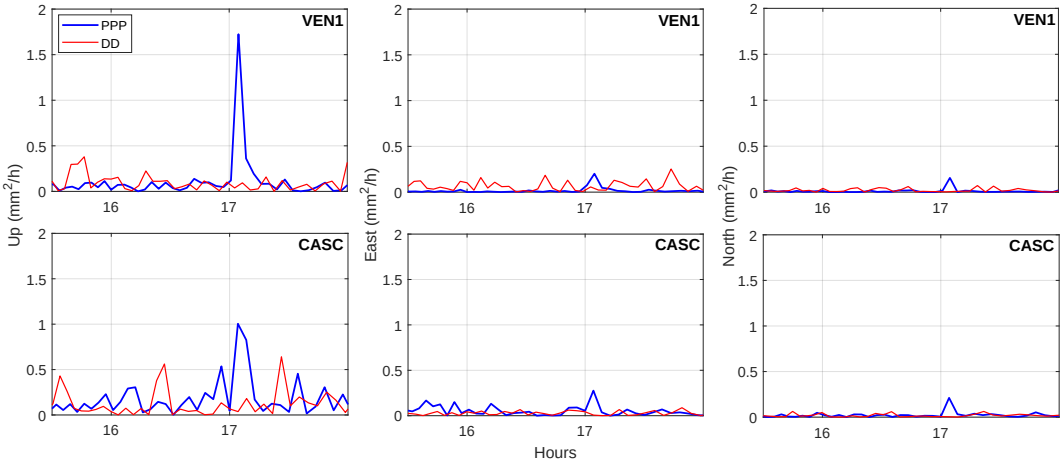

Figure 4.12: Spectral signature of the 17.09 h orbital artifact associated with the Galileo constellation. The peak is clearly visible in the PPP solutions, while in the DD time series it remains close to the noise level, indicating partial mitigation of constellation-related aliasing effects through differencing.

lower aliasing periods previously analyzed, and it is clearly evident for the PPP solutions, while in the DD time series, it remains in the order of the noise.

4.3.4 Discussion on DD and PPP results

The results presented in this study provide an assessment of the sensitivity and limitations of DD and PPP strategies in detecting and modeling OTL effects from GNSS coordinate time series. By analyzing two contrasting tidal environments, a high-energy Atlantic coastal site (CASC) and a low-energy semi-enclosed basin site (VEN1), we evaluated the capability of each processing technique to recover the amplitudes of the main tidal constituents and to quantify the residual tidal energy after applying the FES2014b correction model.

The incorporation of OTL corrections using the FES2014b model systematically reduced the RMS of all coordinate components for both techniques, confirming the model's ability to reproduce the dominant tidal loading displacements. The reduction was most pronounced in the vertical component, where OTL effects are largest, reaching up to a 22% RMS improvement overall. The horizontal

components also showed smaller but consistent improvements, indicating that the high-resolution hydrodynamic modeling effectively captures local tidal variability even in coastal and shelf regions (F. H. Lyard et al., 2021; Hart-Davis et al., 2021). The residual analysis demonstrated that, after model correction, small tidal energy remains in both techniques, dominated by the K_1 and M_2 constituents. This residual pattern indicates that the remaining signals may reflect a combination of local site effects, unmodelled processes, or minor model inaccuracies, consistent with findings from previous GNSS-based OTL evaluations (Abbaszadeh et al., 2020; Ait-Lakbir et al., 2023).

A consistent difference was observed between the two processing approaches. DD generally produced smaller residuals and slightly lower tidal amplitudes than PPP, reflecting its relative nature and the partial cancellation of loading signals common to both stations in the baseline (King et al., 2005; Dach et al., 2015). PPP, by contrast, provides an absolute estimate of the displacement referenced to the global frame and therefore reproduces the true amplitude of the loading, but remains more sensitive to systematic effects such as residual orbital errors. The larger K_1 residuals in the PPP solutions at both sites exemplify this sensitivity. The K_1 and, to a lesser extent, P_1 components correspond to the GPS orbit and constellation repeat periods, making them particularly prone to spectral contamination and aliasing in PPP-derived OTL estimates (Penna et al., 2003; King, 2006).

The use of relatively long baselines in the DD configuration represents both an advantage and a limitation. On one hand, longer baselines enhance the measurable differential OTL signal, since the tidal deformation differs more significantly between the two sites, improving the detectability of the loading effect. On the other hand, the cancellation of common-mode errors, such as atmospheric path delays, becomes less effective with increasing station separation and residuals can reach the centimeter level, partially masking the millimeter-scale tidal signal (Bos et al., 2015). The results obtained in this study confirm this trade-off. The analysis of the signal-to-error ratio at varying noise levels demonstrates that the ability to detect the M_2 constituent in DD solutions depends not only on the baseline length but also on the relative amplitude difference between stations. For VEN1, the 500 km baseline with BRMF yielded higher ratio values than the shorter 150 km baseline with BZRG, indicating that the stronger differential signal between the two sites can, in some cases, compensate for the partial loss of error cancellation. A similar behavior was observed for CASC, where the 500 km

baseline with VILL performed better than the 280 km baseline with CACE. In both cases, the shorter baselines dropped below the 99% detection threshold more rapidly as noise increased, confirming their lower resilience to observational noise. These results highlight that while long baselines introduce greater sensitivity to uncorrelated orbit and clock errors, they may still provide enhanced detectability when the tidal loading contrast between sites is sufficiently large.

The ability to resolve tidal constituents also depends strongly on the length of the time series. Longer observation periods improve frequency resolution according to the Rayleigh criterion (Godin, 1972; Pugh et al., 2014), allowing a more reliable separation of closely spaced constituents such as K_2, and N_2, and providing more stable amplitude estimates for weaker diurnal and semidiurnal tides. Extending the duration of the GNSS time series beyond one year would therefore enable the recovery of additional constituents and a more robust estimation of long-period components, as demonstrated in long-term OTL studies based on multi-year GNSS observations (Penna et al., 2015; Matviichuk et al., 2023; Wang et al., 2023). This is particularly important in environments with low tidal energy, where the short 220-day dataset used here limits the detection of minor constituents and may introduce partial aliasing between neighboring frequencies.

The aliasing issue is intrinsic to GNSS data sampling and satellite geometry. The 24-hour repetition of satellite ground tracks introduces spurious diurnal and semidiurnal signals that overlap with genuine tidal constituents. These artifacts are most evident in the PPP solutions, where no differential technique is applied. In the DD approach, the common-mode cancellation mitigates most of this aliasing, explaining the better performance observed for the diurnal K_1. Recent studies have demonstrated that combining multiple constellations (e.g., GPS, Galileo, BeiDou, GLONASS) can substantially reduce orbit-related aliasing and improve the separation of tidal frequencies (Abbaszadeh et al., 2020; Wei et al., 2021; Ait-Lakbir et al., 2023; Wang et al., 2023). In our analysis, the inclusion of multi-GNSS data already improved signal stability and noise reduction, particularly for hourly PPP estimates, but further benefits could be expected from full multi-constellation ambiguity-fixed (PPP-AR) processing (Loyer et al., 2012; Geng et al., 2022). Since the present analysis relied on float PPP solutions, the residual biases associated with fractional ambiguities likely contributed to the scatter observed in PPP amplitudes compared to DD.

The comparison between CASC and VEN1 highlights the role of local conditions in OTL recovery. At CASC, where the ocean tide loading is strong and

the absolute effect exceeds 30 mm in the vertical, both methods clearly resolve the dominant constituents (M_2, N_2, K_2, K_1, O_1). At VEN1, where the expected OTL is only 5–8 mm, the reduced signal-to-noise ratio amplifies the impact of modelling. Here, PPP still resolves the main constituents, especially in the up. In the east component K_1 dominates the OTL signal with a large discrepancy with the models, while DD shows reduced sensitivity and occasionally fails to detect the smallest signals. These differences confirm that the apparent performance of each method depends strongly on site-specific factors such as tidal regime, satellite visibility, multipath environment, and local atmospheric variability (Yuan et al., 2013; Penna et al., 2015).

The observed mismodelling of the K_1 and P_1 constituents may also stem from the difficulty of separating nearby frequencies given the limited length of the time series. Although the synthetic test and the Rayleigh criterion indicate that the two constituents should be separable and resolvable, and the harmonic analysis shows no significant correlation between them, additional contributions cannot be excluded. In particular, the diurnal atmospheric tide S_1, whose frequency is very close to the K_1 and P_1 bands, may influence the estimated amplitudes. Unlike oceanic tidal constituents, S_1 has a predominantly thermal and atmospheric origin, as diurnal solar heating drives oscillations in surface pressure at diurnal (S_1) and semi-diurnal (S_2) periods, as well as higher-frequency harmonics. These atmospheric tides induce periodic loading of the Earth's surface, resulting in measurable vertical deformations at GNSS stations. Recent studies have shown that the amplitude of vertical deformation associated with atmospheric tides can reach several millimeters, comparable in magnitude to some ocean tidal loading components (Li et al., 2018). Consequently, the potential superposition of atmospheric and oceanic loading effects in the diurnal band remains an open issue and warrants further investigation.

An additional aspect emerging from both stations is that the PPP solutions tend to resolve a larger number of significant tidal constituents in the horizontal components compared to the DD results. This tendency is observed at both sites and appears largely independent of the local tidal regime. It likely reflects the fact that the absolute positioning framework of PPP can preserve more of the small-amplitude horizontal signals that may be partially attenuated in the differencing solutions. In contrast, the relative nature of DD, while efficient in reducing common-mode errors, can suppress weaker oscillations, especially when the differential signal between stations is close to or below the noise level. This

difference in spectral richness between PPP and DD is evident at both CASC and VEN1 and highlights the advantage of PPP in capturing a more complete tidal spectrum in the horizontal plane, albeit with slightly higher noise levels (Abbaszadeh et al., 2020; Wang et al., 2023).

Several methodological limitations must be acknowledged. The long baselines in the DD configuration mean that residual orbit and clock errors are not fully cancelled, potentially biasing the estimated amplitudes at the millimeter level. Even so, our results show that for VEN1–BRMF and CASC–VILL ($\sim$ 500 km), the stronger differential OTL signal partly compensates for this effect, yielding higher signal-to-error ration than shorter baselines. Second, the PPP analysis was conducted using float solutions without ambiguity resolution, which limits precision compared with PPP-AR implementations now available in modern processing frameworks. Third, the limited duration of the time series restricts the separability of close tidal frequencies; according to the Rayleigh criterion, longer series ($\geq$ 1 year) are required to fully resolve smaller constituents such as Q_1 and K_2, and short records may lead to partial aliasing between nearby frequencies.

Chapter 5

Tidal analysis in the northern Adriatic region

The northern Adriatic Sea represents a particularly compelling environment for the study of ocean tides. Unlike many regions of the Mediterranean basin, which are characterized by weak tidal amplitudes, the northern Adriatic displays the largest tidal ranges in the entire basin. This distinction arises primarily from its unique geographical and morphological features: a shallow basin, with large continental shelf, and semi-enclosed configuration. These conditions favor amplification of tidal signals and produce dynamic responses not commonly observed in deeper Mediterranean sub-basins (Guarnieri et al., 2013).

Tidal resonance is a key factor shaping the tidal regime of the northern Adriatic. The natural oscillation periods of the basin are close to the periods of the dominant tidal constituents, leading to resonant amplification of both diurnal and semidiurnal harmonics (Medvedev et al., 2020). Such resonance contributes to elevated tidal amplitudes and the formation of standing wave patterns (seiches), which significantly influence coastal dynamics and flood risk, notably in areas such as the Venetian Lagoon.

In addition to astronomical forcing, meteorological drivers play a strong role in sea-level variability. Local wind systems, including the Bora (from ENE) and Scirocco (from SE), along with rapid atmospheric pressure fluctuations, often interact with the tidal signal to generate extreme water level events (so-called "acqua alta") in Venice, also felt in Trieste and Grado. These superposed effects, tidal, seiche, storm surge, lead to marked variability across temporal scales. Understanding their coupling is critical for hydrodynamic modelling and hazard assessment (Camuffo, 2023; Rus et al., 2023).

The Adriatic Sea is among the regions of the globe with the longest and densest records of sea-level variability, as TG observations in Venice and Trieste have

been maintained since the mid-19th century. This long observational history makes the basin particularly valuable for studies of tidal dynamics and long-term sea-level change.

Although the Mediterranean Sea is connected to the Atlantic Ocean through the Strait of Gibraltar, the strait's narrow geometry allows only a small fraction of the Atlantic tidal energy to enter (Candela et al., 1990). Consequently, tides in the Mediterranean are primarily driven by direct astronomical forcing rather than by Atlantic propagation (Pugh et al., 2014). Given the scale of the basin relative to tidal wavelengths, most of the Mediterranean is microtidal, with average ranges not exceeding 20–30 cm (Tsimplis et al., 1995). Two areas, however, represent clear exceptions: the Gulf of Gabès in Tunisia, where spring tidal ranges reach approximately 2 m amplitude from the mean (Othmani et al., 2017), and the northern Adriatic, where tides may exceed 1 m amplitude during spring conditions (Janeković et al., 2005).

From a geophysical perspective, OTL in the northern Adriatic is also significant. The shallow water depth and broad horizontal extent of the basin induce elastic deformations of the solid Earth that can be detected via geodetic methods, such as GNSS. These deformations are relevant not only for the correction of geodetic observations, but also for the characterization of vertical land motion and subsidence.

Finally, the societal relevance of the region is substantial. The northern Adriatic coastline is densely populated and economically important, with major ports, industrial activity, and culturally significant sites (Venice among the foremost). Episodic flooding events, especially "acqua alta", are directly tied to the interplay among tides, meteorological forcing, resonance, and subsidence. Thus, research into tidal dynamics and loading here advances fundamental physical understanding and addresses critical issues of coastal resilience and adaptation under climate change.

5.1 Sea level height estimation from tide gauge

Models for determining sea level height variations are generally based on TG and satellite altimetry data. We analyzed most of the available TG stations in the north Adriatic area, estimating tidal wave amplitudes and phases over an

extended period, and compare the results with the FES2014b global model.

For each station, the outliers are firstly removed and the time series interpolated. Annual, semi-annual oscillations, and linear trend over the period are subsequently removed to obtain an accurate representation of the ocean tidal effect only. These variations are mainly due to oceanographic, atmospheric, and hydrological processes, such as seasonal heating and cooling of the ocean, seasonal wind forcing and ocean circulation, atmospheric pressure, and river discharge. Data from the Monfalcone station were decimated from 10-minute to hourly resolution by averaging six consecutive 10-minute samples, which acts as a low-pass (anti-aliasing) filter prior to resampling.

The evaluation of tidal amplitudes and phases over one year data at the selected stations was computed using *Utide* Matlab toolbox (Unified Tidal Analysis and Prediction Functions) (Codiga, 2011), considering 68 tidal constituents (Table B.1). Tidal constituents are automatically selected using the Foreman (M. Foreman, 1977) decision-tree criterion, which applies the Rayleigh resolution criterion within the UTide framework. The inverted barometer (IB) effect was not accounted for in the present analysis; therefore, sea-level variations associated with atmospheric pressure forcing are retained in the residual signal.

The results are collected in Figures 5.1 (amplitude in cm) and 5.2 (phase in degree), showing a good agreement with the previous studies conducted for this area (Janeković et al., 2005; Medvedev et al., 2020). There is a clear increase in the relative importance of the semidiurnal constituents, particularly M_2 and S_2 from south to north. Stations in the northernmost Adriatic (Trieste, Monfalcone, Venezia) consistently show stronger M_2 amplitudes, often reaching values comparable to or exceeding the diurnal K_1 component. This spatial trend is consistent with the known resonant response of the Adriatic basin to semidiurnal tidal forcing, which is enhanced in the shallower and narrower northern sub-basin (Medvedev et al., 2020). The amplification of semidiurnal constituents toward the head of the Adriatic has been reported in earlier studies and is linked to the basin's geometric configuration, which favors resonance with the M_2 tide. In addition to the dominant K_1 and M_2 signals, the secondary constituents (O_1, K_2, N_2, J1, Q_1) contribute at smaller but non-negligible levels, typically below 10 cm amplitude. Among these, S_2 plays an important role in reinforcing the semidiurnal variability in the north.

Comparison between observed TG amplitudes and the FES2014b tidal model indicates generally good agreement. The model reproduces the dominance of K_1

and M_2 and captures the northward anticlockwise increase in semidiurnal energy, though with some deviations in amplitude at individual stations. These differences may be related to local bathymetric effects, coastal geometry, or unresolved shallow-water dynamics that are not fully represented in the global model. Nevertheless, the overall correspondence supports the use of FES2014b as a reliable boundary condition for tidal forcing in the Adriatic. The main differences with the model appear in the phase estimation for the tidal constituents in Split and Zadar, where the model possibly fails due to coastal and bathymetry knowledge deficiencies. The dominant constituents M_2 and K_1 are overestimated bt the model respect to the observations.

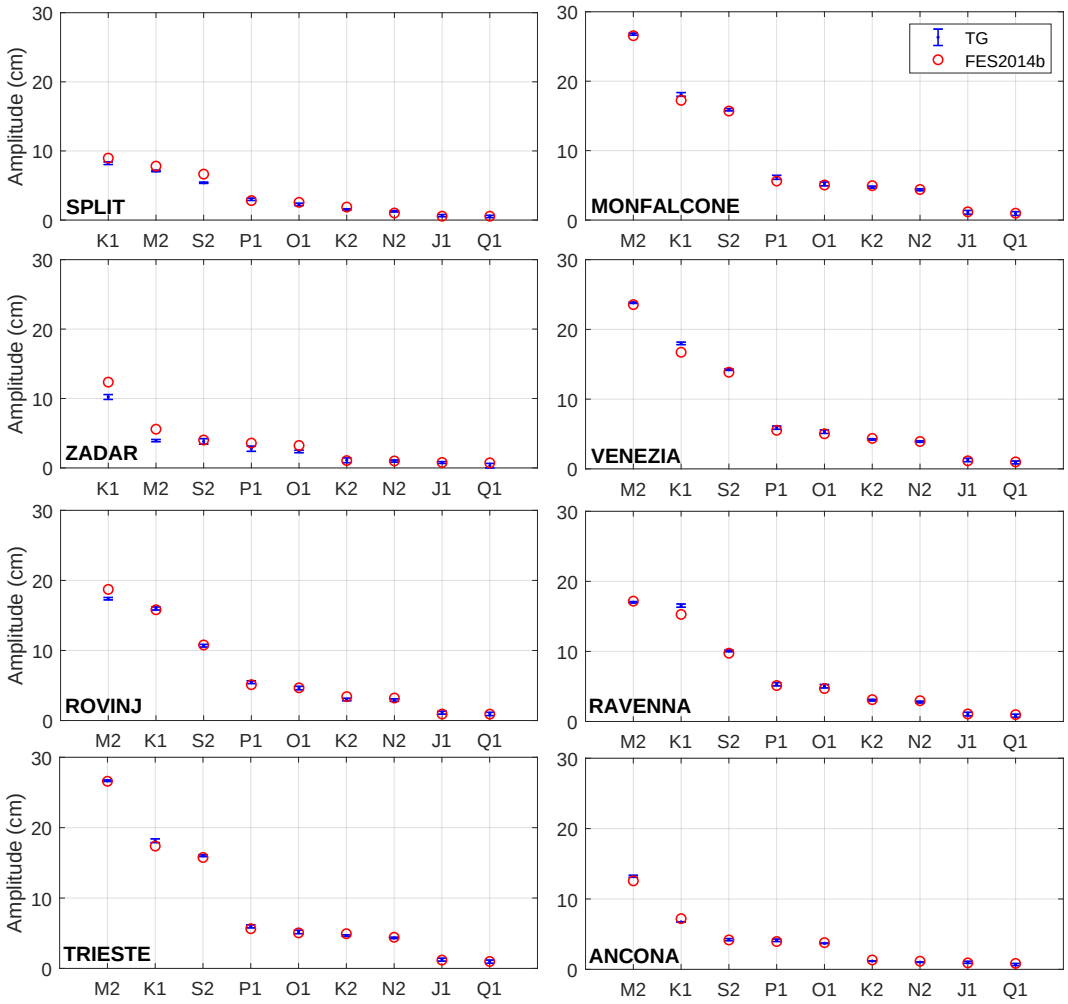

Figure 5.1: Amplitudes of the ocean tidal constituents at different TGs in the northern Adriatic sea. The blue dots with bars represent the estimated amplitudes of the TG data, the red dots are the amplitudes according to the global model FES2014b.

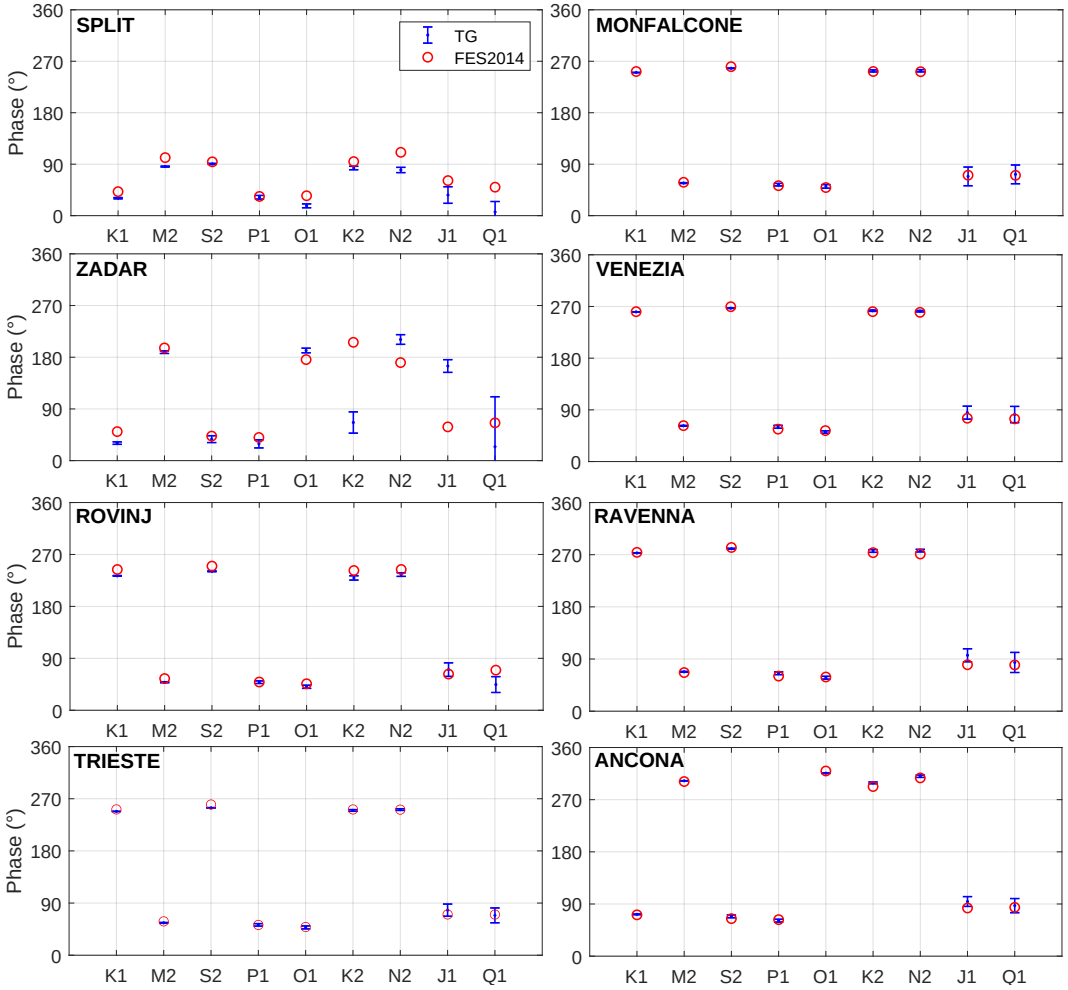

Figure 5.2: Phases of the ocean tidal constituents at different TGs in the northern Adriatic sea. The blue dots with bars represent the estimated phases of the TG data, the red dots are the phases according to the global model FES2014b.

5.2 Sea level height estimation from GNSS reflectometry

The sea level height estimates from GNSS-R for the three stations selected (VEN1, PORE, GARI) along the northern Adriatic coast are presented (Figure 3.2). Following the processing scheme described in Section 3.5, the sea surface height (SSH) was derived from GNSS reflectometry observables and compared with TG measurements available near each site.

The input parameters are listed in Table 5.1. For each station the elevation angle, azimuthal, and reflector height ranges, and satellites capture from the receiver are indicated. These selected inputs aimed to maximize the number of valid observations. For example, GARI station had an unrestricted azimuthal

visibility, which provided a large number of daily observations, while PORE was more constrained due to limited azimuthal coverage.

Table 5.1: Input parameters used for the GNSS-R sea level estimation at the three northern Adriatic stations. The table lists the elevation angle, reflector height, and azimuthal ranges, along with the satellite constellations included in the analysis.

Station	Δe	ΔH_{refl}	**Satellite**	$\Delta azimuth$
VEN1	5-20°	15-20	GRE	150-240°
PORE	5-20°	18-24	GRE	210-270°
GARI	5-20°	3-10	GRE	0-360°

The SSH outputs were smoothed with a 3-hour moving mean to filter out the high-frequency signals and resampled at evenly spaced intervals of 1 hour for comparison with the similarly filtered TG data. Resampling was necessary because satellite transits do not occur at regular time intervals. Both time series were interpolated to compute the cross-correlation and assess their relation. All results are summarized in Table 5.2. The number of sea observation per day depends on the angular visibility of the reflective surface. The results show a strong consistency between GNSS-R and TG data, with correlation values exceeding 90% at all stations. The number of observations per day varied between sites depending on visibility constraints, and the residual noise ranged between 9 and 13 cm. The noise is defined as the standard deviation of residuals between the GNSS and TG sea levels.

Figure 5.3 highlights one month of data for each of the three GNSS sites, compared with the TG time series. Since PORE is not located near any TG, comparisons were made with both Trieste and Venice.

Table 5.2: Summary of GNSS-R sea level results for the analyzed stations. Reported values include the number of daily observations, mean sea surface height, reference TG, correlation coefficient with TG data, and residual noise level.

Station ID	**N° obs**	**Mean H (cm)**	**TG**	**Corr %**	**Noise (cm)**
GARI	108	7.8	Ravenna	91.2	10.1
VEN1	119	16.9	Venice	94.9	9.07
PORE	72	22.1	Trieste	91.6	13.2
			Venice	91.5	12.1

Overall, these results demonstrate that GNSS-R can provide reliable sea level

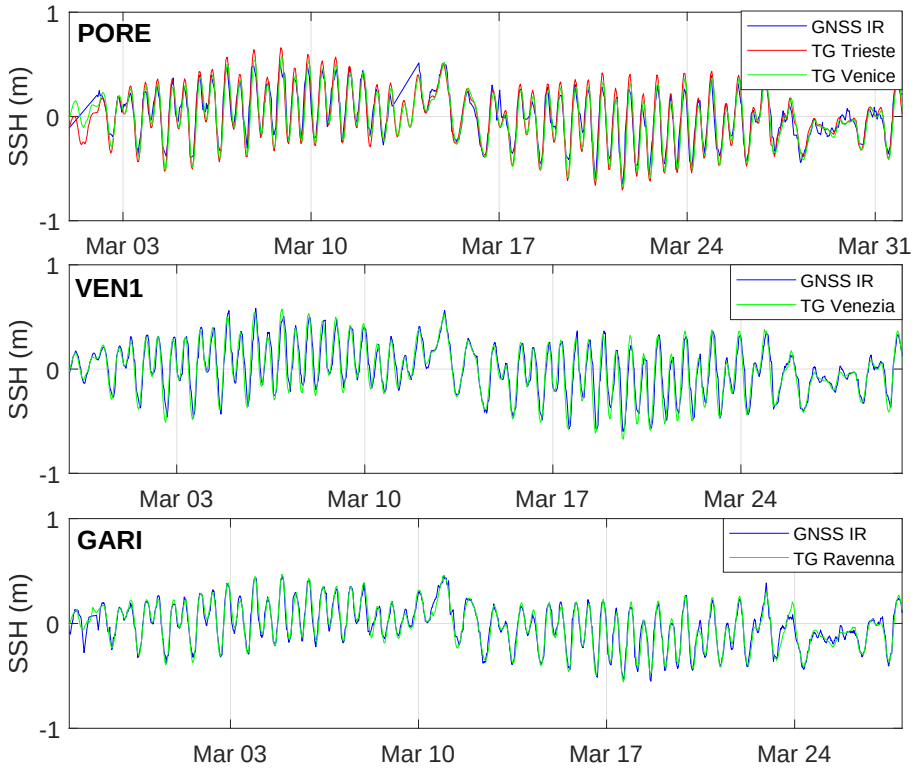

Figure 5.3: Comparison between GNSS-R derived sea surface height (SSH) time series and TG (TG) measurements for the three northern Adriatic stations. The GNSS-R results were smoothed with a 3-hour moving mean and resampled at 1-hour intervals to match the TG data.

measurements along the northern Adriatic coast. The high correlations with TG records highlight its potential as a complementary tool for coastal sea level monitoring, particularly in regions where traditional TGs are sparse or absent.

We analyzed the power spectra of the reflectometry time series and compared them with those derived from the TG data. The results show a clear reduction in amplitude across all components, leading to amplitude differences on the order of 2–3 cm between the two time series. Figure 5.4 shows, for each station, the diurnal and semidiurnal spectral intervals. The major diurnal (K_1, P_1, and O_1) and semidiurnal (M_2, S_2) constituents are clearly identified, with the largest discrepancies between the solutions observed for M_2 and K_1. which generate the mean discrepancy of about 2-3 cm at each station.

5.2.1 Sistiana results

The continuously acquired dataset used for the analysis, which is still being collected, currently covers the period from 24 July to 17 August 2025. The raw

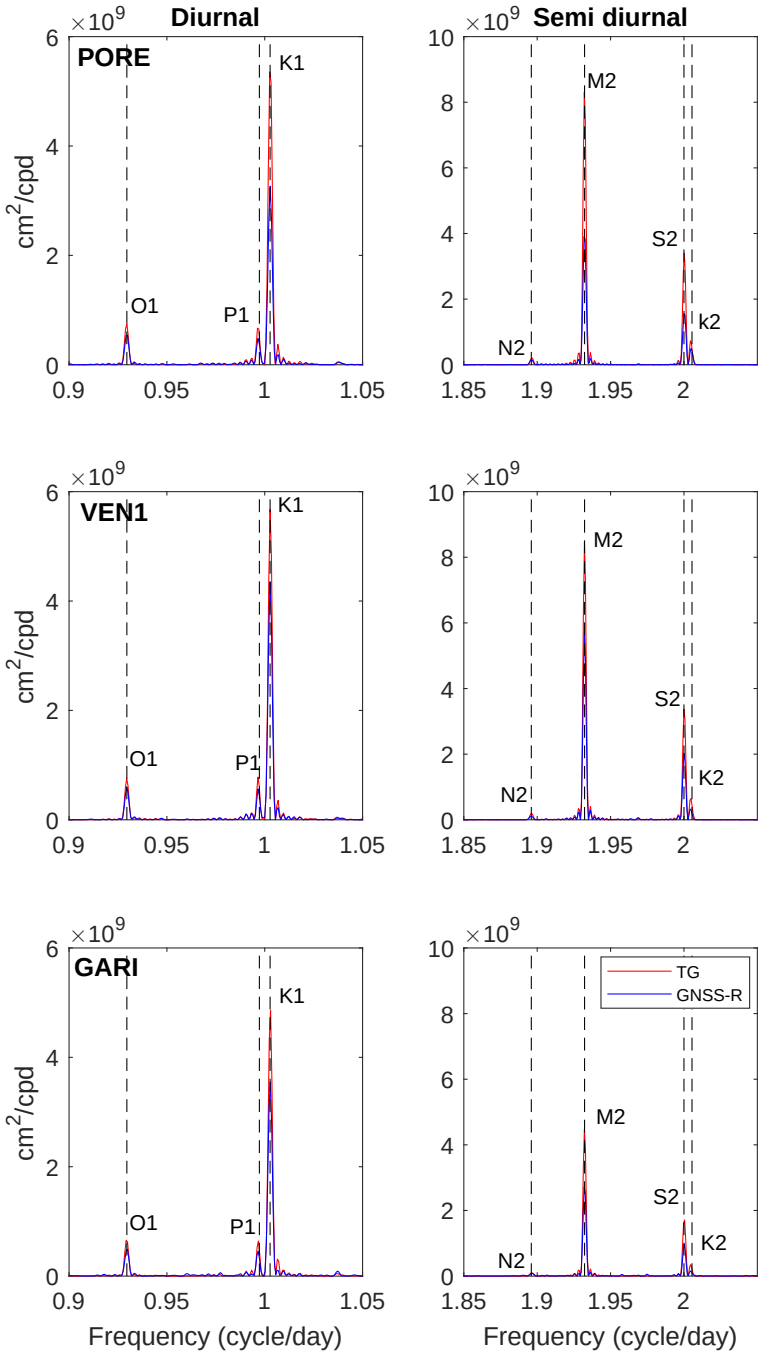

Figure 5.4: Power spectral density of GNSS-R and TG time series for the three stations, showing the principal tidal constituents. The diurnal (K_1, P_1, O_1) and semidiurnal (M_2, S_2) components are clearly visible, with small amplitude discrepancies (2–3 cm) between GNSS-R and TG data.

files were converted from the T00 format to the RINEX format using the Trimble Convert to RINEX utility. This software converts Trimble GPS measurement files stored in DAT or T00 format into RINEX version 2 or 3 files.

Following the processing procedure described in Section 3.5, Figures 5.5, 5.6, and 5.7 present the analysis used to select the elevation angles, reflection zone,

and GPS frequencies.

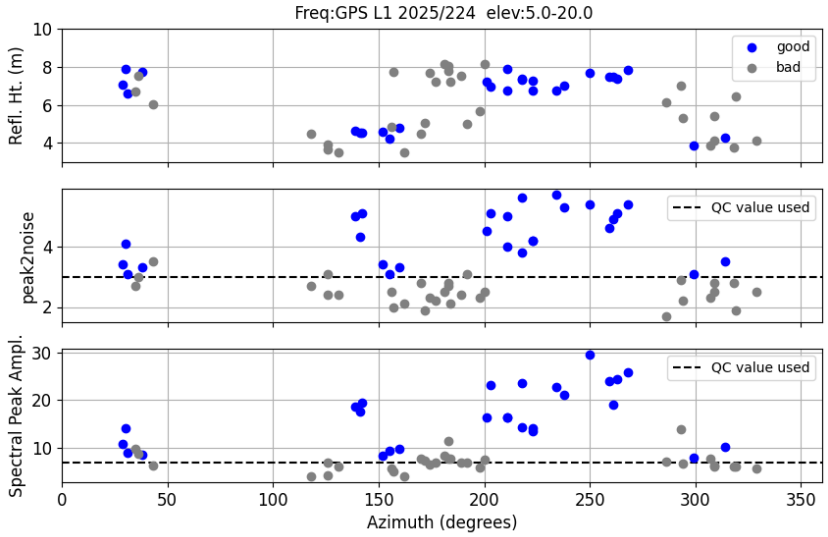

Figure 5.5: Summary plots from the quickLook function for the Sistiana GNSS-R station. The upper panel shows reflector height retrievals as a function of azimuth, the middle panel displays the peak-to-noise ratios, and the lower panel indicates spectral peak amplitudes used for reflector validation.

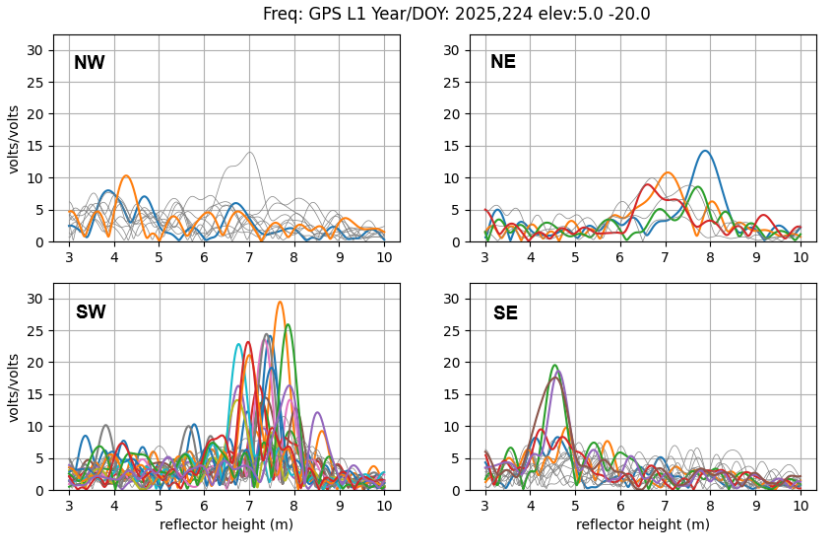

Figure 5.6: Periodograms of SNR observations for Sistiana station. The spectral peaks confirm the presence of a stable reflector approximately 7 m below the antenna, corresponding to sea surface reflections in the southwest azimuthal sector (180°–270°).

Considering elevation angles between 5° and 20°, a reflective surface located approximately 7 m below the GPS antenna is evident. Figure 5.5 shows, in its first panel, the reflector heights that are identified as valid points for sea surface

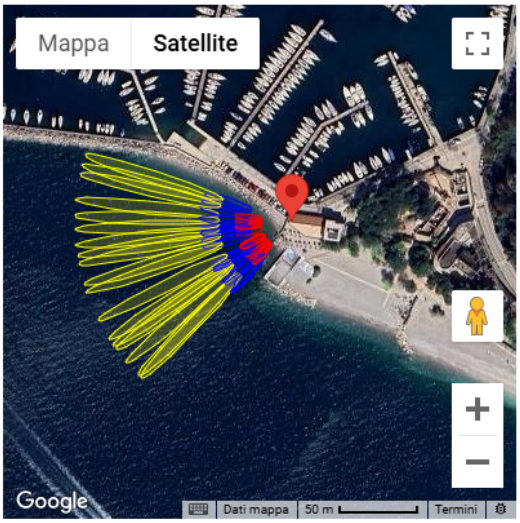

Figure 5.7: Reflection zone for the Sistiana GNSS-R station. The colored clusters represent the reflection areas corresponding to different satellite elevation angles, highlighting the azimuthal sector (200°–280°) associated with valid sea surface reflections. The ellipses refer to the elevation angle, with the following color coding: yellow for 5°, blue for 10°, and red for 15°, depending on the direction of arrival of the reflected signal.

height determination, expressed as a function of azimuth angle. Cross-checking with Figure 5.7 indicates that reflections originating from the sea surface correspond to the azimuthal sector between 200° and 280°. The ellipses refer to the elevation angle, with the following color coding: yellow for 5°, blue for 10°, and red for 15°, depending on the direction of arrival of the reflected signal. Conversely, the apparent good points detected by the software in the range of 30°–150° are excluded from the processing strategy, as they are not reliable for estimation and are unrelated to sea surface reflections. Finally, Figure 5.6 confirms the presence of a reflector at approximately 7 m beneath the antenna, located in the south-western azimuthal quadrant (180°–270°). The input information for the processing strategy are summarized in Table 5.3.

The first part of the data processing is dedicated to the detection of outliers, based on the three sigma outlier criteria. For Sistiana station (see Figure 5.8), no outliers were detected, so all the 688 observations for the 24 days were used to estimate the RH. Figure 5.9 shows the number of RH observations for each day of the measurements, with an average of 27.7 observations per day. As known, by using only GPS satellites, due to the limitation of the receiver, the daily observation are not maximized, still remaining sufficient for an accurate sea level estimation, as presented in Figure 5.10.

Table 5.3: Input configuration adopted for the Sistiana GNSS-R processing, including elevation angle, reflector height range, frequency list, and azimuth limits used for reflector height estimation.

Parameter	**Input**
Elevation angle range	5° to 20°
Assumed $\Delta H_{reflector}$	1 to 8 meters
Peak to noise	3
Frequency list	1, 2, 5, 20
Azimuth range	200° to 270°

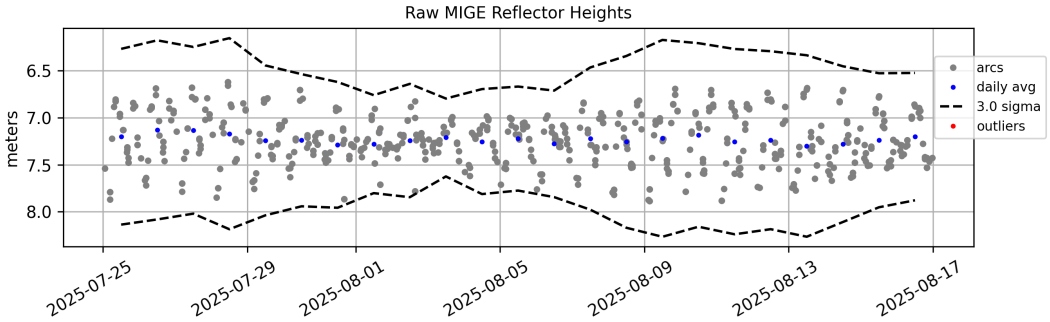

Figure 5.8: Raw reflector height retrievals for the Sistiana station. No outliers were detected under the three-sigma criterion, and all 688 observations were retained for subsequent analysis.

The estimated reflector height obtained with the GNSS-R technique was

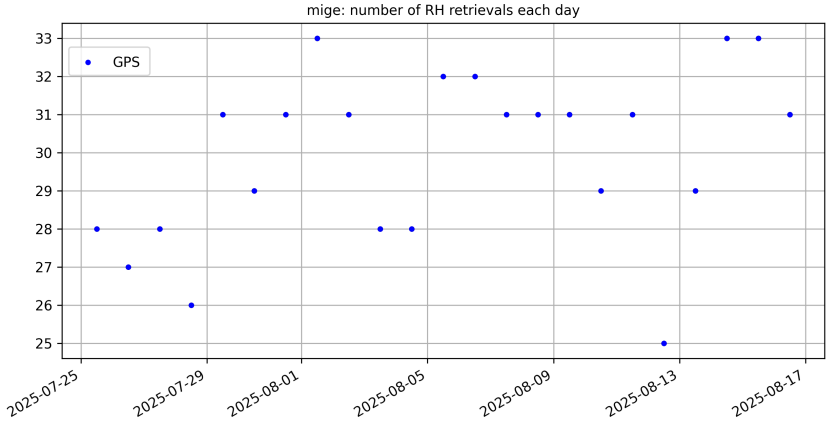

Figure 5.9: Number of valid GNSS-R RH observations per day at the Sistiana station. An average of 27.7 daily observations was obtained using only GPS satellites.

subsequently compared with two TGs present in the Gulf of Trieste, located at Trieste and Monfalcone (see Figure 5.11). The TG series were collected from the

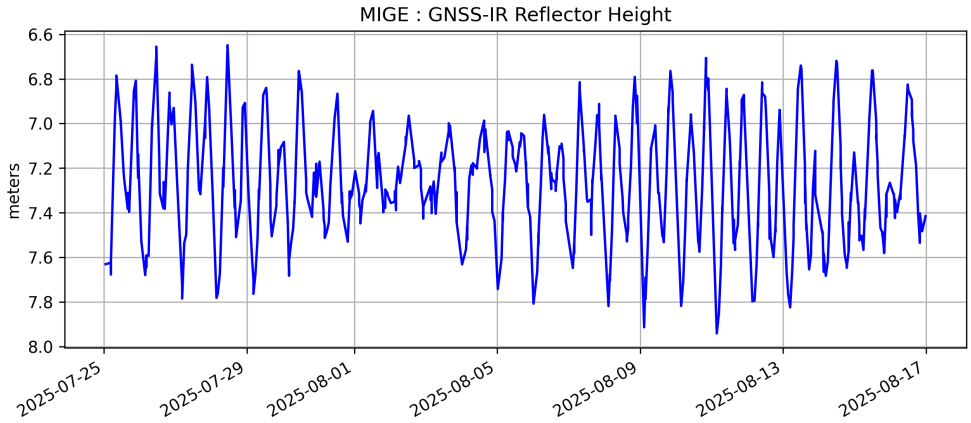

Figure 5.10: Time series of reflector height estimated from GNSS-R at Sistiana. The retrieved sea level variations show a stable reflector at 7.2 m below the antenna.

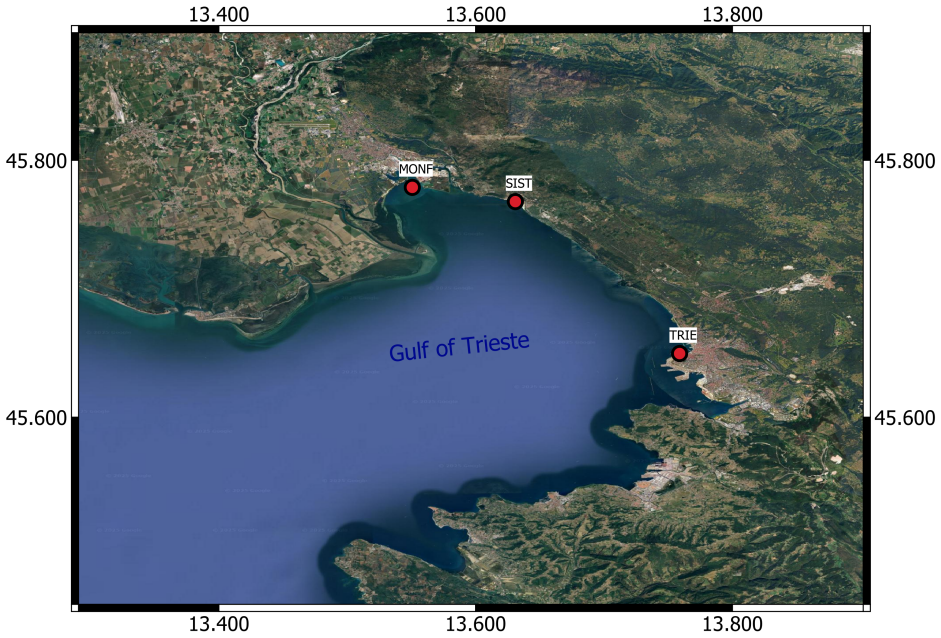

Figure 5.11: Location of the Trieste and Monfalcone TGs, respect to the Sistiana GNSS-R station.

ISPRA database, and, as well as the GNSS-R estimations, they were smoothed through a moving average filter using a 3-hours sliding window in order to filter out the high-frequency signal. The comparison is shown in Figure 5.12, where the blue curve represents the sea level variation estimated with the reflectometry technique, and the red and green curves are the TG data for Trieste and Monfalcone respectively. By computing a normalized cross-correlation on the ob-

servations, the results show a correlation of 95% between Sistiana and Trieste, and a correlation percentage of 94% between Sistiana and Monfalcone. Comparing the tidal amplitudes, a difference of 2-3 cm is visible between Sistiana and Trieste, and 4-5 cm with Monfalcone.

The analysis performed at the Sistiana GNSS station demonstrates the feasibility and reliability of using reflectometry for sea level monitoring in the Gulf of Trieste. The adopted processing strategy enabled the identification of a stable reflector height 7.2 m below the antenna, corresponding to the average sea surface.

Despite the receiver's limitations, which results in fewer daily observations compared to a multi-constellation GNSS station, the data proved sufficient to retrieve sea level estimates consistent with close located TGs. Another potential limitation arises from the restricted azimuthal range of the site; the visible sea portion covers only about 80°, which is below the minimal 90° recommended for RH estimation. Nevertheless, although this reduces the number of daily observations, the derived estimates remain robust and satisfactory.

These results confirm that GNSS-R is a reliable and complementary tech-

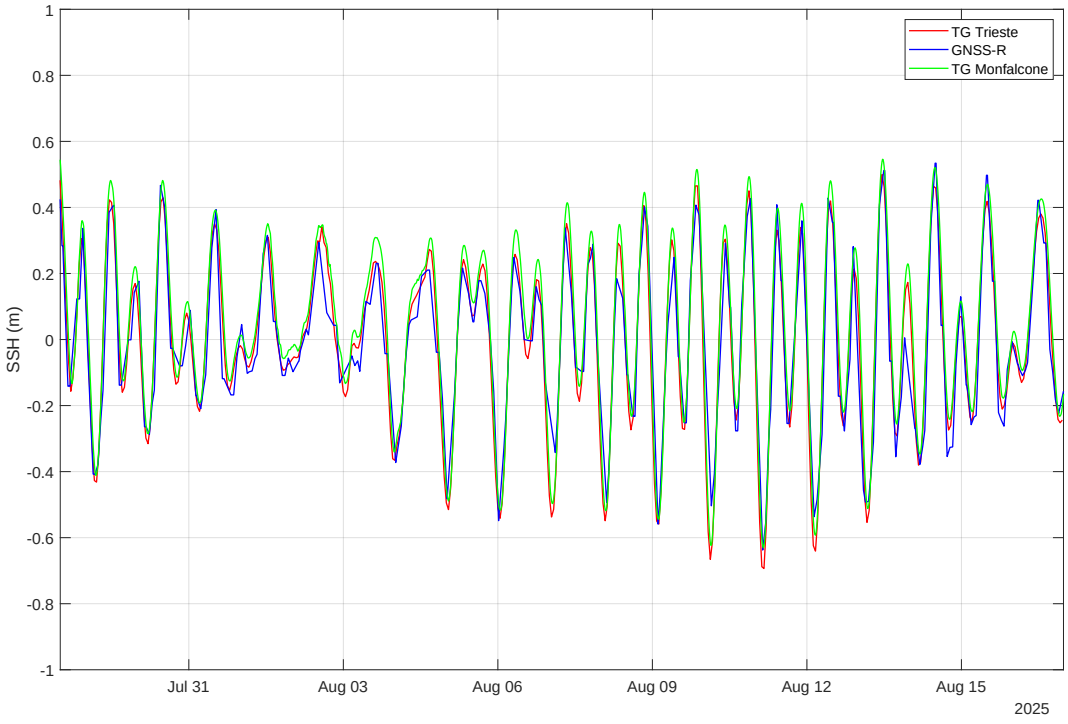

Figure 5.12: Comparison of 3-hour moving mean sea level variations for Sistiana (GNSS-R) and nearby TGs at Monfalcone and Trieste. The consistent temporal evolution confirms the high correlation between GNSS-R and TG measurements.

nique to traditional TG measurements for sea level monitoring, with strong po-

tential to expand observational coverage in coastal areas. The high correlation with established instruments highlights the robustness of the method, even when relying solely on GPS signals and under sub-optimal site conditions. GNSS-R thus represents a cost effective alternative to TGs, and a practical solution for sea level estimation in locations where installing a conventional TG station is challenging or unfeasible.

5.3 GNSS ocean tidal loading analysis in the northern Adriatic region

Among the processing techniques, the PPP was chosen to extract the absolute effect in terms of loading of the ocean tides in the northern Adriatic area. This choice is justified because the loading effect is relatively small (in the order of 10 mm maximum) and must be accurately separated from the noise present in the GNSS time series.

The database is described in Section 3.1.2, processed with a sampling period of 1 hour for 1 year length. We focus on the detection and estimation of OTL amplitudes and phases at each site, comparing the observations with the most used global ocean tidal model FES2014b.

5.3.1 3-D surface deformation calculation

For this study, we calculate the 3-D surface displacements caused by OTL using the *LoadDef* software (Martens et al., 2019). *LoadDef* is a Python-based toolkit developed to simulate the spheroidal deformation response of a spherically symmetric, isotropic, elastic, and non-rotating (SNREI) Earth subject to external forces such as surface mass loading and gravitational fields.

It starts by computing the load Love numbers integrating the equation of motion for spheroidal deformation through the interior layers of the Earth (Alterman et al., 1959, Farrell, 1972). Subsequently, the Love numbers are combined in spherical harmonic expansions to compute Green Functions (GFs) for the 3-D surface deformation (see Chapter 2.3).

To provide a clearer visualization of regional displacements, the horizontal deformation can be represented as particle motion ellipses. This approach was applied to identify the dominant components in the northern Adriatic region,

selecting for further analysis only those OTL constituents that exhibit a vertical amplitude major or close to 1 mm. Figures 5.13 and 5.14 illustrate the modelled OTL amplitudes for the eight principal tidal constituents: the semidiurnal (M_2, S_2, N_2, K_2) and diurnal (K_1, O_1, P_1, Q_1) components.

The size, shape, and orientation of the ellipses represent the horizontal displacement, while the colors indicate the vertical displacement. Based on this assessment, only the M_2, S_2, N_2, K_1, O_1 and P_1 components were retained for analysis, as the remaining constituents exhibit amplitudes far below the GNSS noise level and could therefore be subject to miscalculation. Furthermore, since the processing strategy does not include any atmospheric model, we decided to exclude the S_2 constituent from the estimation, as its amplitude could be biased by atmospheric solar effects.

5.3.2 Tropospheric delay estimation

Sub-daily variability in ZTD is dominated by atmospheric thermal tides at one and two cycles per solar day (S_1 and S_2), generated by the diurnal cycle of heating, humidity and surface pressure. These effects are a persistent, millimeter-level feature of ZTD observed with GNSS and coherently related to local meteorology. In GNSS solution, ZTD and the vertical coordinate are intrinsically coupled by the tropospheric mapping function, so if S_1/S_2 are not represented in ZTD, part of their energy can be spuriously absorbed by the Up component. Early analyses quantified this leakage and showed how height errors map into ZTD and vice-versa (Vey et al., 2002). At the same time, the OTL signal is best recovered from the coordinate time series themselves. To avoid absorption of tidal effects in the tropospheric delay estimates, the delays are modeled stochastically and estimated together with the station coordinates, using nominal values as a reference at high temporal resolution (Martens et al., 2016). The tropospheric signal delays are derived from a combination of numerical weather model outputs and stochastic estimation. Nominal values for the zenith wet and dry delays are obtained from the Vienna Mapping Function 3 (VMF3, Landskron et al., 2018) grids, which are based on six-hourly numerical weather model data provided by the European Centre for Medium-Range Weather Forecasts (ECMWF; Boehm et al., 2006).

We first conducted an analysis of the sampling intervals used for ZTD estimation by comparing the RMS of the position time series at different intervals. This investigation was motivated by the strong correlation between station coordinates

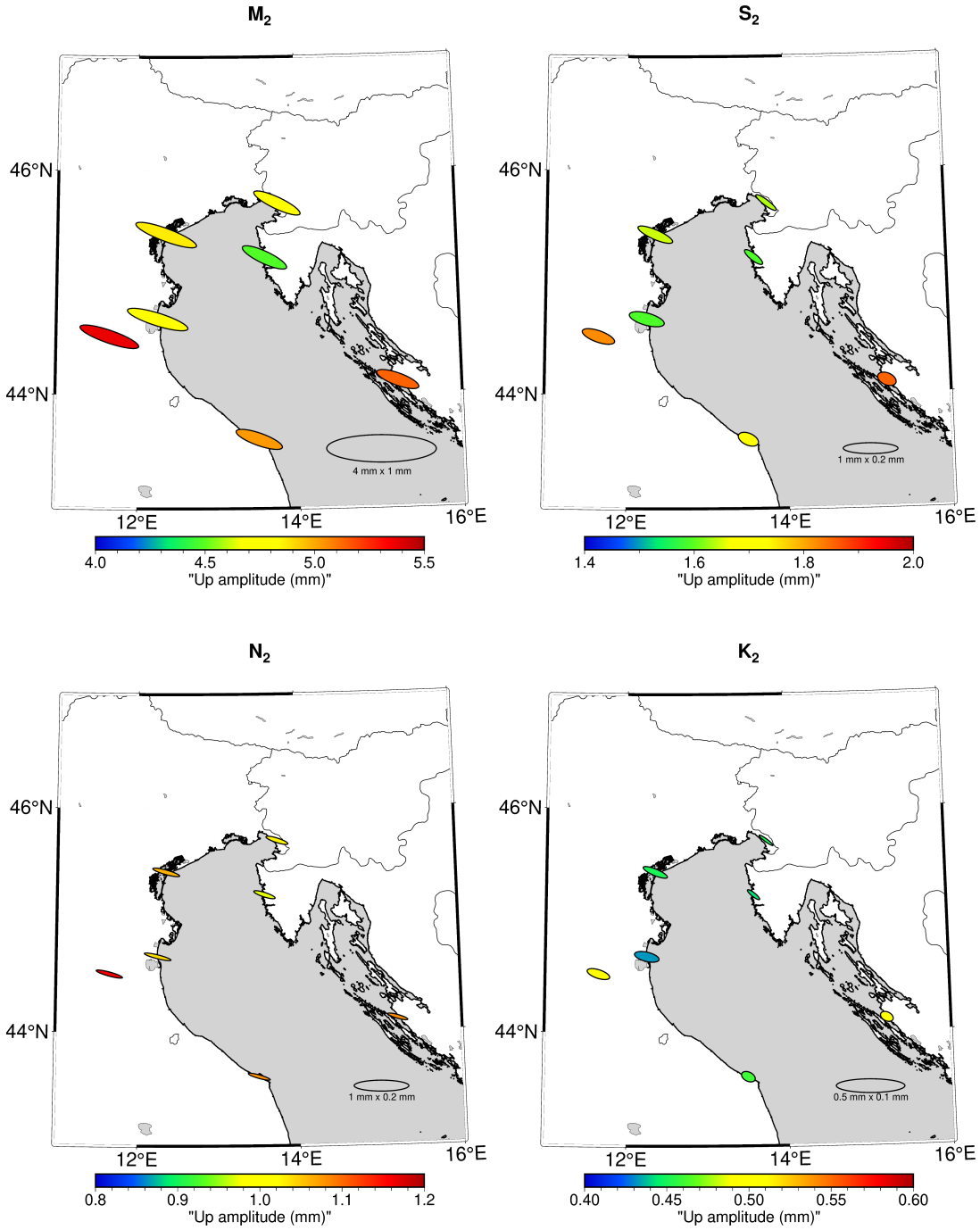

Figure 5.13: Predicted semi-diurnal components surface displacements from FES2014b model at each selected station. Size, shape, and orientation of the ellipses denote horizontal displacement and the colors depict the vertical displacement. Reference ellipsoids and color scale are different and shown for each tidal constituent; consider that the horizontal scales vary from figure to figure.

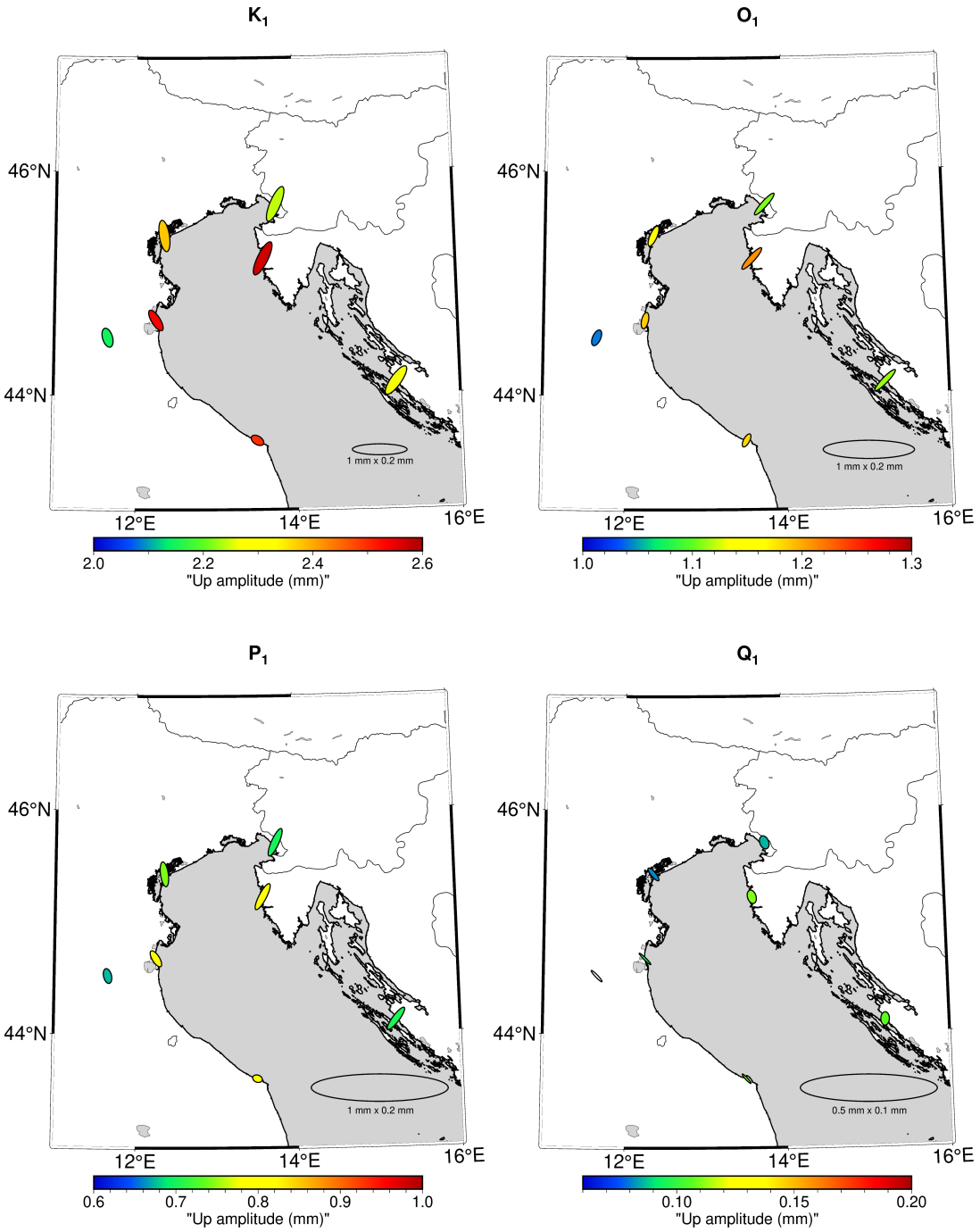

Figure 5.14: Predicted diurnal components surface displacements from FES2014b model at each selected station. Sized, shapes, and orientations of the ellipses denote horizontal displacement and the colors depict the vertical displacement. Reference ellipsoids and color scale are different and shown for each tidal constituent; consider that the horizontal scales vary from figure to figure.

and ZTD estimates, as well as by the objective of minimizing displacement noise to optimize the detection of small tidal components. Three cases were examined: (i) a 1-hour sampling interval without horizontal gradient estimation in the tropospheric wet delay; (ii) a 1-hour sampling interval with horizontal gradient estimation; and (iii) a 10-minute sampling interval without horizontal gradient estimation.

The positioning performance of station VEN1 under different tropospheric delay estimation strategies is presented in Figure 5.15. The results highlight the

Figure 5.15: RMS comparison of coordinate time series at station VEN1 for different ZTD estimation strategies. Three cases are shown: 1-hour ZTD interval without gradient estimation (red), 1-hour interval with horizontal gradient estimation (blue), and 10-minute interval without gradient estimation (green). The results indicate that shorter ZTD intervals and gradient modeling produce only marginal improvements in coordinate precision.

clear discrepancy between vertical and horizontal components in terms of sensitivity to the zenith tropospheric delay (ZTD) estimation interval and the inclusion of gradient parameters. For the Up component, the RMS ranges from 15.39 mm to 15.77 mm, indicating only a marginal difference between solutions with 1 hour or 10 minutes ZTD intervals and the inclusion or omission of gradient parameters. In the East component, RMS values vary between 9.18 mm and 10.85 mm, show-

ing a slightly larger spread but still with no substantial improvement from more frequent ZTD updates or gradient modeling. The North component is the most stable, with nearly identical RMS values (5.77–5.82 mm) across all strategies.

Overall, these results suggest that shortening the ZTD estimation interval and adding gradient parameters do not significantly reduce the RMS in any coordinate component. The variations in RMS remain within the millimeter level, confirming that the tested tropospheric modeling strategies have a limited influence on the final solution. Based on the results, for the processing strategy we chose to estimate the ZTD every 1 hour, including a horizontal gradient estimation every 6 hours, as suggested from the Bernese manual, modelling with the Chen-Herring model (Chen et al., 1997).

5.3.3 Sensitivity test for OTL prediction

We first conduct a sensitivity test to understand the capability of GNSS PPP solutions to resolve the main OTL components given the noise level in such specific environment. To investigate the effect of observational noise on tidal parameter estimation, a Monte Carlo simulation is performed (Mooney, 1997). Synthetic noise, scaled relative to the standard deviation of the original GNSS displacement series, is added to the observations in multiple realizations. To simulate measurement uncertainty in the GNSS synthetic time series, zero-mean Gaussian (normal) noise was added to the displacement data. The noise amplitude was defined as a multiple of the standard deviation of the original signal, allowing control over the noise level through a scaling factor. For each noise level and realization, tidal amplitudes and their uncertainties (standard error *se*) are re-estimated. The resulting ensemble of simulations allows for the characterization of the mean amplitude and the signal-to-noise ratio (expressed as amplitude over standard error of the amplitude) as a function of noise magnitude. The standard error is derived from the covariance of the fitted coefficients obtained through least squares estimation. It reflects how precisely the amplitude has been determined from the available data (M. G. G. Foreman et al., 2009). This procedure provides quantitative insight into the robustness of GNSS-based OTL estimation under varying observational conditions.

Finally, the methodology allows comparison between the observed tidal response and theoretical OTL models, facilitating the evaluation of station-specific

sensitivities and potential systematic biases. By systematically increasing the noise amplitude, the method also identifies thresholds beyond which tidal signals become indistinguishable from random variability, providing guidance for data quality requirements in GNSS estimates.

The synthetic data are generated to cover a full year with an hourly sampling rate, ensuring comprehensive temporal coverage of all major tidal constituents. The noise tests are designed to explore the range from the natural GNSS observation noise up to twice its amplitude, providing an upper bound for sensitivity analysis. For each noise level, 30 independent realizations are performed to ensure statistical robustness of the estimated parameters. To evaluate the statistical significance of each tidal constituent, a t-test was applied to the amplitudes estimated from the harmonic analysis. The t-test quantifies how confidently an estimated amplitude differs from zero, thereby determining whether the corresponding tidal signal is genuinely present in the GNSS displacement series or simply a result of random noise. It is computed as the ratio between the estimated amplitude and its formal standard deviation, the latter being derived from the residual variance of the least-squares harmonic fit. The t-test values are inherently influenced by the noise level of the time series: higher noise leads to larger uncertainties and consequently smaller t-values. Therefore, the statistical significance of each tidal constituent reflects not only its amplitude but also the signal-to-noise ratio of the GNSS vertical displacement series (M. G. G. Foreman et al., 1989). In this study, a threshold of $|t| \geq 2.57$, corresponding approximately to the 99% confidence level, was adopted as the minimum acceptable criterion for statistical significance. The statistical significance of the estimated tidal amplitudes was evaluated using the Student's t-distribution. The critical t-value (t_{crit}) was computed considering the number of degrees of freedom (dof), defined as the difference between the total number of observations (N) and the number of parameters estimated by the harmonic model ($m = 2k$, where k is the number of tidal constituents, each described by sine and cosine terms). The 99% confidence threshold represents the minimum ratio between the estimated amplitude and its standard error required for the constituent to be considered statistically significant.

Figure 5.16 presents the outcome of the sensitivity analysis conducted on synthetic GNSS displacement time series for the main diurnal and semidiurnal tidal constituents (M_2, K_2, S_2, N_2, K_1, Q_1, P_1, and O_1). Each subplot presents the variation of the amplitude-to-standard-error ratio (A/se, left y-axis) and the es-

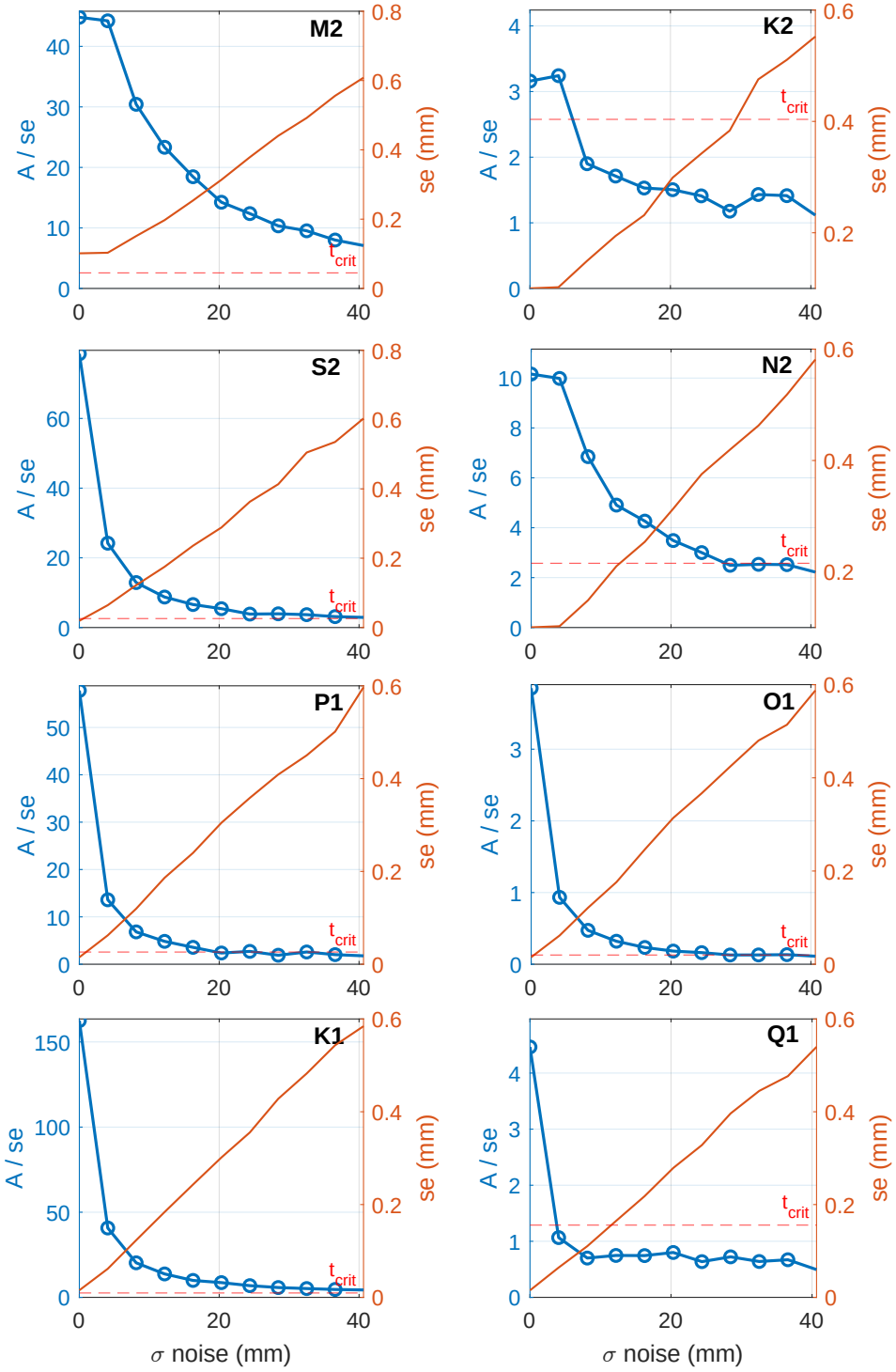

Figure 5.16: Results of the Monte Carlo sensitivity test using synthetic GNSS displacement time series. Each subplot shows the amplitude-to-standard-error ratio (A/se, left axis) and the standard error (se, right axis) as functions of the imposed noise level. The red dashed line marks the 99% confidence threshold. The M_2, S_2, N_2, and K_1 constituents remain statistically significant under realistic noise conditions, whereas weaker components (K_2, Q_1, P_1, O_1) fall below detectability as noise increases.

timated amplitude standard error (se, right y-axis) as functions of the imposed noise amplitude. The horizontal red dashed line indicates the critical value of the Student's t-distribution at the 99% confidence level, used to assess the statistical significance of the estimated tidal amplitudes. The critical t is set to 2.57 and depends on the number of observations (8760) and the number of the estimated parameters in the harmonic analysis (8).

The results reveal a clear and distinct behavior for each tidal constituent. The dominant semidiurnal component M_2 maintains a high A/se ratio (> 20) even at large noise amplitudes, confirming its strong detectability and robustness against measurement noise. S_2 remains statistically significant across most of the tested range, with only a moderate decrease in detectability at higher noise levels. N_2 shows a more pronounced decline in A/se, falling below the confidence threshold at noise amplitudes above approximately 25 mm, indicating reduced reliability for this weaker semidiurnal constituent. K_2, which is the weakest among the semidiurnal components in the region, falls below the critical threshold already for noise amplitudes above 5 mm, indicating that this constituent cannot be confidently resolved under typical GNSS noise conditions.

Among the diurnal constituents, K_1 demonstrates a strong and consistent signal, with A/se values remaining above the threshold across the entire noise range tested. This confirms that K_1 is one of the most reliably detected diurnal tides in the region. In contrast, P_1 and O_1 display lower A/se ratios, falling below the detection threshold even for relatively modest noise levels (20 mm). Q_1 behavior follows the K_2 one, becoming unresolvable for noise above 5 mm. These weaker diurnal components are therefore the most sensitive to noise contamination and would require either improved GNSS precision or longer observation periods (multi-years) for robust estimation.

The right axes of the plots show that the standard error of each constituent amplitude increases almost linearly with the imposed noise level, as expected from least-squares estimation theory. This confirms that the uncertainty in tidal amplitude retrieval scales proportionally with measurement noise.

When comparing these synthetic results with the real GNSS noise level observed at station VEN1 ($\sim$ 15.5 mm), the analysis indicates that the M_2, S_2, N_2, K_1, P_1, and O_1 constituents remain clearly detectable and statistically significant in the actual data. Their ratios to the se at this noise level are still above the critical t-value, suggesting that the station's precision is sufficient to resolve the dominant OTL components. Conversely, the weaker constituents Q_1

and K_2 likely fall below the detection threshold under the same noise conditions, explaining the reduced or absent signatures of these components in real GNSS tidal spectra. This comparison confirms that the observed performance at VEN1 aligns with the expectations derived from the synthetic sensitivity analysis, reinforcing the reliability of the modeling approach and providing a quantitative reference for the minimum data quality required for accurate OTL estimation.

5.3.4 Observed and predicted ocean tidal loading

In this section, the GNSS-derived OTL amplitudes and phases are compared with the global FES2014b model to assess the ability of GNSS to detect and resolve main OTL constituents in the northern Adriatic area and model's ability to reproduce the observed tidal signals. This comparison allows identifying possible regional discrepancies and evaluating the performance of the model in coastal and shallow-water environments.

Figure 5.17 shows, as an example, the power spectral density (PSD) of the vertical displacement for the VEN1 station. Peaks corresponding to the main

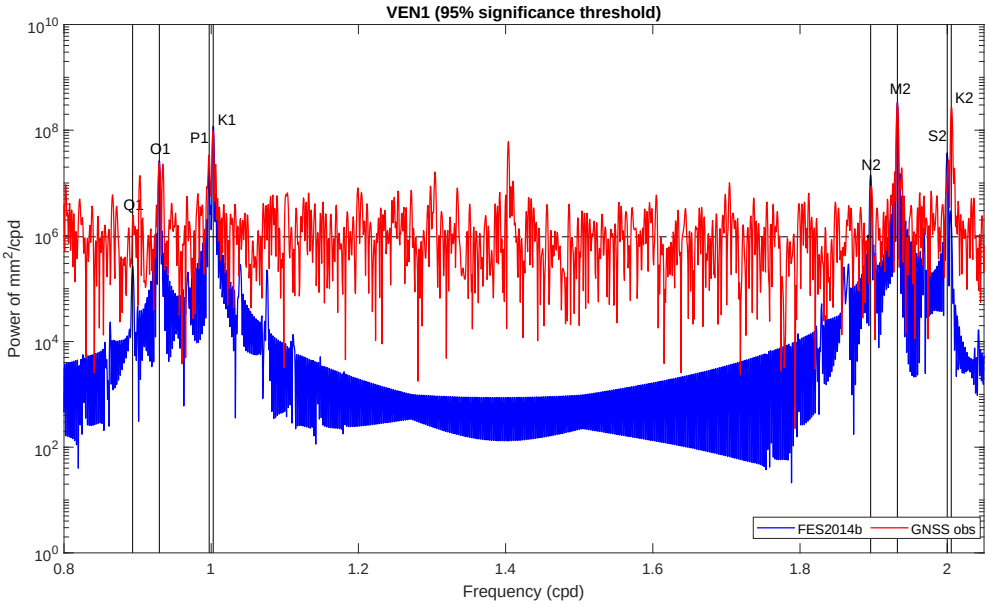

Figure 5.17: Power spectral density (PSD) of the vertical GNSS displacement at station VEN1 compared with FES2014b model predictions. The main tidal constituents (M_2, S_2, N_2, O_1, K_1, and P_1) are clearly visible and consistent with model frequencies, while the minor components K_2 and Q_1 remain below the 5% significance level.

tidal constituents (M_2, S_2, N_2, O_1, K_1, and P_1) are clearly identifiable, with the GNSS-observed peaks closely matching those predicted by the FES2014b model.

The O_1 and K_2 constituents remain below the 5% significance threshold, likely due to their very small amplitudes compared to the noise level present in the time series.

The results for each constituent are shown over the entire dataset; amplitudes and phases of the selected ocean tide (OT) constituent are estimated and compared to the global ocean model FES2014b. The versatile tidal analysis software has been used as described in previous section 4.3.2.

Figure 5.18 presents the t-test values obtained for the main diurnal and semidiurnal tidal constituents (Q_1, O_1, K_1, P_1, N_2 and M_2) at the seven analyzed GNSS stations. For each site, the t-test values are shown separately for the Up (blue), East (red), and North (green) components of the position time series, allowing the assessment of tidal significance in both vertical and horizontal directions. The dashed red horizontal line marks the 99% confidence threshold ($|t| = 2.57$), adopted as the minimum acceptable value for statistical significance. Bars exceeding this threshold correspond to constituents that can be considered statistically significant, meaning that their amplitudes are reliably distinguishable from background noise in the GNSS observations. Across the network, the Up component generally exhibits the highest t-values, reflecting its stronger tidal sensitivity compared with the horizontal components. In most stations, the semidiurnal constituent M_2 yields the largest t-values, often exceeding A/se ratio of 20–30, indicating robust detection of the principal lunar semidiurnal tide. The diurnal constituents K_1 and O_1 also show consistently significant values ($t > 5$) at nearly all stations, confirming their presence in the vertical displacement signal. Conversely, the minor lunar diurnal constituent Q_1 and the inferred solar constituent P_1 usually remain close or below the significance threshold, suggesting that their amplitudes are small relative to the noise level of the GNSS series.

O_1 is significant only in the vertical component, except for the continental station MEDI; in the East and North components, it remains close to or just above the threshold confidence value, reflecting the lower tidal response in horizontal motion.

The minor lunar diurnal constituent Q_1 was also estimated, given its small amplitude and low t-value (< 2.57), it is statistically insignificant and likely masked by observational noise. This is consistent with expectations, as Q_1 typically contributes only marginally to the vertical tidal displacement compared to the dominant diurnal constituents O_1 and K_1.

PORE is the coastal station that exhibits the lowest t-test values, as it is the

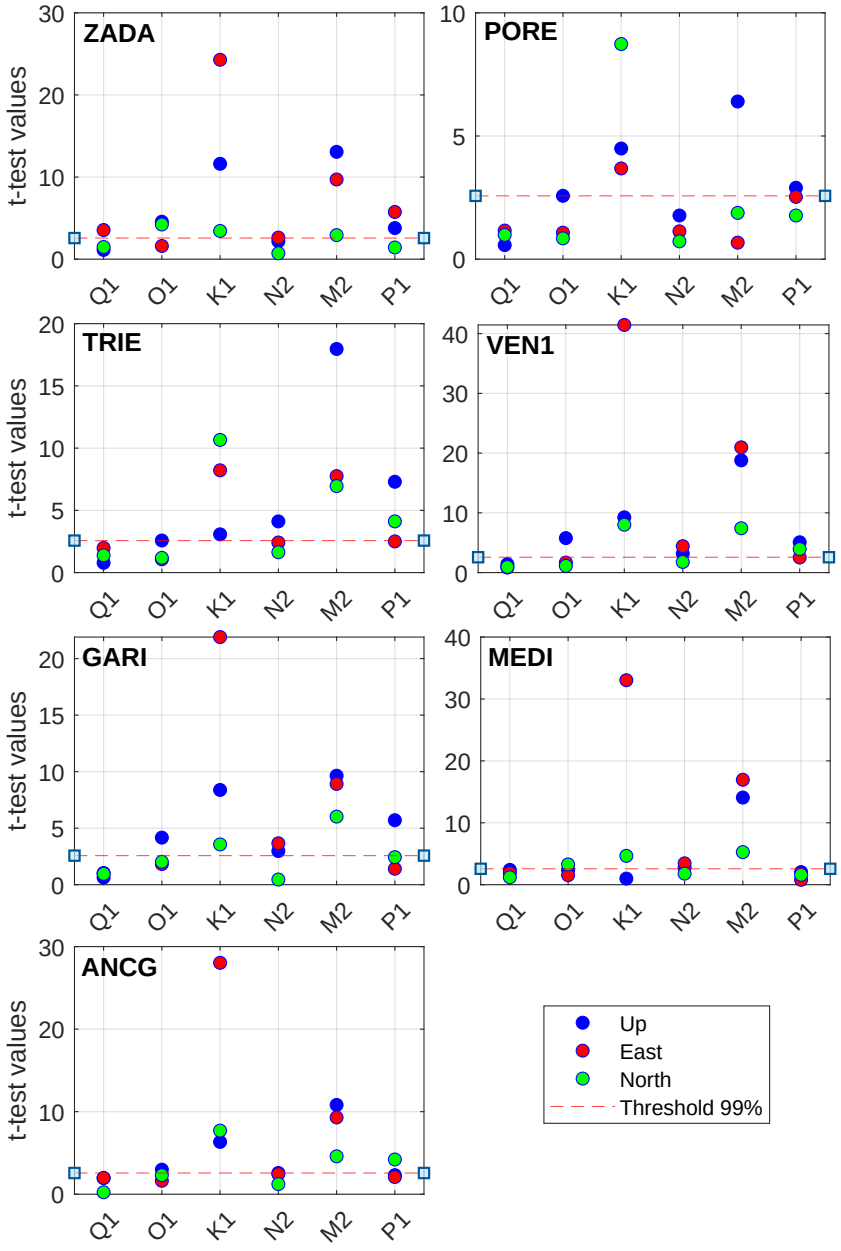

Figure 5.18: Student's t-test results for the main diurnal and semidiurnal tidal constituents (Q_1, O_1, K_1, P_1, N_2, and M_2) at all analyzed GNSS stations. Dots represent the Up (blue), East (red), and North (green) components. The red dashed line marks the 99% confidence threshold; values above this indicate statistically significant tidal detections.

noisiest. In fact, at this station, the only OT components that are significantly distinguishable in the vertical displacement are M_2, K_1, P_1, and O_1. MEDI detects only the strongest components, M_2 and K_1, which can be attributed to its continental location, approximately 50 km inland from the Adriatic coastline.

Overall, the pattern of t-test values confirms that the vertical component of the GNSS displacements is primarily dominated by the principal diurnal and

semidiurnal tidal constituents, whereas the horizontal components contain smaller and less statistically significant tidal signals. This reflects the ability to detect the main OTL components using GNSS even in relatively small basins, particularly in the vertical component, where the weak signal is strogest. However, the detection of smaller or secondary tidal constituents requires longer and less noisy time series, since extended observation periods improve the spectral resolution and reduce the uncertainty of the harmonic estimates.

The phasor diagram in Figure 5.19 shows the complex representation of the main OTL constituents in the northern Adriatic Sea where each vector combines the amplitude and phase of the vertical loading displacement. The red arrows correspond to the estimates derived from the harmonic analysis of GNSS time series, while the black arrows represent the predictions from the FES2014b ocean tide model. This joint visualization enables a direct assessment of the agreement between observations and model predictions, thereby characterizing the basin-scale coherence of the OTL response. The reference system is defined by standard Cartesian coordinate axes, with positive angles measured counterclockwise. Phasors are represented in the complex plane, with the real component along the horizontal axis and the imaginary component along the vertical axis. For each station only the significant components are shown.

The M_2 constituent dominates the tidal loading signal, exhibiting the largest amplitudes and the most consistent phase behavior across the Adriatic basin. The red and black phasors are nearly coincident in both magnitude and orientation, indicating an excellent match between GNSS-derived estimates and model predictions. A slight counterclockwise phase rotation toward the northern shallow shelf suggests a weak delay caused by frictional dissipation and partial standing-wave behavior typical of the semidiurnal tide in a narrow, semi-enclosed basin. The N_2 constituent displays a similar spatial pattern but with smaller amplitudes, about one quarter of those of M_2. Its phasors show very high coherence between estimated and modeled values, confirming that the harmonic analysis captures well the secondary semidiurnal component and that FES2014b accurately represents the semidiurnal loading field over the Adriatic shelf.

The diurnal constituents, by contrast, exhibit noticeably larger discrepancies between the estimated and modeled phasors. The K_1 constituent, in particular, reveals significant mismatches both in amplitude and direction: at several stations, the red vectors deviate from the black ones by tens of degrees and sometimes by more than 30% in magnitude. Such inconsistencies are well-documented in the

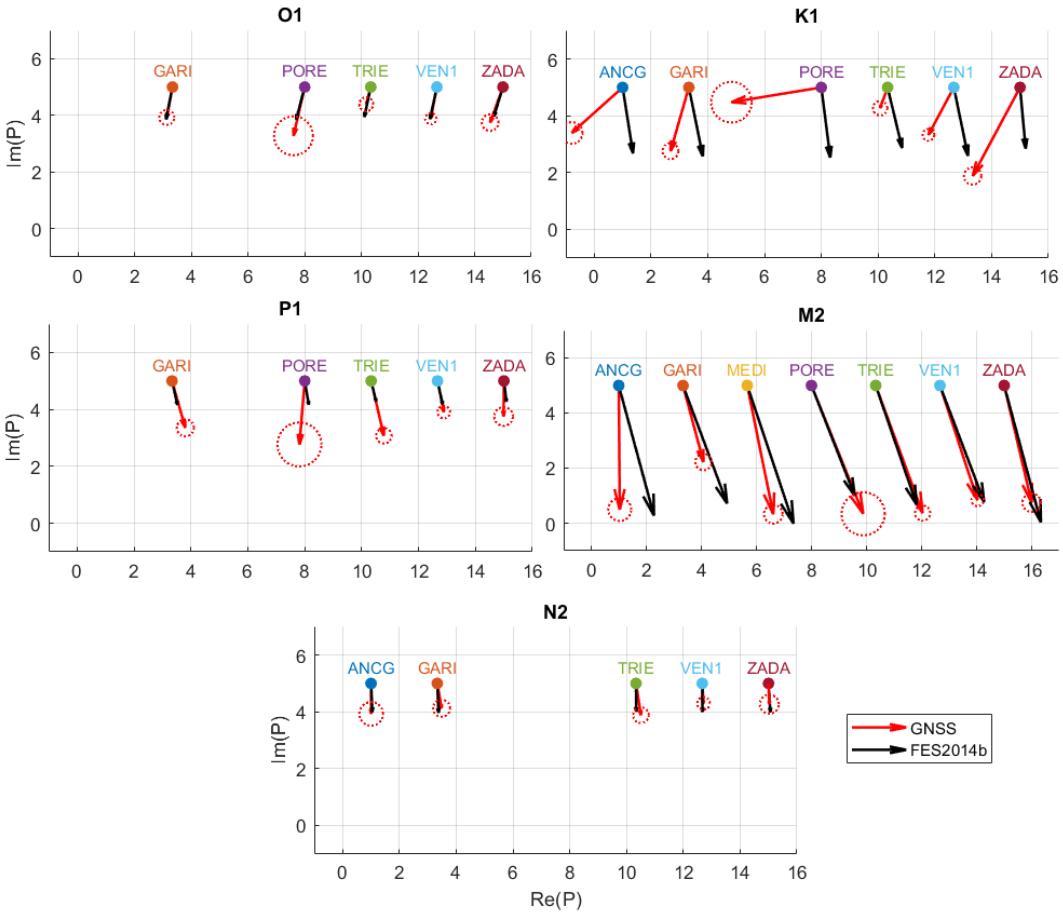

Figure 5.19: Phasor diagram showing the complex representation of the main OTL constituents in the northern Adriatic Sea. Each vector combines the amplitude and phase of the vertical loading displacement. Red arrows indicate estimates derived from harmonic analysis of GNSS time series, while black arrows represent predictions from the FES2014b OT model. The reference system is defined by standard Cartesian coordinate axes, with positive angles measured counterclockwise. Phasors are represented in the complex plane, with the real component along the horizontal axis and the imaginary component along the vertical axis.

literature and are commonly attributed to the intrinsic limitations of GPS-based OTL estimation for the diurnal band. The K_1 period (23.93 h) nearly coincides with the repeat period of GPS satellite orbits ($\sim$ 23.93 h) and is therefore affected by aliasing and orbital errors (King, 2006; Abbaszadeh et al., 2020). This spectral overlap hampers the separation between true diurnal loading signals and orbit-related artifacts, producing biased amplitude and phase estimates. As shown by Abbaszadeh et al. (2020) and later confirmed by Wang et al. (2024), combining multiple GNSS constellations (e.g., GPS + GLONASS + Galileo) substantially improves the estimation of diurnal OTL displacements by reducing orbital resonance effects and enhancing spectral resolution. The discrepancies observed here

between the GNSS-derived K_1 phasors and FES2014b predictions are therefore consistent with the literature.

The O_1 constituent shows a more regular behavior; amplitudes are moderate, and the phase pattern remains spatially coherent, with estimated and modeled phasors generally aligned.

The P_1 constituent, on the other hand, exhibits the weakest modelled signal among all analyzed components. The estimated phasors are longer, differing substantially from the corresponding FES2014b vectors. Given its small equilibrium amplitude and strong sensitivity to observational noise, the solar diurnal P_1 tide is particularly difficult to resolve in GNSS-based analyses, and its discrepancies are within the expected uncertainty range. The frequency of P_1 is close to the one of K_1, therefore some aliasing are introcted as weel in this component.

The results for MEDI are significant only for M_2, as previously shown, as it is the only resolvable OT components.

Overall, the phasor distribution for the vertical displacement demonstrates that the Adriatic Sea exhibits a predominantly semidiurnal and good coherent elastic response to OTL. The semidiurnal constituents M_2 and N_2, and the diurnal O_1 are well reproduced by GNSS observations and show good agreement with the FES2014b model. Conversely, the diurnal constituents, especially K_1 and P_1, display notable deviations.

The phasor diagram in Figure 5.20 illustrates the horizontal OTL displacements in the Adriatic Sea for the two dominant constituents, M_2 (principal lunar semidiurnal) and K_1 (lunisolar diurnal), as derived from the GNSS-based harmonic analysis (red arrows) and compared with the FES2014b ocean tide model predictions (black arrows). Each phasor encodes both the amplitude and phase of the horizontal loading response, depicting the direction and timing of the crustal motion in the east–north plane.

For M_2, the horizontal deformation is spatially coherent and tracks the semidiurnal wave entering the Adriatic from the Otranto Strait. Estimated and modeled phasors align NW–SE, and the east component shows no appreciable phase shift relative to FES2014b. A small, nearly uniform lag appears only in the north component. PORE is excluded because its M_2 amplitude is not statistically significant (t-test).Amplitudes overall agree closely with the model, with a modest positive bias in the east component and a weaker response in the north.

In contrast, the K_1 constituent shows a more intricate pattern than M_2. In the east component, phases are broadly consistent with FES2014b across sta-

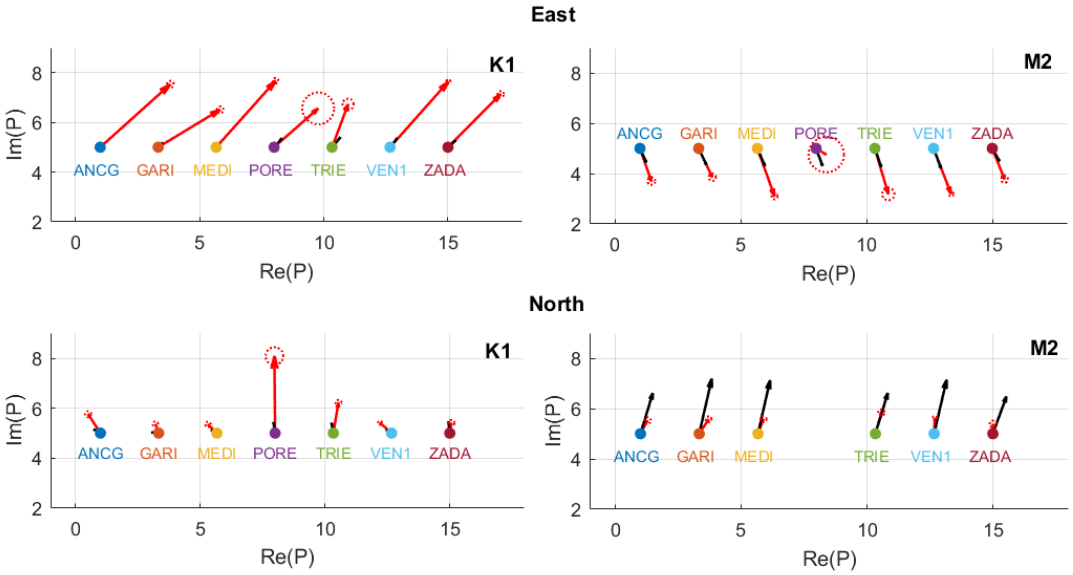

Figure 5.20: Phasor diagram illustrating horizontal ocean tide loading (OTL) displacements in the Adriatic Sea for the two dominant constituents: M_2 and K_1. Red arrows represent estimates from GNSS-based harmonic analysis, while black arrows show predictions from the FES2014b ocean tide model. Each phasor encodes both amplitude and phase of the horizontal loading response, indicating the direction and timing of crustal motion in the east–north plane. The reference system is defined by standard Cartesian coordinate axes, with positive angles measured counterclockwise. Phasors are represented in the complex plane, with the real component along the horizontal axis and the imaginary component along the vertical axis.

tions, TRIE is the only site showing a small offset, while amplitudes are strongly biased toward higher values, with a coherent amplification that can reach $\sim$8 times the model. The north component exhibits more scattered phases but amplitudes are comparatively uniform and closer to the model, with the exception of PORE. The diurnal signal remains spectrally strong, especially in K_1 east, but the near-resonance between the K_1 period (23.93 h) and the GNSS orbital/sidereal repeat, together with residual diurnal systematics (e.g., solar-day multipath and radiation-pressure mismodeling), can imprint aliasing that biases the recovered harmonic parameters. In this case, discrepancies are dominated by amplitude inflation rather than systematic phase rotation.

5.3.5 Discussion on ocean tides prediction in northern Adriatic

The combined analysis of TG, GNSS-R, and GNSS PPP-based ocean tides and loading results provides a comprehensive characterization of the tidal dynamics and the corresponding solid Earth response in the northern Adriatic basin. The TG records confirm the well-known amplification of semidiurnal constituents toward the northern shallow shelf, where M_2 and S_2 reach amplitudes comparable to or larger than the diurnal K_1 component. This progressive increase, consistent with the basin's geometry and bathymetry, reflects the near-resonant response of the Adriatic to semidiurnal forcing (Medvedev et al., 2020). The comparison with the FES2014b model demonstrates that, although the large-scale spatial trend is well captured, local deviations in amplitude and phase persist at individual stations, particularly along complex coastal segments such as Split and Zadar. These discrepancies likely stem from unresolved shallow-water effects and limitations in the global model's bathymetric representation (Martens et al., 2020).

GNSS-R results extend this characterization to locations without conventional TG, confirming the high spatial coherence of sea level variability along the northern Adriatic coast (Devoti et al., 2023). The strong correlation (above 90%) between GNSS-R derived SSH and nearby TG measurements demonstrates the ability of the reflectometry technique to resolve tidal and sub-tidal oscillations with centimeter level accuracy. The small amplitude discrepancies (2–3 cm) observed in the spectral domain are consistent with the expected attenuation from the limited number of valid reflections in some stations (Tabibi et al., 2020). Despite these constraints, GNSS-R effectively reproduces both the diurnal and semidiurnal tidal bands, supporting its suitability for continuous coastal sea level monitoring, particularly in areas where TGs are sparse or maintenance is difficult. The case study at Sistiana confirms this capability; the identified stable reflector at 7.2 m below the antenna corresponds to the mean sea surface, and the high correlation (94–95%) with nearby TGs at Trieste and Monfalcone, further validates the method under realistic field conditions. Moreover, it demonstrates the capability in SSH detection with the use of low cost antennas and limited GNSS constellations.

The GNSS PPP analysis complements the oceanographic observations by resolving the three-dimensional elastic response of the crust to OTL. The vertical OTL amplitudes derived from GNSS are in good agreement with those predicted

by the FES2014b model, confirming that the Adriatic Sea exerts a coherent semidiurnal loading signal along the basin margins. The M_2 constituent dominates both in amplitude and phase stability, showing excellent correspondence between observed and modeled phasors, while the N_2 component reproduces a similar pattern with reduced magnitude. The diurnal band, on the other hand, exhibits less consistency. The GNSS derived K_1 constituent shows systematic amplitude amplification and phase deviations with respect to the model, which can be attributed to the spectral interference between the 23.93-h tidal period and the GPS orbital repeat cycle. This near-resonance produces aliasing effects and residual orbit-related errors that bias the diurnal estimates. Such limitations have been widely reported in single-constellation GPS analyses and could be mitigated by multi-GNSS integration, which improves spectral separation and reduces orbit-induced artifacts (Matviichuk et al., 2020; Pan et al., 2023; Wang et al., 2024). The discrepancy is further emphasized by the TG results, which do not show comparable differences with the model predictions, confirming that the observed bias arises from the GNSS technique itself rather than from physical tidal or oceanographic processes.

The horizontal tidal loading deformation presents a similar contrast between semidiurnal and diurnal components. For M_2, both amplitude and direction of the GNSS-derived vectors align well with FES2014b, reflecting a coherent northwest–southeast motion parallel to the propagation of the tidal wave entering from the Otranto Strait. The overall amplitude differences remain at the millimeter level, with a slight positive bias in the east component and a small underestimation in the north component. Conversely, the K_1 horizontal displacements are more scattered and often overestimated in magnitude, again reflecting the limitations of resolving this diurnal constituents from GNSS. Nevertheless, the overall pattern of OTL deformation is spatially coherent across the network, confirming that even in a small and partially enclosed basin, the GNSS technique can resolve the main tidal loading modes at the millimeter level.

The GNSS results confirm the capability to resolve the main OTL components in the northern Adriatic region, particularly for the dominant vertical component. For TRIE, VEN1, and GARI, located furthest north among the analyzed stations, all principal tidal constituents (M_2, N_2, P_1, O_1, K_1) are successfully resolved. PORE, due to its higher noise level, does not allow for the full determination of all constituents, whereas ZADA, located on the same Adriatic coast, but further south, enables the estimation of all constituents except N_2. MEDI, despite ex-

hibiting the strongest M_2 amplitude due to the influence of the Tyrrhenian Sea, allows for the identification of only M_2 and K_1; the remaining constituents are too small to be detected, owing to its greater distance from the coastline. ANCG is the coastal station exhibiting the weakest OTL signal and, consequently, has a limited capability to detect tidal constituents above the noise level.

Chapter 6

Conclusions

This thesis set out to determine how reliably ocean tidal loading can be detected and quantified from GNSS coordinate time series, and how geodetic and oceanographic observations can be combined to characterize tides and their solid-Earth response in a shallow, semi-enclosed basin. The work advanced along two complementary tracks. First, a methodological assessment compared differential (DD) and absolute (PPP) positioning across contrasting tidal regimes, establishing what each strategy can and cannot recover at hourly periods. Second, a regional synthesis for the northern Adriatic integrated tide gauges (TG), GNSS reflectometry (GNSS-R), and GNSS-based OTL to map tidal dynamics and the associated 3-D deformation along the basin margins.

Concerning the methodological and feasibility analysis, the results conclude that applying modern OTL corrections is essential for millimetric geodesy. Regardless of processing strategy, introducing the OTL model reduces coordinate scatter systematically, up to $\sim 22\%$ in the vertical and $\sim 10-15\%$ in the horizontals, demonstrating that contemporary tide models capture the bulk of the sub-daily load. Yet the residual spectra retain coherent tidal energy, concentrated in the diurnal band, especially K_1, and secondarily in M_2. This underscores that the application of an OTL model does not, in itself, resolve the problem; model–data mismatches persist and should be examined on a constituent-by-constituent basis.

PPP appears to resolve a larger number of tidal constituents, particularly in the horizontal components, even though its time series often exhibit slightly higher noise than DD. The retrieved amplitudes show smaller discrepancies from the forward OTL model, whereas in DD the differencing attenuates small signals and can push minor constituents below the detection threshold, rendering them unresolved. This behavior is station and component dependent; in lower noise settings, DD detects the strongest lines, but for weak constituents the amplitude

loss inherent to differencing more often leads to non significance, while PPP retains them in the estimated spectrum.

Record length and noise level are decisive levers of detectability. Synthetic tests and real data agree; year-scale time series improve Rayleigh separation and stabilize weaker amplitudes, while shorter records can create partial aliasing between close constituents. Equally, a lower amplitude level of non tidal signals and acquisition noise enhances the amplitude to standard error ratio and raises constituents above significance, whereas elevated noise can render weak lines indistinguishable even over long durations.

The diurnal band shows a critical mismatch in some components. In PPP, K_1 residuals are systematically larger than semidiurnal constituents, with amplitude inflation and phase bias consistent with near-resonance between the 23.93 hour tidal period and GNSS orbital/sidereal repeats. DD mitigates, but does not eliminate, this effect. This pattern cautions against attributing diurnal misfits solely to ocean tides, as processing artifacts and orbit modeling limitations can dominate. In contrast, semidiurnal constituents, especially M_2, are robust. Amplitudes align closely with model predictions in both vertical and horizontal components.

The Adriatic provides a natural laboratory where these methodological insights translate into regional physics. Owing to its shallow, semi-enclosed geometry and large shelf, the basin exhibits the largest tidal ranges in the Mediterranean. TG analyses confirm a clear northward amplification of semidiurnal energy (M2, S2) and a spatially coherent phase structure; FES2014b reproduces the first-order pattern, with local amplitude/phase deviations likely tied to unresolved bathymetry and coastal complexity. GNSS-R extends sea level monitoring where TG coverage is limited: along the coast, GNSS-R sea levels correlate at $\sim$ 91–95% with nearby TGs, and the spectral content clearly resolves the principal diurnal and semidiurnal peaks with only 2–3 cm amplitude differences relative to TG. A focused case at Sistiana confirms feasibility under realistic constraints. Daily observations suffice for centimeter-level SSH and high correlation with nearby gauges, highlighting the accuracy of low cost instrumentation and not perfect conditions.

Bringing the geodetic and oceanographic strands together, GNSS-based OTL across the northern Adriatic resolves a predominantly semidiurnal, basin-coherent elastic response. Vertical phasors for M_2, and with smaller amplitudes N_2, match model predictions closely; horizontal vectors align NW–SE, tracking the semid-

iurnal wave that enters via the Otranto Strait. The diurnal band remains less consistent. K_1 shows phase and amplitude discrepancies relative to FES2014b that mirror known GNSS aliasing rather than a failure of the ocean model, an interpretation reinforced by TGs, which do not display comparable mismatches. Station by station, detection reflects local noise and exposure. Coastal northern sites (TRIE, VEN1, GARI) resolve all principal constituents in the vertical; noisier or inland sites (PORE, MEDI) detect only the strongest tides. Even so, the spatial pattern of horizontal OTL remains coherent at the millimeter level, underscoring the physical consistency of the joint solution.

Beyond the methodological advances, the societal relevance is direct. Along a densely populated, economically vital coastline, episodic flooding arises from the superposition of tides, surges, and subsidence. A monitoring architecture that fuses TG, GNSS-R, and GNSS-derived OTL provides both redundancy and reach. GNSS-R fills gaps in sea-level coverage. GNSS time series track millimetric crustal response. Together they sharpen hydrodynamic models, improve operational corrections for geodesy, and support coastal-risk assessment and adaptation planning under climate change.

The thesis reports the first documented hourly GNSS detection of OTL in the Adriatic Sea, showing that this geodetic technique can retrieve OTL signals below 1 cm when appropriately processed. While significance remains station dependent, the integrated framework combining hourly multi-GNSS positioning with TG and GNSS-R provides a cross validated, physically consistent view that links ocean forcing to solid Earth response. The approach is readily transferable to other semi-enclosed seas and wide shelves, strengthening operational geodetic corrections, refining hydrodynamic modelling, and supporting coastal risk assessment and adaptation under climate change.

Acknowledgements

I would like to express my gratitude to Prof. Carla Braitenberg, my supervisor, for her guidance and encouragement throughout my research journey. Her insight, enthusiasm and ability to inspire curiosity have greatly influenced the way I approach research and scientific thinking.

I am grateful to Dr. Roberto Devoti and Dr. Grazia Pietrantonio for having taught me so much and for guiding me, especially at the beginning of my research journey. The many long calls and discussions we had have taught me to think more critically, to question even the simplest things, and to reason with curiosity and depth. Their support and thoughtful advice have been essential to my personal and professional growth.

I would also like to thank the Diporto Nautico of Sistiana (DNS) for kindly offering us the location and support to install the multi-GNSS station.

I would also like to thank my colleagues and friends, who have been a strong point of support and a great help throughout this journey. Their encouragement, collaboration, and companionship have made the challenges easier.

Bibliography

Abbaszadeh, Majid, Peter J. Clarke, and Nigel T. Penna (July 2020)
"Benefits of combining GPS and GLONASS for measuring ocean tide loading displacement". en. In: *Journal of Geodesy* 94.7, p. 63. ISSN: 1432-1394. DOI: 10.1007/s00190-020-01393-5.

Abraha, K E, F N Teferle, A Hunegnaw, and R Dach (Sept. 2018)
"Effects of unmodelled tidal displacements in GPS and GLONASS coordinate time-series". en. In: *Geophysical Journal International* 214.3, pp. 2195–2206. ISSN: 0956-540X, 1365-246X. DOI: 10.1093/gji/ggy254.

Ait-Lakbir, H., A. Santamaría-Gómez, and F. Perosanz (May 2023)
"Assessment of sub-daily ocean tide loading errors and mitigation of their propagation in multi-GNSS position time series". en. In: *GPS Solutions* 27.3, p. 129. ISSN: 1521-1886. DOI: 10.1007/s10291-023-01467-9.

Allinson, C. R. (2004)
Stability of direct GPS estimates of ocean tide loading. en. DOI: 10.1029/2004GL020588.

Alterman, Z., H. Jarosch, and C. L. Pekeris (Aug. 1959)
"Oscillations of the Earth". In: *Proceedings of the Royal Society of London Series A* 252, pp. 80–95. ISSN: 0080-46301364-5021. DOI: 10.1098/rspa.1959.0138.

Altuntas, Cemali and Nursu Tunalioglu (Nov. 2021)
"GIRAS: an open-source MATLAB-based software for GNSS-IR analysis". en. In: *GPS Solutions* 26.1, p. 16. ISSN: 1521-1886. DOI: 10.1007/s10291-021-01201-3.

Altuntas, Cemali and Nursu Tunalioglu (2023)
"Enhancing Snow Depth Estimations Through Iterative Satellite Elevation Range Selection in GNSS-IR to Account for Terrain Variation". In: *IEEE Transactions on Geoscience and Remote Sensing* 61, pp. 1–9. ISSN: 1558-0644. DOI: 10.1109/TGRS.2023.3312925.

Banville, Simon, Jianghui Geng, Sylvain Loyer, Stefan Schaer, Tim Springer, and Sebastian Strasser (Jan. 2020)
"On the interoperability of IGS products for precise point positioning with

ambiguity resolution". en. In: *Journal of Geodesy* 94.1, p. 10. ISSN: 1432-1394. DOI: 10.1007/s00190-019-01335-w.

Bevis, Michael, Steven Businger, Steven Chiswell, Thomas A. Herring, Richard A. Anthes, Christian Rocken, and Randolph H. Ware (Mar. 1994) "GPS Meteorology: Mapping Zenith Wet Delays onto Precipitable Water". EN. In: *Journal of Applied Meteorology and Climatology* 33.3, pp. 379–386. ISSN: 1520-0450, 0894-8763. DOI: 10.1175/1520-0450(1994)033<0379:GMMZWD>2.0.CO;2.

Bilich, Andria, Kristine M. Larson, and Penina Axelrad (2008) "Modeling GPS phase multipath with SNR: Case study from the Salar de Uyuni, Boliva". en. In: *Journal of Geophysical Research: Solid Earth* 113.B4. _eprint: https://agupubs.onlinelibrary.wiley.com/doi/pdf/10.1029/2007JB005194. ISSN: 2156-2202. DOI: 10.1029/2007JB005194.

Blewitt, G. (2015) "GPS and Space-Based Geodetic Methods". en. In: *Treatise on Geophysics*. Elsevier, pp. 307–338. ISBN: 978-0-444-53803-1. DOI: 10.1016/B978-0-444-53802-4.00060-9.

Blewitt, Geoffrey and David Lavallée (2002) "Effect of annual signals on geodetic velocity". en. In: *Journal of Geophysical Research: Solid Earth* 107.B7, ETG 9–1–ETG 9–11. ISSN: 2156-2202. DOI: 10.1029/2001JB000570.

Boehm, Johannes, Birgit Werl, and Harald Schuh (2006) "Troposphere mapping functions for GPS and very long baseline interferometry from European Centre for Medium-Range Weather Forecasts operational analysis data". en. In: *Journal of Geophysical Research: Solid Earth* 111.B2. ISSN: 2156-2202. DOI: 10.1029/2005JB003629.

Bogusz, Janusz and Anna Klos (Oct. 2016) "On the significance of periodic signals in noise analysis of GPS station coordinates time series". en. In: *GPS Solutions* 20.4, pp. 655–664. ISSN: 1521-1886. DOI: 10.1007/s10291-015-0478-9.

Bos, Machiel S., Nigel T. Penna, Trevor F. Baker, and Peter J. Clarke (2015) "Ocean tide loading displacements in western Europe: GPS-observed anelastic dispersion in the asthenosphere". en. In: *Journal of Geophysical Research: Solid Earth* 120.9, pp. 6540–6557. ISSN: 2169-9356. DOI: 10.1002/2015JB011884.

Bruyninx, Carine, Juliette Legrand, András Fabian, and Eric Pottiaux (Oct. 2019)

"GNSS metadata and data validation in the EUREF Permanent Network". en. In: *GPS Solutions* 23.4, p. 106. ISSN: 1080-5370, 1521-1886. DOI: 10.1007/s10291-019-0880-9.

Camuffo, Dario (Feb. 2023)

"The Treatise on Waters by Cornaro (1560) and a quantitative assessment of the historical sea surges "Acqua Alta" in Venice". en. In: *Climatic Change* 176.3, p. 18. ISSN: 1573-1480. DOI: 10.1007/s10584-023-03492-6.

Candela, Julio, Clinton Winant, and Antonio Ruiz (May 1990)

"Tides in the Strait of Gibraltar". en. In: *Journal of Geophysical Research: Oceans* 95.C5. Publisher: John Wiley & Sons, Ltd, pp. 7313–7335. ISSN: 2156-2202. DOI: 10.1029/JC095iC05p07313.

Chen, G. and T. A. Herring (1997)

"Effects of atmospheric azimuthal asymmetry on the analysis of space geodetic data". en. In: *Journal of Geophysical Research: Solid Earth* 102.B9, pp. 20489–20502. ISSN: 2156-2202. DOI: 10.1029/97JB01739.

Chiaruttini, Claudio (Sept. 1976)

"Tidal Loading on the Italian Peninsula". In: *Geophysical Journal International* 46.3, pp. 773–793. ISSN: 0956-540X. DOI: 10.1111/j.1365-246X.1976.tb01257.x.

Codiga, Daniel (Sept. 2011)

Unified tidal analysis and prediction using the UTide Matlab functions. DOI: 10.13140/RG.2.1.3761.2008.

Dach, Rolf and Reinhard Dietrich (2000)

"Influence of the ocean loading effect on GPS derived precipitable water vapor". en. In: *Geophysical Research Letters* 27.18, pp. 2953–2956. ISSN: 1944-8007. DOI: 10.1029/1999GL010970.

Dach, Rolf, Simon Lutz, Peter Walser, and Pierre Fridez (2015)

Bernese GNSS Software Version 5.2. eng. Ed. by Rolf Dach, Simon Lutz, Peter Walser, and Pierre Fridez. Publication Title: Dach, Rolf; Lutz, Simon; Walser, Peter; Fridez, Pierre (eds.) (2015). Bernese GNSS Software Version 5.2. Bern: University of Bern, Bern Open Publishing. Bern: University of Bern, Bern Open Publishing. ISBN: 978-3-906813-05-9.

Devoti, Roberto, Sergio Bruni, and Grazia Pietrantonio (Sept. 2023)

"GNSS-Interferometric Reflectometry, spectral artifacts and sea level measurements in the Mediterranean Sea". en. In: *Journal of Geography and Cartography* 6.2, p. 2358. ISSN: 2578-1979. DOI: 10.24294/jgc.v6i2.2358.

Dey, Abhijit and Dr.V.Malleswara Rao (2014)

"Study and analysis of Differential GNSS and Precise Point Positioning". en. In: *IOSR Journal of Electrical and Electronics Engineering* 9.2, pp. 53–59. ISSN: 23203331, 22781676. DOI: 10.9790/1676-09215359.

Dong, D., P. Fang, Y. Bock, F. Webb, L. Prawirodirdjo, S. Kedar, and P. Jamason (2006)

"Spatiotemporal filtering using principal component analysis and Karhunen-Loeve expansion approaches for regional GPS network analysis". en. In: *Journal of Geophysical Research: Solid Earth* 111.B3. ISSN: 2156-2202. DOI: 10.1029/2005JB003806.

Doodson, Arthur Thomas and Horace Lamb (Jan. 1997)

"The harmonic development of the tide-generating potential". In: *Proceedings of the Royal Society of London. Series A, Containing Papers of a Mathematical and Physical Character* 100.704. Publisher: Royal Society, pp. 305–329. DOI: 10.1098/rspa.1921.0088.

Egbert, Gary D. and Svetlana Y. Erofeeva (Feb. 2002)

"Efficient Inverse Modeling of Barotropic Ocean Tides". en. In: Section: Journal of Atmospheric and Oceanic Technology. ISSN: 1520-0426.

Farina, P., R. E. M. Riva, and F. J. Simons (2013)

"Improving ocean tidal loading predictions in coastal and semi-enclosed basins". In: *Journal of Geophysical Research: Solid Earth* 118, pp. 6216–6230. DOI: 10.1002/jgrb.50491.

Farrell, W. E. (1972)

"Deformation of the Earth by surface loads". en. In: *Reviews of Geophysics* 10.3, pp. 761–797. ISSN: 1944-9208. DOI: 10.1029/RG010i003p00761.

Foreman, M. (Jan. 1977)

"Manual for Tidal Heights Analysis and Prediction". In: *Pac. Mar. Sci. Rep.* 77–10.

Foreman, M. G. G., J. Y. Cherniawsky, and V. A. Ballantyne (Apr. 2009)

"Versatile Harmonic Tidal Analysis: Improvements and Applications". en. In: Section: Journal of Atmospheric and Oceanic Technology. DOI: 10.1175/2008JTECHO615.1.

Foreman, M. G. G. and R. F. Henry (Sept. 1989)

"The harmonic analysis of tidal model time series". In: *Advances in Water Resources* 12.3, pp. 109–120. ISSN: 0309-1708. DOI: 10.1016/0309-1708(89)90017-1.

Gabor, Michael Joseph (Nov. 1999)

"GPS carrier phase ambiguity resolution using satellite-satellite single differences". ADS Bibcode: 1999PhDT.....223G. Ph.D. thesis.

Geng, Jianghui, Qiang Wen, Qiyuan Zhang, Guangcai Li, and Kunlun Zhang (Feb. 2022)

"GNSS observable-specific phase biases for all-frequency PPP ambiguity resolution". en. In: *Journal of Geodesy* 96.2, p. 11. ISSN: 1432-1394. DOI: 10.1007/s00190-022-01602-3.

Geremia-Nievinski, Felipe and Thomas Hobiger (Oct. 2019)

"Site guidelines for multi-purpose GNSS reflectometry stations". eng. In: Publisher: Zenodo. DOI: 10.5281/zenodo.5335890.

Godin, Gabriel (1972)

The Analysis of Tides. en. Google-Books-ID: rxUIAQAAIAAJ. University of Toronto Press. ISBN: 978-0-8020-1747-5.

Guarnieri, A., N. Pinardi, P. Oddo, G. Bortoluzzi, and M. Ravaioli (Jan. 2013)

"Impact of tides in a baroclinic circulation model of the Adriatic Sea". en. In: *Journal of Geophysical Research: Oceans* 118.1. Publisher: John Wiley & Sons, Ltd, pp. 166–183. ISSN: 2169-9291. DOI: 10.1029/2012JC007921.

Guerova, Guergana, Jonathan Jones, Jan Douša, Galina Dick, Siebren de Haan, Eric Pottiaux, Olivier Bock, Rosa Pacione, Gunnar Elgered, Henrik Vedel, and Michael Bender (Nov. 2016)

"Review of the state of the art and future prospects of the ground-based GNSS meteorology in Europe". English. In: *Atmospheric Measurement Techniques* 9.11. Publisher: Copernicus GmbH, pp. 5385–5406. ISSN: 1867-1381. DOI: 10.5194/amt-9-5385-2016.

Hart-Davis, Michael, Gaia Piccioni, Denise Dettmering, Christian Schwatke, Marcello Passaro, and Florian Seitz (2021)

EOT20 - A global Empirical Ocean Tide model from multi-mission satellite altimetry. DOI: 10.17882/79489.

Hernández-Pajares, M., J. M. Juan, J. Sanz, and R. Orús (2007)

"Second-order ionospheric term in GPS: Implementation and impact on geodetic estimates". en. In: *Journal of Geophysical Research: Solid Earth* 112.B8. ISSN: 2156-2202. DOI: 10.1029/2006JB004707.

"Data processing" (2008). en. In: *GNSS — Global Navigation Satellite Systems: GPS, GLONASS, Galileo, and more*. Ed. by Bernhard Hofmann-Wellenhof,

Herbert Lichtenegger, and Elmar Wasle. Vienna: Springer, pp. 193–276. ISBN: 978-3-211-73017-1. DOI: 10.1007/978-3-211-73017-1_7.

Jacobs, Gregg A., George H. Born, Mike E. Parke, and Patrick C. Allen (1992) "The global structure of the annual and semiannual sea surface height variability from Geosat altimeter data". en. In: *Journal of Geophysical Research: Oceans* 97.C11, pp. 17813–17828. ISSN: 2156-2202. DOI: 10.1029/92JC01708.

Janeković, Ivica and M. Kuzmić (Nov. 2005) "Numerical simulation of the Adriatic Sea principal tidal constituents". In: *Annales Geophysicae* 23, pp. 3207–3218. DOI: 10.5194/angeo-23-3207-2005.

Jin, Shuanggen and Attila Komjathy (July 2010) "GNSS reflectometry and remote sensing: New objectives and results". In: *Advances in Space Research*. GNSS Remote Sensing-1 46.2, pp. 111–117. ISSN: 0273-1177. DOI: 10.1016/j.asr.2010.01.014.

Kaplan, Elliott D. and Christopher Hegarty (May 2017) *Understanding GPS/GNSS: Principles and Applications, Third Edition*. en. Google-Books-ID: y4Q0DwAAQBAJ. Artech House. ISBN: 978-1-63081-442-7.

Kaplan, Elliott D. and Christopher J. Hegarty, eds. (2006) *Understanding GPS: principles and applications*. en. Second edition. Artech House mobile communications series. Boston London: Artech House. ISBN: 978-1-58053-894-7 978-1-58053-895-4.

Katzberg, Stephen J., Jason Dunion, and George G. Ganoe (2013) "The use of reflected GPS signals to retrieve ocean surface wind speeds in tropical cyclones". en. In: *Radio Science* 48.4, pp. 371–387. ISSN: 1944-799X. DOI: 10.1002/rds.20042.

Khan, Shfaqat Abbas and Hans-Georg Scherneck (2002) "The M2 ocean tide loading wave in Alaska: Vertical and horizontal displacements, modelled and observed | Request PDF". en. In: *ResearchGate*. DOI: 10.1007/s00190-003-0312-y.

King, Matt (Jan. 2006) "Kinematic and static GPS techniques for estimating tidal displacements with application to Antarctica". In: *Journal of Geodynamics*. Earth Tides and Geodynamics: Probing the Earth at Sub-Seismic Frequencies 41.1, pp. 77–86. ISSN: 0264-3707. DOI: 10.1016/j.jog.2005.08.019.

King, Matt, Nigel Penna, Peter Clarke, and Ed King (Aug. 2005)
"Validation of ocean tide models around Antarctica using onshore GPS and gravity data". In: *Journal of Geophysical Research* 110. DOI: 10.1029/2004JB003390.

Klobuchar, John A. (May 1987)
"Ionospheric Time-Delay Algorithm for Single-Frequency GPS Users". In: *IEEE Transactions on Aerospace and Electronic Systems* AES-23.3, pp. 325–331. ISSN: 1557-9603. DOI: 10.1109/TAES.1987.310829.

Kouba, Jan and Pierre Héroux (Oct. 2001)
"Precise Point Positioning Using IGS Orbit and Clock Products". en. In: *GPS Solutions* 5.2, pp. 12–28. ISSN: 1521-1886. DOI: 10.1007/PL00012883.

Lambeck, Kurt (Jan. 1988)
Geophysical geodesy - The slow deformations of the earth. Publication Title: Research supported by CNES and Universite de Paris VI. Oxford and New York ADS Bibcode: 1988oxny.book.....L.

Landskron, Daniel and Johannes Böhm (Apr. 2018)
"VMF3/GPT3: refined discrete and empirical troposphere mapping functions". en. In: *Journal of Geodesy* 92.4, pp. 349–360. ISSN: 1432-1394. DOI: 10.1007/s00190-017-1066-2.

Larson, Kristine M. (July 2024)
"Gnssrefl: an open source software package in python for GNSS interferometric reflectometry applications". en. In: *GPS Solutions* 28.4, p. 165. ISSN: 1521-1886. DOI: 10.1007/s10291-024-01694-8.

Larson, Kristine M., Johan S. Löfgren, and Rüdiger Haas (Apr. 2013)
"Coastal sea level measurements using a single geodetic GPS receiver". In: *Advances in Space Research*. Satellite Altimetry Calibration and Deformation Monitoring using GNSS 51.8, pp. 1301–1310. ISSN: 0273-1177. DOI: 10.1016/j.asr.2012.04.017.

Larson, Kristine M., Richard D. Ray, and Simon D. P. Williams (Feb. 2017)
"A 10-Year Comparison of Water Levels Measured with a Geodetic GPS Receiver versus a Conventional Tide Gauge". en. In: *Journal of Atmospheric and Oceanic Technology* 34.2. Publisher: American Meteorological Society, pp. 295–307. ISSN: 0739-0572, 1520-0426. DOI: 10.1175/jtech-d-16-0101.1.

Leick, Alfred, Lev Rapoport, and Dmitry Tatarnikov (Mar. 2015)
GPS Satellite Surveying. en. Google-Books-ID: WvtgBgAAQBAJ. John Wiley & Sons. ISBN: 978-1-118-67557-1.

Li, Zhao, Wu Chen, Weiping Jiang, Liansheng Deng, and Ronghua Yang (July 2018)

"The Magnitude of Diurnal/Semidiurnal Atmospheric Tides (S1/S2) and Their Impacts on the Continuous GPS Coordinate Time Series". en. In: *Remote Sensing* 10.7, p. 1125. ISSN: 2072-4292. DOI: 10.3390/rs10071125.

Liu, Z., L. Du, P. Zhou, X. Wang, and Z. Zhang (2022)

"Cloud-based near real-time sea level monitoring using GNSS reflectometry". In: *GPS Solutions* 27. DOI: 10.1007/s10291-022-01382-5.

Lomb, N. R. (Feb. 1976)

"Least-squares frequency analysis of unequally spaced data". en. In: *Astrophysics and Space Science* 39.2, pp. 447–462. ISSN: 1572-946X. DOI: 10.1007/BF00648343.

Loyer, Sylvain, Félix Perosanz, Flavien Mercier, Hugues Capdeville, and Jean-Charles Marty (Nov. 2012)

"Zero-difference GPS ambiguity resolution at CNES–CLS IGS Analysis Center". en. In: *Journal of Geodesy* 86.11, pp. 991–1003. ISSN: 1432-1394. DOI: 10.1007/s00190-012-0559-2.

Lyard, Florent, Fabien Lefevre, Thierry Letellier, and Olivier Francis (Dec. 2006)

"Modelling the global ocean tides: modern insights from FES2004". en. In: *Ocean Dynamics* 56.5, pp. 394–415. ISSN: 1616-7228. DOI: 10.1007/s10236-006-0086-x.

Lyard, Florent H., Damien J. Allain, Mathilde Cancet, Loren Carrère, and Nicolas Picot (May 2021)

"FES2014 global ocean tide atlas: design and performance". English. In: *Ocean Science* 17.3. Publisher: Copernicus GmbH, pp. 615–649. ISSN: 1812-0784. DOI: 10.5194/os-17-615-2021.

Ma, Xiongwei, Xinzhe Wang, Yibin Yao, Hang Zhu, Bao Zhang, Ruitao Chu, Qi Zhang, and Yangmin Feng (Mar. 2025)

"Enhanced multi-GNSS precise point positioning based on ERA5 precipitation water vapor information". en. In: *Journal of Geodesy* 99.3, p. 24. ISSN: 1432-1394. DOI: 10.1007/s00190-025-01948-4.

Macdonald, Gordon James Fraser (1975)

The rotation of the earth: a geophysical discussion. Cambridge University Press.

Martens, Luis Rivera, and Mark Simons (2019)

"LoadDef: A Python-Based Toolkit to Model Elastic Deformation Caused by

Surface Mass Loading on Spherically Symmetric Bodies". en. In: *Earth and Space Science* 6.2, pp. 311–323. ISSN: 2333-5084. DOI: 10.1029/2018EA000462.

Martens and M Simons (Oct. 2020)

"A comparison of predicted and observed ocean tidal loading in Alaska". en. In: *Geophysical Journal International* 223.1, pp. 454–470. ISSN: 0956-540X, 1365-246X. DOI: 10.1093/gji/ggaa323.

Martens, Mark Simons, Susan Owen, and Luis Rivera (June 2016)

"Observations of ocean tidal load response in South America from subdaily GPS positions". en. In: *Geophysical Journal International* 205.3, pp. 1637–1664. ISSN: 0956-540X, 1365-246X. DOI: 10.1093/gji/ggw087.

Matviichuk, Bogdan, Matt King, and Christopher Watson (Oct. 2020)

"Estimating ocean tide loading displacements with GPS and GLONASS". en. In: *Solid Earth* 11.5, pp. 1849–1863. ISSN: 1869-9529. DOI: 10.5194/se-11-1849-2020.

Matviichuk, Bogdan, Matt King, Christopher Watson, and Machiel Bos (Aug. 2023)

"Comparison of state-of-the-art GNSS-observed and predicted ocean tide loading displacements across Australia". en. In: *Journal of Geodesy* 97.8, p. 78. ISSN: 1432-1394. DOI: 10.1007/s00190-023-01767-5.

Medvedev, Igor P., Ivica Vilibić, and Alexander B. Rabinovich (2020)

"Tidal Resonance in the Adriatic Sea: Observational Evidence". In: *Journal of Geophysical Research: Oceans* 125.8, e2020JC016168. DOI: 10.1029/2020JC016168.

Melchior, P. (Jan. 1983)

The tides of the planet earth.

Misra, Pratap and Per Enge (Jan. 2002)

"Global Positioning System: Signals, Measurements, and Performance". In: *IEEE Aerospace and Electronic Systems Magazine* 17. Publisher: IEEE ADS Bibcode: 2002IAESM..17j..36M, pp. 36–37. DOI: 10.1109/MAES.2002.1044515.

Montenbruck, Oliver, Peter Steigenberger, and André Hauschild (June 2014)

"Broadcast Versus Precise Ephemerides: A Multi-GNSS Perspective". In: *GPS Solutions* 19. DOI: 10.1007/s10291-014-0390-8.

Mooney, Christopher (1997)

Monte Carlo Simulation. en. SAGE Publications, Inc. ISBN: 978-1-4129-8511-6. DOI: 10.4135/9781412985116.

Nievinski, Felipe G. and Kristine M. Larson (Apr. 2014)

"Forward modeling of GPS multipath for near-surface reflectometry and positioning applications". en. In: *GPS Solutions* 18.2, pp. 309–322. ISSN: 1080-5370, 1521-1886. DOI: 10.1007/s10291-013-0331-y.

Ogaja, Clement A. (2022)

"Estimating Geodetic Parameters from GNSS". en. In: *Introduction to GNSS Geodesy: Foundations of Precise Positioning Using Global Navigation Satellite Systems*. Ed. by Clement A. Ogaja. Cham: Springer International Publishing, pp. 51–60. ISBN: 978-3-030-91821-7. DOI: 10.1007/978-3-030-91821-7_4.

Ordóñez, Celestino, Javier Martínez, José Rodríguez-Pérez, and A. Reyes (Nov. 2011)

"Detection of Outliers in GPS Measurements by Using Functional-Data Analysis". In: *Journal of Surveying Engineering* 137, pp. 150–155. DOI: 10.1061/(ASCE)SU.1943-5428.0000056.

Othmani, Achref, Béchir Béjaoui, Cristèle Chevalier, Dalila Elhmaidi, Jean-Luc Devenon, and Lotfi Aleya (May 2017)

"High-resolution numerical modelling of the barotropic tides in the Gulf of Gabes, eastern Mediterranean Sea (Tunisia)". In: *Journal of African Earth Sciences* 129, pp. 224–232. ISSN: 1464-343X. DOI: 10.1016/j.jafrearsci.2017.01.007.

Pan, Haidong, Xiaoqing Xu, Huayi Zhang, Tengfei Xu, and Zexun Wei (Jan. 2023)

"A Novel Method to Improve the Estimation of Ocean Tide Loading Displacements for K1 and K2 Components with GPS Observations". en. In: *Remote Sensing* 15.11. Publisher: Multidisciplinary Digital Publishing Institute, p. 2846. ISSN: 2072-4292. DOI: 10.3390/rs15112846.

Parkinson, Bradford W. and James J. Spilker (1996)

Global Positioning System: Theory and Applications. en. Google-Books-ID: lvI1a5J_4ewC. AIAA. ISBN: 978-1-60086-419-3.

Penna, Peter J. Clarke, Machiel S. Bos, and Trevor F. Baker (2015)

"Ocean tide loading displacements in western Europe: 1. Validation of kinematic GPS estimates". en. In: *Journal of Geophysical Research: Solid Earth* 120.9, pp. 6523–6539. ISSN: 2169-9356. DOI: 10.1002/2015JB011882.

Penna and Stewart (2003)

"Aliased tidal signatures in continuous GPS height time series". en. In: *Geophysical Research Letters* 30.23. ISSN: 1944-8007. DOI: 10.1029/2003GL018828.

Perosanz, H., A. Santamaría-Gómez, et al. (2023)
"Assessment of sub-daily ocean tide loading errors and mitigation of their propagation in multi-GNSS position time series". In: *GPS Solutions* 27. DOI: 10.1007/s10291-023-01467-9.

Petit, Gerard and Brian Luzum (2010)
"IERS Conventions (2010)". en. In: Verlag des Bundesamts für Kartographie und Geodäsie, Frankfurt am Main.

Petrov, L., J.-P. Boy, Y. Rogister, and N. T. Penna (2021)
"Detection and validation of ocean tidal loading displacements using GNSS". In: *Journal of Geodesy* 95. DOI: 10.1007/s00190-021-01531-8.

Pintori, Francesco, Enrico Serpelloni, and Adriano Gualandi (Oct. 2022)
"Common-mode signals and vertical velocities in the greater Alpine area from GNSS data". English. In: *Solid Earth* 13.10, pp. 1541–1567. ISSN: 1869-9510. DOI: 10.5194/se-13-1541-2022.

Poulain, Pierre-Marie (2013)
"Tidal currents in the Adriatic as measured by surface drifters". In: *Journal of Geophysical Research: Oceans* 118.C3, pp. 1434–1448. DOI: 10.1002/jgrc.20147.

Pugh, David and Philip Woodworth (Apr. 2014)
Sea-Level Science: Understanding Tides, Surges, Tsunamis and Mean Sea-Level Changes. en. Google-Books-ID: OAJeAwAAQBAJ. Cambridge University Press. ISBN: 978-1-139-91633-2.

R. Dach, R. Dietrich (Jan. 2001)
"The Ocean Loading Effect in the GPS Analysis: A Case Study in the Antarctic Peninsula Region". EN. In: *Marine Geodesy*. Publisher: Informa UK Ltd. ISSN: 1014-3793. DOI: 10.1080/01490410116803.

Ray, J., Z. Altamimi, X. Collilieux, and T. van Dam (Jan. 2008)
"Anomalous harmonics in the spectra of GPS position estimates". en. In: *GPS Solutions* 12.1, pp. 55–64. ISSN: 1521-1886. DOI: 10.1007/s10291-007-0067-7.

Ray, R. D. (2013)
"Precise comparisons of bottom-pressure and altimetric ocean tides". en. In: *Journal of Geophysical Research: Oceans* 118.9, pp. 4570–4584. ISSN: 2169-9291. DOI: 10.1002/jgrc.20336.

Riccardi, Umberto, Umberto Tammaro, and Paolo Capuano (Sept. 2021)
"Tropospheric Delay in the Neapolitan and Vesuvius Areas (Italy) by Means

of a Dense GPS Array: A Contribution for Weather Forecasting and Climate Monitoring". en. In: *Atmosphere* 12.9, p. 1225. ISSN: 2073-4433. DOI: 10.3390/atmos12091225.

Rizos, Chris, Volker Janssen, C Roberts, and T Grinter (Jan. 2012)
"Precise Point Positioning: Is the era of differential GNSS positioning drawing to an end?" In.

Rus, Marko, Anja Fettich, Matej Kristan, and Matjaž Ličer (Jan. 2023)
"HIDRA2: deep-learning ensemble sea level and storm tide forecasting in the presence of seiches – the case of the northern Adriatic". English. In: *Geoscientific Model Development* 16.1. Publisher: Copernicus GmbH, pp. 271–288. ISSN: 1991-959X. DOI: 10.5194/gmd-16-271-2023.

Saastamoinen, J. (1972)
"Atmospheric Correction for the Troposphere and Stratosphere in Radio Ranging Satellites". en. In: *The Use of Artificial Satellites for Geodesy*. American Geophysical Union (AGU), pp. 247–251. ISBN: 978-1-118-66364-6.

Saastamoinen, J. (Mar. 2013)
"Atmospheric Correction for the Troposphere and Stratosphere in Radio Ranging Satellites". en. In: Book Title: The Use of Artificial Satellites for Geodesy Publisher: American Geophysical Union (AGU), pp. 247–251. DOI: 10.1029/GM015p0247.

Scargle, J. D. (Dec. 1982)
"Studies in astronomical time series analysis. II. Statistical aspects of spectral analysis of unevenly spaced data." In: *The Astrophysical Journal* 263. Publisher: IOP ADS Bibcode: 1982ApJ...263..835S, pp. 835–853. ISSN: 0004-637X. DOI: 10.1086/160554.

Schaer, Stefan, Gerhard Beutler, and Markus Rothacher (1999)
"MAPPING AND PREDICTING THE IONOSPHERE". en. In.

Shannon, C.E. (Jan. 1949)
"Communication in the Presence of Noise". In: *Proceedings of the IRE* 37.1. Conference Name: Proceedings of the IRE, pp. 10–21. ISSN: 2162-6634. DOI: 10.1109/JRPROC.1949.232969.

Tabibi, S., F. Geremia-Nievinski, O. Francis, and T. van Dam (2020)
"Tidal analysis of GNSS reflectometry applied for coastal sea level sensing in Antarctica and Greenland". In: *Remote Sensing of Environment* 248, p. 111959. DOI: 10.1016/j.rse.2020.111959.

Teunissen, Peter JG, Oliver Montenbruck, et al. (2017)

Springer handbook of global navigation satellite systems. Vol. 10. Springer.

Thayer, Gordon D. (1974)

"An improved equation for the radio refractive index of air". en. In: *Radio Science* 9.10, pp. 803–807. ISSN: 1944-799X. DOI: 10.1029/RS009i010p00803.

Tsimplis, M. N., R. Proctor, and R. A. Flather (Aug. 1995)

"A two-dimensional tidal model for the Mediterranean Sea". en. In: *Journal of Geophysical Research: Oceans* 100.C8. Publisher: John Wiley & Sons, Ltd, pp. 16223–16239. ISSN: 2156-2202. DOI: 10.1029/95JC01671.

Vey, S., E. Calais, M. Llubes, N. Florsch, G. Woppelmann, J. Hinderer, M. Amalvict, M. F. Lalancette, B. Simon, F. Duquenne, and J. S. Haase (Nov. 2002)

"GPS measurements of ocean loading and its impact on zenith tropospheric delay estimates: a case study in Brittany, France". en. In: *Journal of Geodesy* 76.8, pp. 419–427. ISSN: 0949-7714, 1432-1394. DOI: 10.1007/s00190-002-0272-7.

Wahr, John M. (Mar. 1981)

"Body tides on an elliptical, rotating, elastic and oceanless earth". en. In: *Geophysical Journal International* 64.3. Publisher: Oxford Academic, pp. 677–703. ISSN: 0956-540X. DOI: 10.1111/j.1365-246X.1981.tb02690.x.

Wang, Hao, Na Wei, Min Li, Shin-Chan Han, Rongxin Fang, and Qile Zhao (Nov. 2023)

"Estimation of GPS-observed ocean tide loading displacements with an improved harmonic analysis in the northwest European shelf". en. In: *Journal of Geodesy* 97.12, p. 108. ISSN: 1432-1394. DOI: 10.1007/s00190-023-01796-0.

Wang, Hao, Na Wei, Min Li, Shin-Chan Han, Yunfei Xiang, and Qile Zhao (Oct. 2024)

"Benefits of tidal admittance functions for refining GNSS-observed solar and lunisolar tidal constituents". en. In: *GPS Solutions* 29.1, p. 13. ISSN: 1521-1886. DOI: 10.1007/s10291-024-01768-7.

Wei, Kejie Chen, and Run Ji (Dec. 2021)

"Improving estimates of ocean tide loading displacements with multi-GNSS: a case study of Hong Kong". en. In: *GPS Solutions* 26.1, p. 25. ISSN: 1521-1886. DOI: 10.1007/s10291-021-01212-0.

Yuan, Linguo, Benjamin Fong Chao, Xiaoli Ding, and Ping Zhong (2013)

"The tidal displacement field at Earth's surface determined using global GPS

observations". en. In: *Journal of Geophysical Research: Solid Earth* 118.5, pp. 2618–2632. ISSN: 2169-9356. DOI: 10.1002/jgrb.50159.

Zajdel, Radosław, Kamil Kazmierski, and Krzysztof Sośnica (2022)
"Orbital Artifacts in Multi-GNSS Precise Point Positioning Time Series". en. In: *Journal of Geophysical Research: Solid Earth* 127.2, e2021JB022994. ISSN: 2169-9356. DOI: 10.1029/2021JB022994.

Zavorotny, Valery U., Scott Gleason, Estel Cardellach, and Adriano Camps (Dec. 2014)
"Tutorial on Remote Sensing Using GNSS Bistatic Radar of Opportunity". In: *IEEE Geoscience and Remote Sensing Magazine* 2.4, pp. 8–45. ISSN: 2168-6831. DOI: 10.1109/MGRS.2014.2374220.

Zumberge, J. F., M. B. Heflin, D. C. Jefferson, M. M. Watkins, and F. H. Webb (1997)
"Precise point positioning for the efficient and robust analysis of GPS data from large networks". en. In: *Journal of Geophysical Research: Solid Earth* 102.B3. yuan, pp. 5005–5017. ISSN: 2156-2202. DOI: 10.1029/96JB03860.

Appendices

Appendix A

Station list

Table A.1: GNSS CASC fiducial stations coordinates and database for data processing.

Station name	**Latitude (°)**	**Longitude (°)**	**Database**
CASC	38.6934	-9.4185	EUREF
VILL	40.4436	-3.9520	IGS
ACOR	43.3644	-8.3989	EUREF
ALAC	38.3389	-0.4812	EUREF
ALME	36.8525	-2.4594	EUREF
CACE	39.479	-6.34	EUREF
CEU1	35.8920	-8.3989	EUREF
MELI	35.2812	-2.9516	IGS
M0SE	41.8931	12.4933	EUREF
VALE	39.481	-0.34	EUREF
VFCH	47.294	1.72	EUREF
VIGO	42.1840	-8.8131	EUREF

Table A.2: GNSS VEN1 fiducial stations coordinates and database for data processing.

Station name	**Latitude (°)**	**Longitude (°)**	**Database**
BRMF	45.7261	4.9384	RGP
VEN1	45.4306	12.3541	EUREF
GENO	44.4194	8.9211	EUREF
GRAZ	47.0671	15.4935	IGS
GSR1	46.0481	14.5437	EUREF
MATE	40.6491	16.7045	IGS
MEDI	44.5200	11.6468	EUREF
TRIE	45.7098	13.7635	EUREF
WTZR	49.1442	12.8789	IGS
ZADA	44.1132	15.2276	EUREF
ZIMM	46.8770	7.4653	IGS

Table A.3: GNSS Adriatic estimated stations coordinates and database for data processing.

Station name	**Latitude (°)**	**Longitude (°)**	**Database**
ANCG	43.6027	13.5019	ITALPOS
GARI	44.6769	12.2494	EUREF
MEDI	44.5200	11.6468	EUREF
PORE	45.226	13.595	EUREF
TRIE	45.7098	13.7635	FREDNET
VEN1	45.4306	12.3541	EUREF
ZADA	44.1132	15.2276	EUREF

Table A.4: Tide gauge stations locations and coordinates.

Place	**Latitude (°)**	**Longitude (°)**	**Time coverage (yr)**
Trieste	45.649	13.757	2010 - 2024
Monfalcone	45.778	13.550	2007 - 2022
Venezia	45.430	12.336	2010 - 2024
Ravenna	44.491	12.283	2010 - 2024
Ancona	43.609	13.481	2010 - 2024
Rovinj	45.083	13.628	1955 - 2005
Zadar	44.123	15.235	1991 - 2005
Split	43.506	16.441	1956 - 2005

Appendix B

Tidal analysis

Table B.1: Tidal constituents (wave groups) used in the UTide harmonic analysis. Frequencies are astronomical and given in cycles per hour (cph), periods are given in hours. Tidal constituents are automatically selected using the Foreman (M. Foreman, 1977) decision-tree criterion, which applies the Rayleigh resolution criterion within the UTide framework.

Constituent	**Frequency (cph)**	**Period (h)**
Long-period wave group		
SA	0.0001141	8765.8
SSA	0.0002282	4382.9
MM	0.0015122	661.3
MSF	0.0028219	354.4
MF	0.0030501	327.9

Constituent	**Frequency (cph)**	**Period (h)**
Diurnal wave group		
K1	0.0417807	23.93
O1	0.0387307	25.82
P1	0.0415526	24.07
Q1	0.0372185	26.86
J1	0.0432929	23.10
OO1	0.0448308	22.31
S1	0.0416667	24.00
NO1	0.0402686	24.84
PHI1	0.0420089	23.80
THE1	0.0430905	23.20
CHI1	0.0404710	24.71
PSI1	0.0418948	23.87
PI1	0.0414385	24.13
UPS1	0.0463430	21.57
RHO1	0.0357064	28.00
SIG1	0.0374209	26.72
SO1	0.0446027	22.42
TAU1	0.0446027	22.42
ALP1	0.0343966	29.07
BET1	0.0400404	24.97
H1	0.0803973	12.44

Constituent	**Frequency (cph)**	**Period (h)**
Semidiurnal wave group		
M2	0.0805114	12.42
S2	0.0833333	12.00
N2	0.0789992	12.66
K2	0.0835615	11.96
L2	0.0820236	12.19
T2	0.0832193	12.01
NU2	0.0792016	12.63
2N2	0.0774871	12.91
MU2	0.0359087	27.85
EPS2	0.0834474	11.98
GAM2	0.0803090	12.45
LDA2	0.0818212	12.22
ETA2	0.0850736	11.76
OQ2	0.0759749	13.16
R2	0.0761773	13.12
H2	0.0807396	12.39
MKS2	0.0818212	12.22
MSN2	0.0389588	25.66

Constituent	Frequency (cph)	Period (h)
Shallow-water (overtides and compound) wave group		
MSM	0.0013098	763.6
M3	0.1207671	8.28
SK3	0.1251141	7.99
MO3	0.0848455	11.78
SO3	0.2474062	4.04
MK3	0.1595106	6.27
S4	0.1666667	6.00
M4	0.2400221	4.17
SK4	0.1610228	6.21
MK4	0.2028035	4.93
SN4	0.2084474	4.80
MN4	0.1623326	6.16
MS4	0.1638447	6.10
M6	0.2415342	4.14
M8	0.3220456	3.11
2SM6	0.2471781	4.04
2MS6	0.2443561	4.09
MSK6	0.2445843	4.09
2MK6	0.2445843	4.09
2MN6	0.1668948	5.99
2MK5	0.1222921	8.18
2SK5	0.2833149	3.53
3MK7	0.2400221	4.17